UNIVERSITÀ
DEGLI STUDI
DI PADOVA

UNIVERSITY OF PADOVA

Center of studies and activities for space "Giuseppe Colombo" - CISAS

Ph.D. COURSE IN: Space Sciences, Technologies and Measurements
CURRICULUM: Sciences and Technologies for Aeronautics and Satellite Applications

SERIES XXXII

MORPHOLOGICAL AND COMPOSITIONAL ANALYSIS OF BOULDER DISTRIBUTIONS ON COMET 67P/CHURYUMOV-GERASIMENKO

Ph.D. Course Coordinator: Prof. Giampiero Naletto
Supervisor: Prof. Giampiero Naletto
Co-Supervisor: Dr. Gabriele Cremonese

Ph.D. Student: PAMELA CAMBIANICA

UNIVERSITÀ DEGLI STUDI DI PADOVA

Centro di ateneo di studi ed attività spaziali “Giuseppe Colombo” - CISAS

CORSO DI DOTTORATO DI RICERCA IN: Scienze Tecnologie e Misure Spaziali
CURRICOLO: Scienze e Tecnologie per Applicazioni Satellitari e Aeronautiche

CICLO XXXII

ANALISI MORFOLOGICA E COMPOSIZIONALE DI FAMIGLIE DI MASSI APPARTENENTI ALLA COMETA 67P/CHURYUMOV-GERASIMENKO

Coordinatore Corso di Dottorato: Ch.mo Prof. Giampiero Naletto
Supervisore: Ch.mo Prof. Giampiero Naletto
Co-supervisore: Dr. Gabriele Cremonese

Dottoranda: PAMELA CAMBIANICA

Dedico questa tesi alla mia famiglia e a Edoardo, senza i quali non avrei potuto raggiungere questo traguardo e nemmeno concludere questo importante percorso.

Abstract

The European Space Agency's Rosetta mission consisted of the orbiter spacecraft Rosetta and the lander Philae. Launched in 2004, the space probe reached the comet 67P/Churyumov-Gerasimenko after a journey lasted more than ten years. The objectives of the mission were to map the comet, to study its composition, to investigate the chemical and thermal properties, and to monitor the activity during its journey in the inner Solar System. Rosetta was the first mission to rendezvous with a comet, and to deploy a lander on a comet's surface. From a wider prospective, the Rosetta mission allowed to investigate the origin of comets, and to define the implication for the origin of the Solar System. We used OSIRIS Narrow Angle Camera with a spatial scale smaller than 2 m/pixel to analyze the surface of comet 67P. The surface reveals a variety of terrains and geological features, suggesting to be a very active and complex environment. In the first part of the thesis, a detailed quantitative analysis of isolated boulder fields is provided. We used different techniques to supply a method for analyzing the morphology of the boulders, which represent one of the ubiquitous and most important geological features on the comet. In the second part, a method to measure the seasonal evolution of Hapi's deposit is described, providing an upper limit for Hapi's water ice fraction. Measuring the evolution of the heights of some boulders, we fixed the pristine 67P ice content, and we compared the results with the InterStellar Medium and CI-Chondrites. Finally, we investigated the macroscopic thermomechanical behavior of a 40 meter boulder located on the Imhotep region by modeling its response to diurnal thermal forcing. Preliminary results reveal that stresses occur in the boulder's exteriors due to the sudden variation in temperature during sunset and sunrise. We explored whether the simulated stress is enough to propagate preexisting cracks, discussing the implications for rock breakdown.

Acknowledgements

OSIRIS was built by a consortium of the Max-Planck Institut für Sonnensystemforschüng, in Göttingen, Germany, CISAS University of Padova, Italy, the Laboratoire de Astrophysique de Marseille, France, the Instituto de Astrofísica de Andalucía, CSIC, Granada, Spain, the Research and Scientific Support Department of the European Space Agency, Noordwijk, The Netherlands, the Instituto Nacional de Tecnica Aeroespacial, Madrid, Spain, the Universidad Politechnica de Madrid, Spain, the Department of Physics and Astronomy of Uppsala University, Sweden, and the Institut für Datentechnik und Kommunikationsnetze der Technischen Universitat Braunschweig, Germany. The support of the national funding agencies of Germany (DLR), France (CNES), Italy (ASI), Spain (MEC), Sweden (SNSB), and the ESA Technical Directorate is gratefully acknowledged. We thank the ESA teams at ESAC, ESOC and ESTEC for their work in support of the Rosetta mission. We made use of Arcgis 10.3.1 software together with the Matlab, Java, and ImageJ software to perform our analysis.

Contents

List of Figures

List of Tables

Chapter 1

Introduction

Comets are considered primordial objects which can reveal information about the formation and evolution of the Solar System (Glassmeier et al., 2007). These minor bodies are thought to be remnants of planetesimals in the solar nebula, and their history may provide indications to physical and chemical conditions within the nebula in which our Solar System formed. Comets are irregularly shaped objects, composed of dust and ice, orbiting around the Sun on strongly elliptical paths. As a comet nucleus approaches the Sun, the heat warms the surface, causing the icy components to sublimate. This results in the ejection of gases and dust particles from the comet. These particles and gas molecules surround the nucleus, diffuse the Sunlight, and form the so called *coma*. The Sun's radiation pressure pushes away the escaping dust particles, forming a tail of dust. Meanwhile, the ultraviolet radiation of the Sun ionizes the gas molecules, forming the narrower plasma tail following the solar wind. There are two reservoirs containing comet nuclei. The largest reservoir surrounds the Solar System as far as 100.000 astronomical units (au) (Morbidelli, 2005). It is called Oort cloud and may contain more than trillion icy bodies. Beyond the orbit of Neptune, the Trans-Neptunian objects (TNO's) form a diffuse disc of scattered small bodies (Whipple, 1987). This region can be considered as a second and smaller reservoir of comets. This disk contains also planet-like bodies located in the Kuiper-Edgeworth Belt. It extends from about 30 to 55 au. Comets from the Kuiper Belt, known as short period comet, take less than 200 years to orbit the Sun (Stern and Colwell, 1997). Since comets are time capsules that hold clues about the formation and evolution of the Solar System, a cometary mission becomes fundamental to investigate these topics. The first probe to visit a comet was the *NASA ICE* probe. Launched on 12 August, 1978, ICE achieved the first ever comet encounter. It was sent to study comet Giacomini-Zinner. The mission proved the "dirty-snowball" theory, that comets are composed of mixed rock and ice (Whipple, 1950). The mission ended in 1981. The next probes to visit a comet were the Japanese's *Sakigake and Suisei* probes. Launched on 7 January, 1985, and 18 August, 1985, respectively, these twin spacecraft explored comet Halley on its journey into the inner Solar System. The first European Space Agency (ESA)'s deep space mission was *Giotto*. The probe was launched in 1985, and was able to study two comets: comet Halley in 1996 and comet Grigg-Skjellerup in 1992. Thanks to this mission, the closest pictures ever taken of a comet were obtained, being its closest approach to Halley comet only 650 km. Developed in collaboration with ESA and NASA, the *Ulysses* probe was designed for Solar studies. During its period of activity, it passed close to comet Hyakutake in 1996, allowing to study its tail. *Stardust* was the first NASA mission traveling into the coma of a comet. Launched on 7 February, 1999, this probe analyzed the cloud of ice and dust that surround the nucleus of comet Wild 2, coming to within 240 kilometers of the nucleus itself on 2 January, 2004. There, it gathered comet dust particles and delivered them back to Earth in 2006. NASA's *Deep Impact* mission was launched on 12 January, 2005, and consisted of two probes. The main spacecraft performed a flyby of comet Tempel 1. The purpose of the second probe was to send a projectile to the comet creating an impact crater. The impact excavated debris from the comet, allowing the main spacecraft to analyse the composition of the surface and the interior materials.

The European Space Agency's *Rosetta* mission was the first designed to orbit and land on a comet. Launched in March, 2004, the Rosetta spacecraft arrived at its primary target, the Jupiter-family comet 67P/Churyumov-Gerasimenko (hereafter 67P), on 6 August, 2014. The probe was first guided into an orbit about its target to perform first analysis and find a suitable landing site. The Philae lander was released from the orbiter on 12 November, 2014. Rosetta's payload included a suite of instruments that investigated the coma, the chemical interaction with radiation and the solar wind, the activity of the comet, the nucleus and its surface morphology. Its main objectives were to characterize the cometary nucleus and its surface topography, and obtain data on its chemical and mineralogical composition. Other experiments were focused on studying 67P's physical properties, such as thermal behavior or magnetic parameters, and on monitoring the activity during its approach to the Sun. The comet nucleus appeared rather dark and characterized by a peculiar surface structure. The 67P nucleus surface reveals a huge variety of terrains and geological features (Thomas et al., 2015b). In particular, the comet shows different types of landforms: smooth regolith plains, vertical cliffs, and talus aprons. The observations of nucleus's surface revealed layers that corresponded to terraces (planar patches of terrains arranged in staircase patterns of overimposed tabular elements) and/or linear traces on vertical cliffs and on the wall of pits (Massironi et al., 2015; Thomas et al., 2015b; Vincent et al., 2015a). These surfaces, their distribution, and the magnitude of insolation (Vincent et al., 2017) seem to define the morphologies that are present on the cometary surfaces. The presence of large blocks is one of the ubiquitous and most important geological features of 67P: these boulders can be found both isolated and in clusters and their size distribution depends both on the formation and evolution they have undergone (Pajola et al., 2015). The presence of boulders on comet 67P offers the opportunity to study the physical properties and the evolution of the comet itself. Being exposed on the surface of the comet, these objects undergo intense thermal fatigue, and reveal imprints of erosional and geological processes (Ehlmann et al., 2008). It is therefore important to understand how these objects may have originated and what this means in the framework of cometary evolution.

Objectives and Strategy

This thesis aims at contributing to the research dealing with cometary boulder formation and erosion by providing some answers to the previously described scenario. In particular, we investigated the fragmentation processes responsible for the presence of boulders on the surface of comet 67P. This research is divided into three main parts: in the first part, we quantitatively describe populations of boulders located in three different regions of comet 67P, namely *Imhotep, Hapi and Hatmehit* (Thomas et al., 2015b; El-Maarry et al., 2015), using OSIRIS NAC images. In particular, we propose techniques to analyze populations of boulders that can complement previous studies, analyzing the size-frequency distribution and the cumulative fractional area, linking these data with the fractal theory. Boulder counting can be used to understand and characterize surface properties (Birch et al., 2017) and the processes that result in fragmentation. Characterizing the population of boulders and the cumulative size-frequency distribution may lead to a better comprehension of the geologic history of the cometary surface (Garvin et al., 1981). In this context, a fractal fragmentation model can be used to quantify and predict the size-frequency distribution of fragments produced by a given energy input. The power-law exponent determined by the size-frequency analysis can be interpreted as a fractal dimension. This number describes the filling capabilities of the fragments generator. We also outlined the morphology of boulders, providing a shape parameter set independent of different observing geometries. The shape of boulders may provide indications on geological processes that leave morphological marks on rocks'

surfaces at different spatial scales (Viles, 2001). This is particularly true if signatures in boulder shape and surface texture can be identified and interpreted (Ehlmann et al., 2008).
In the second part of this thesis, we focus our analysis on a specific region of comet 67P. This region, named *Hapi*, is located in the northern hemisphere of 67P, in the neck that joins the big and the small lobe. Due to its location and lobe shadowing, Hapi experiences day-night cycles twice every comet rotation (Pajola et al., 2019) during the northern summer, when the comet is at heliocentric distances >1.6 au pre-perihelion and >2.6 au post-perihelion (Keller et al., 2015). It has been classified as a deposit of debris (Thomas et al., 2015a), similarly to Agilkia and Sais regions (Pajola et al., 2017), and is characterized by a distribution of boulders/outcrops of tens of meters in size scattered in the debris plain (Cambianica et al., 2019), and dune fields, which suggest a deposit thickness of several meters (El-Maarry et al., 2015). Analyzing this region, we noticed changes in terms of dust content. The opportunity to record the time evolution of dust in the Hapi region is linked to the likely source of the deposit surrounding the boulders, namely the erosion of the southern hemisphere, the subsequent transport of material, and then its fallout on the nucleus (Fulle et al., 2018b; Keller et al., 2015). We developped a Matlab tool that allows to measure the time evolution of the height of boulders, defined as the difference between the top of the boulders and the surrounding pebble deposit surfaces. No variation in morphology or position of boulders was recorded during the mission (Cambianica et al., 2019). Thus, any height variation is not due to boulder intrinsic changes, but to erosion/accretion of the surrounding deposit. The adopted technique is based on the measurement of the shadow length projected by the boulder itself. From the measurement of the evolution of the heights of some boulders, on the basis of a suitable comet nucleus surface evolutionary model (Fulle et al., 2018a) we have been able to infer the pristine 67P ice content.
In the last part of the presented research, we focus on rock weathering due to solar induced thermal stresses via the process of thermal fatigue. Thermal stress weathering is defined as rock breakdown due to the expansion and/or contraction of the material induced by heating and/or cooling (Lamp et al., 2017). To evaluate quantitatively the potential for thermal fatigue on the surface of 67P, we used a combination of finite element modeling and subcritical crack growth theory. Modeling temperatures and stresses in boulders, we derived the maximum tensile stress for different combination of materials and numbers of thermal cycles, to determine whether the modeled maximum tensile thermal stress is sufficient to propagate cracks inside the boulder. We modeled a specific boulder of 67P, located in the Imhotep region which shows all the effects typically associated to thermal stress, as the production

of split rocks, fragments (Dorn, 2003), and cracks on the surface (Bourke et al., 2007b).

Outline of the Following Chapters

In the following chapters, we describe in depth the results. The thesis is divided into 5 chapters:

- **Chapter one**: this introduction.
- **Chapter two**: an overview of the Rosetta mission is provided. We describe the birth and the timeline of the mission, the experiments onboard both the orbiter and the lander, focusing on a specific instrument, the Optical, Spectroscopic, and Infrared Remote Imaging System (OSIRIS). Also, we describe the world of comets, introducing and describing comet 67P/Churyumov-Gerasimenko before and after the mission. At the end of this chapter, the contribution Rosetta has made to the cometary science will be evident.
- **Chapter three**: in this chapter the concept of soil fragmentation is introduced. We investigate fragmentation models in the past century, and we explore the link between this process and the fractal theory. In this context, we present a quantitative analysis of isolated boulder fields on comet 67P, to investigate the origin of this features.
- **Chapter four**: in this chapter we present observations by the Rosetta mission to comet 67P fixing its pristine ice content. The seasonal evolution of Hapi's deposit erosion/accretion provides an upper limit for Hapi's water ice fraction. We describe the adopted method based on the measurement of the shadow length of boulders located in the comet's northern neck, to monitor the time evolution of their height.
- **Chapter five**: this chapter presents a thermomechanical model realized to investigate the response of boulders to diurnal thermal forcing. The geometry and mesh, the material selection, the boundary conditions and physics are described. We finally link the preliminary results with the implications for rock breakdown.
- **Chapter six**: conclusions.

Each chapter can be read independently of the others, but a linear reading will naturally facilitate their understanding.

Chapter 2

The Rosetta Mission. Discovering Comet 67P/Churyumov-Gerasimenko

Rosetta has been the first space mission to realize a rendezvous with a comet and to land on its nucleus. The mission takes its name from the Egyptian town of Rosetta, in which a stone inscribed with three scripts (hieroglyphic, demotic, and Greek) in two different languages (Egyptian and Greek) was found. This document was fundamental to decipher the hieroglyphs, and contained all of the good things that the pharaon has done for the priests and the people of Egypt. As the stone has allowed to decipher important secrets of ancient Egypt, the goal of the Rosetta mission was to reveal secrets of one of the most primordial objects of our Solar System, comet 67P/Churyumov-Gerasimenko. Launched on 2 March, 2004, on a 10-year journey towards comet 67P, Rosetta investigated its target for more than two years. The mission was concluded on 30 September, 2016, with a controlled impact onto the surface. The scientific objectives of the mission were to observe, image, and study the 67P's nucleus and coma with a spatial resolution never achieved before. Observing a comet from close range allows to investigate the surface and its features, its morphology, to observe the changes associated with the seasons as the comet approaches the Sun and leaves the inner Solar System. This mission also allowed to analyze the thermal properties of the nucleus, to investigate the composition of the coma, and to characterize its trend with developing activity. Along its way, the spacecraft passed by two main belt asteroids, 2867 Steins (in 2008) and 21 Lutetia (in 2010), before entering deep-space hibernation mode in July, 2011. This cruise phase was necessary because its trajectory took it beyond Jupiter's orbit, where the solar arrays would have been unable to produce sufficient energy. On 6 August, 2014, Rosetta arrived at its target, and on 12 November the Philae lander was released on the surface. During the following phases of the mission, Rosetta accompanied the comet through perihelion (13 August, 2015) until the end of the mission.

In this chapter a brief introduction about comets and the main characteristics of the Rosetta mission are reported. A description of the instruments onboard the orbiter and the lander is included, focusing on a specific instrument, the Optical and Spectroscopic Infrared Remote Imaging System (OSIRIS). In the second part of this chapter, a global description of comet 67P, before and after the Rosetta mission, is presented.

2.1 The World of Comets Before the Rosetta Mission

Comets are conglomerates of dust and ice, circling the Sun on strongly elliptical orbits. They are the remnants of the birth of our Solar System, and it is therefore essential to study them for understanding its formation. These objects are the best candidates for the delivery of water on Earth, and contain organic molecules considered to be the building blocks of life on our planet (van Boekel et al., 2004). Since they remain at large distance from the Sun, they are solar system objects unmodified by erosional processes due to the Sun's radiation and gravity effects. As a comet approaches the Sun, the ice components begin to sublimate, and the dust is released to the outer space. The core structure of a comet is known as the *nucleus*. It is composed of rock, dust, water ice, and frozen gases, such as ammonia, carbon dioxide, carbon monoxide, and methane (Greenberg and Li, 1999). The origin of comets is still debated, but several models suggest that the formation of comet nuclei can be explained by the accretion of primordial cometesimals (Jutzi et al., 2010). For this reason, comets are considered the building blocks from which the planets formed. It is difficult to directly observe a nucleus and describe it, but its surface appears generally rocky or covered in dust, suggesting that ices are hidden beneath the surface. Cometary surfaces appear also very dark, as demonstrated by their low albedo, proposing the presence of organic compounds (Buratti et al., 2016). The dust and gas released from the nucleus form an envelope around it, called the *coma*. At the distance the solar wind becomes strong enough to sweep the gas and dust away from the coma, tails form. The streams of dust and gas form their own distinct tails, pointing in slightly different directions. A *type I*, or *gas tail*, is produced by

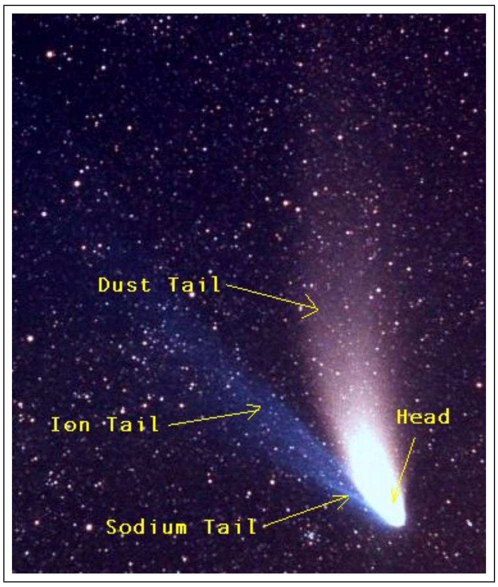

Credits: E. Kolmhofer, H. Raab; Johannes-Kepler-Observatory, Linz, Austria

Figure 2.1: Picture of Hale-Bopp comet showing the dust, ion gas, and sodium tails.

ionized gas carried away from the nucleus by the solar wind. This tail points directly away from the Sun, because the gas is strongly affected by the solar wind and radiation. The spectrum of a gas tail is an emission spectrum, revealing atoms and ions such as water (H_2O), carbon dioxide (CO_2), carbon monoxide (CO), hydrogen (H), hydroxide (OH), oxygen (O), sulfur (S), and carbon (C) (Seeds, 1997). These elements are released by the vaporizing ices, and after the breakdown of these molecules, some gases, such as hydrogen cyanide (HCN), can be formed by chemical reactions. A *type II*, or *dust tail*, is produced by dust pushed outward by the pressure of Sunlight. The gas is affected by the magnetic field of the solar wind, so dust tail appears more uniform than gas tail. The direction and shape of the gas tail is controlled by the magnetic field embedded in the solar wind. On the contrary, the dust tail appears often curved because the dust particles follow their individual orbits once they leave the nucleus (see Fig. 2.1). In 1997, during an observational campaign on the Canary Island, a third tail composed of neutral sodium was discovered (Cremonese et al., 1997). Studying Hale-Bopp, the authors suggested that the narrow sodium tail they found, was generated by the release of sodium atoms by the dust particles (Cremonese and Fulle, 1997).

Comets are classified according to the length of their orbital period. Most comets have long, elliptical orbits with periods greater than 200 years, and are known as *long-period comets.* Their orbits are very eccentric and randomly inclined, causing comets falling into the inner Solar System from all directions. In the 1950s, Jan Oort proposed that the long-period comets are objects originated in a region of the Solar System known as the *Oort cloud.* This region is a spherical cloud of icy bodies that extends from about 10.000 to 100.000 au from the Sun (Morbidelli, 2005). The gravitational influence of passing star or giant molecular cloud perturbs them from their resting place in the Oort cloud, causes them to fall into the inner Solar System in highly elliptical orbits. Originating from a spherical distribution, the high inclinations of the orbits arise since they can enter the inner Solar System from any angle. Some of these objects are the icy planetesimals that formed in the outer solar nebula. These bodies, however, could not have formed at their present location, because the solar nebula would not have been dense enough at that distance from the Sun. Furthermore, if these icy objects had formed in the solar nebula, they would be distributed in a disk and not in a sphere.

A recent evolutionary model places the birthplace of the long-period comets in a massive trans-Neptunian disk (Vokrouhlický et al., 2019). This disk was dispersed by migrating giant planets, such as Uranus and Neptune. As those planets were pushed outward by gravitational interactions with Jupiter and Saturn, they swept up many of these primordial objects, ejecting some of them in the outer part of the Solar System. Some of them vanished into space, but most comets had their orbits modified by the gravity and remain bound to the Solar System, becoming part of the Oort cloud. On the contrary, *short-period comets* have orbits with periods less than 200 years and follow orbits that lie within 30° of the ecliptic (Duncan et al., 1988). In 1951, Gerard P. Kuiper proposed that the origin of the Solar System should have left a huge number of icy planetesimals beyond the Jovian planets and in the plane of the Solar System. These objects are known as *Kuiper belt* comets (Kuiper and Hynek, 1951). The Kuiper belt extends from the orbit of Neptune to about 50 au from the Sun.

2.1.1 Comet 67P/Churyumov-Gerasimenko

67P/Churyumov-Gerasimenko is a Jupiter-family comet, originally from the Kuiper belt. These objects have orbital periods less than 20 years, and are named as such since their current orbits are primarily determined by the gravitational influence of Jupiter. 67P was discovered in 1969 by Klim Ivanovich Churyumov and Svetlana Ivanovna Gerasimenko of the Kiev University's Astronomical Observatory. Figure 2.2 shows the shape reconstruction done using the Hubble Space Telescope on March, 2003. The rotation

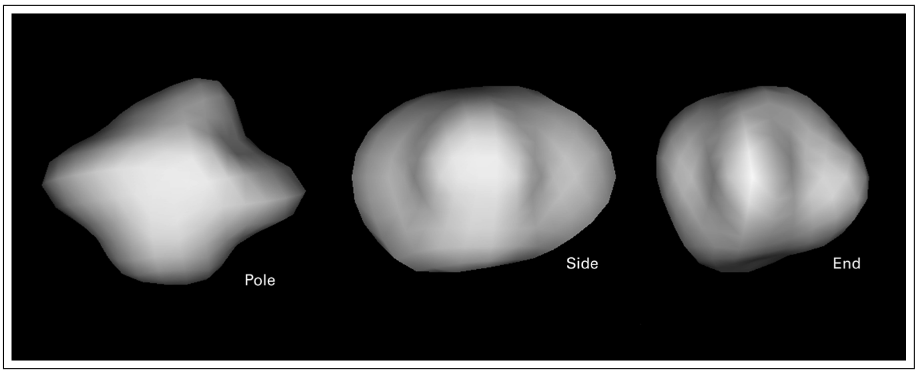

Credits: NASA, ESA, and Philippe Lamy (Laboratoire d'Astronomie Spatiale)

Figure 2.2: 3-D shape reconstruction of comet 67P Churyumov-Gerasimenko's nucleus. The Hubble Space Telescope revealed comet 67P/C-G to be an oval-shaped object of approximately 3 by 5 km in size.

period was estimated to be about 12 hours (Lamy et al., 2006). The original orbit of this comet has been modified by the gravitational influence of Jupiter. Until 1840, the perihelion was located at 4 au. A close flyby with Jupiter shifted the perihelion at 3 AU. Another close encounter with Jupiter moved further the point in the comet's orbit that is closest to the Sun at 1.25 AU.

2.2 The Rosetta Mission

The European Space Agency's Rosetta mission was the first designed to land on a comet. Selected in 1993, the space probe was launched in March, 2004, to comet 67P, and reached its target in August, 2014, after a ten-year journey. The original plan was for Rosetta to approach and study another comet, 46P/Wirtanen, with launch in January, 2003. However, due to problems with the launcher before the Rosetta launch, the latter was delayed and the launch window to reach Wirtanen closed and another target was selected: 67P/C-G.
Rosetta made use of gravitational pull maneuvers of Earth and Mars to reach its target with the right amount of acceleration, and during the cruise phase the spacecraft observed two asteroids, Steins in September, 2008, and Lutetia, in July, 2010. Rosetta entered the deep-space hibernation phase in July 2011. On 20 January, 2014, the spacecraft was roused from the hibernation mode. The journey through the inner Solar System covered 6.4 billion km in ten years. Rosetta reached its target on 6 August, 2014 (see Fig. 2.3

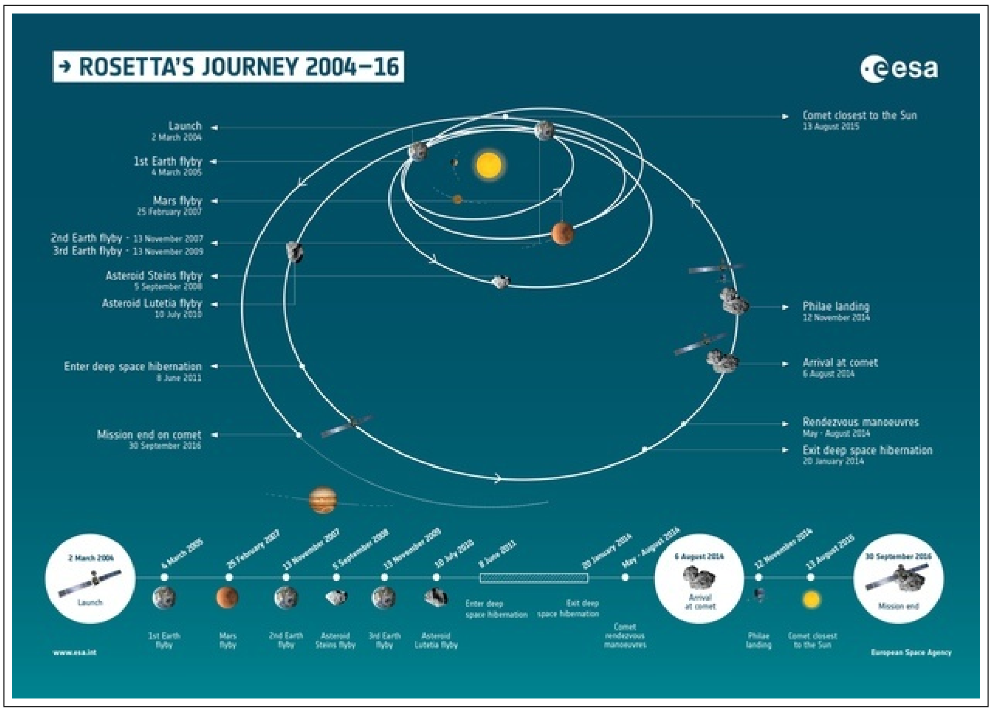

Credits: ESA

Figure 2.3: Trajectory details of Rosetta.

for trajectory details). On November 12, 2014, the spacecraft released the Philae lander, for the first touchdown on a comet nucleus. Unfortunately, its harpoons failed to fire properly and thrusters designed to anchor the probe to the surface did not activate. This resulted in the bouncing of the probe, which finally stopped in a location with very little sun illumination. Three days later, the lander entered safe mode and communicated sporadically with the spacecraft from 13 June to 9 July, 2015, but contact was then lost.

The main objectives of the mission were to describe the geological structure of the comet nucleus and the surface topography, analyze the chemical and mineralogical composition of the nucleus and the coma, investigate the physical and thermal properties of the nucleus, measure the magnetic parameters, and monitor the activity of the comet. For doing this, Rosetta carried a suite of eleven instruments on the comet orbiter and the lander Philae, which was equipped with other ten instruments. The instruments onboard the orbiter combined remote sensing techniques, with direct sensing systems such as dust and gas analysers.

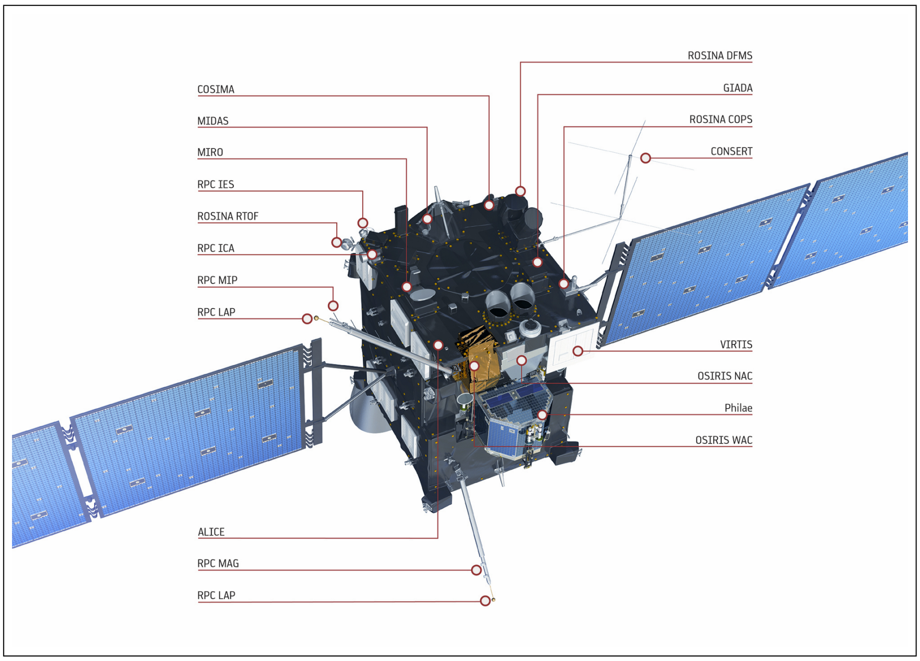

Credits: ESA

Figure 2.4: Instruments onboard the Rosetta orbiter.

2.2.1 Experiments on the Rosetta Orbiter

The Rosetta spacecraft design was a box-structure measuring 2.8 m × 2.1 m × 2.0 m on which all subsystems were mounted. The solar panels measured 14 m in length each, covering an area of 64 m^2 (see Fig. 2.4). A 28-watt parabolic antenna (2.2 meters in diameter) was mounted on the front side of the spacecraft, and two smaller antennas were mounted on the opposite side on the Philae lander to ensure communication between landing module and orbiter.

Remote sensing instrument

- **Alice**: ultraviolet-imaging spectrometer optimized for cometary far-ultraviolet spectroscopy. It was designed to obtain spatially-resolved spectra of 67P targets in the 700-2050 Å spectral band. The aim of this instrument was to detect gas molecules in the coma, noble gases, and ion in the tail (Stern et al., 2007);

- **CONSERT**: the Comet Nucleus Sounding Experiment by Radiowave Transmission was designed to generate a three-dimensional profile of

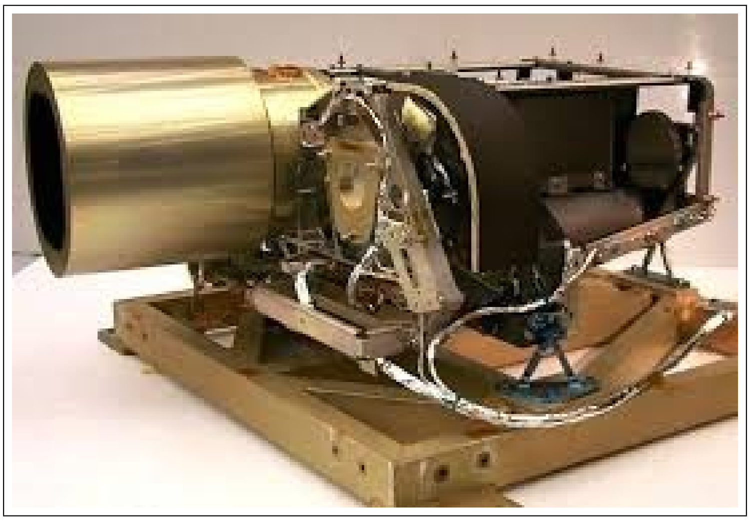

Credits: ESA/MPS

Figure 2.5: OSIRIS NAC, the scientific camera onboard Rosetta.

the comet's nucleus. The radar performed tomography of the nucleus by measuring electromagnetic wave propagation between the Philae lander and the Rosetta orbiter through the comet nucleus making use of the 2^{nd} CONSERT on the lander (Barbin et al., 1999);

- **MIRO**: the Microwave Instrument for the Rosetta Orbiter measured the surface temperature, the gas production rates, and relative abundances, the velocity, and excitation temperature of each detected gas molecules, along with their spatial and temporal variability (Gulkis et al., 2007);
- **OSIRIS**: the Optical, Spectroscopic, and Infrared Imaging System was designed to image the comet's nucleus and its environment. It consisted of two cameras operating from near-ultraviolet to near-infrared wavelengths. The Wide-Angle Camera (WAC) had a spatial scale of 10.1 m/pixel at 100 km from the surface, and its primary objective was to image the dust and the gas directly surrounding the nucleus. The Narrow-Angle Camera (NAC) (see Fig. 2.5)was designed to resolve the nucleus of 67P with a spatial scale of 1.86 m/pixel at the same distance (Keller et al., 2007). Specifications and technical data are reported in Table 2.1;
- **RSI**: the Radio Science Investigation instrument analyzed the shape, density distribution, and comet's gravity from the Doppler effect (Pätzold

Camera	Narrow-Angle	Wide-Angle
Field of view (degree)	2.20 × 2.22	11.35(y) × 12.11 (x)
Spectral filetrs	12	14
Spectral range (nm)	250-1000	240-720
Angular resolution (mrad/pixel)	0.0186 (average)	0.101 (average)
Detector size (pixel)	2048× 2048	2048× 2048

Table 2.1: Specifications of the OSIRIS instrument (Keller et al., 2007).

et al., 2007);

- **VIRTIS**: the Visible and Infrared Thermal Imaging Spectrometer performed spectral mapping and spectrometry of the comet, detecting the evolution of specific signatures such as the typical spectra band of minerals and molecules arising from surface components and from material dispersed in the coma. In addition, surface thermal distribution and evolution were performed (Coradini et al., 2007).

In-situ instrument

- **COSIMA**: the COmetary Secondary Ion Mass Analyser was based on the analytic measurement method of secondary ion mass spectrometry (SIMS). After the collection of cometary dust, it chemical characterized some components, including organics (Kissel et al., 2007);

- **GIADA**: the Grain Impact Analyzer and Dust Accumulator had the objective to measure the dust evolution and particles dynamic properties with position and time (Colangeli et al., 2007);

- **MIDAS**: the Micro-Imaging Dust Analysis System provided microtextural analysis and statistical parameters of pristine cometary particles in the nm-μm range (Riedler et al., 2007);

- **ROSINA**: the Rosetta Orbiter Spectrometer for Ion and Neutral Analysis consisted of two mass spectrometers for neutrals and primary ions with complementary capabilities and a pressure sensors. This instrument was designed to determine the mass of gases and characterize the composition and structure of the comet's atmosphere and ionosphere (Balsiger et al., 2007);

- **RPC**: the Rosetta Plasma Consortium instrument was designed to analyze the plasma environment of the comet, and investigate its interaction with the solar wind (Carr et al., 2007).

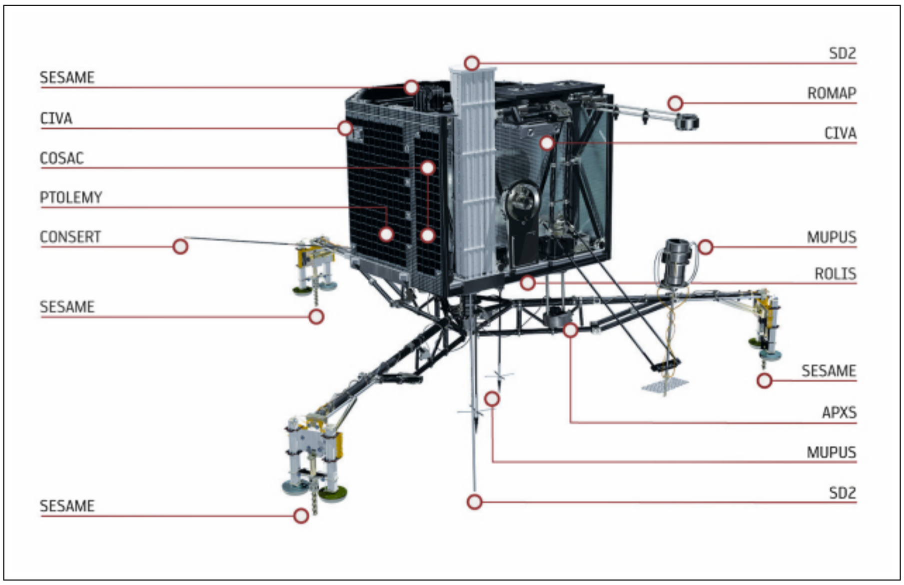

Credits: ESA

Figure 2.6: Instruments onboard the Philae lander.

2.2.2 Experiments on the Philae Lander

The structure of the Philae lander was composed of a carbon fiber baseplate, an instrument platform, and a polygonal sandwich construction. The lander was designed to work at temperatures between +50°C and -180°C. The instruments onboard the lander were (see Fig. 2.6):

- **ApixelS**: the Alpha Particle X-Ray Spectrometer was designed to analyze the detected alpha particles and X-rays, which could have provided information on the elemental composition of the comet's surface (Klingelhöfer et al., 2007);

- **CIVA**: the Comet Infrared and Visible Analyzer was composed of a group of seven cameras used to take pictures of the surface, in particular of the selected landing site, a visible-light microscope, and an infrared spectrometer (Bibring et al., 2007);

- **CONSERT**: the objective of the Comet Nucleus Sounding Experiment by Radiowave Transmission was to study the geometrical structure and electrical properties of the deep interior of the comet nucleus generating a three-dimensional profile of the comet (Barbin et al., 1999);

- **COSAC**: the Cometary Sampling and Composition instrument was designed to analyze the composition of the sub-surface (Goesmann et al., 2005);

- **MUPUS**: the Multi-Purpose Sensor for Surface and Sub-Surface Science had the objective to study the thermal properties of the comet. In particular, it was designed to measure the temperature and detect the thermal conductivity of the ground (Spohn et al., 2007);

- **PTOLEMY**: the aim of this spectrometer and gas chromatograph was to analyze the isotopic composition of the drilled sample (Todd et al., 2007);

- **ROLIS**: the Rosetta Lander Imaging System was designed to image the landing site and monitor the areas during descent (Mottola et al., 2007);

- **ROMAP**: the objective of the Rosetta Lander Magnetometer and Plasma Monitor was to quantify the magnetic field of the comet (Auster et al., 2007);

- **SD2**: the Sample, Drill and Distribution system was designed to drill the surface of the comet. The aim was to drill the surface up to 20 centimeters depth (Finzi et al., 2007);

- **SESAME**: the Surface Electrical, Seismic and Acoustic Monitoring Experiments contained sensors to characterize the electrical properties of the comet, and monitor dust-particle impacts (Seidensticker et al., 2007).

2.3 Comet 67P: a New Concept of Comet

Watching a comet during its approach to the Sun allows to learn and decipher secrets of an object that has preserved pristine material from the early Solar System. During the first six months of observing comet 67P, it became evident that this small body was anything but a simple dirty snow ball. The comet appeared rather dark, reflecting only 5% of the incident Sunlight. It rotated around a spin axis inclined by 52° with respect to the orbit plane (Keller et al., 2015). The inclination of the spin axis is responsible for the strong seasonal effects experienced by the comet. No intrinsic magnetic field was detected, suggesting that the magnetic field was not preserved during the formation of the comet (Auster et al., 2015). Rosetta confirmed that the

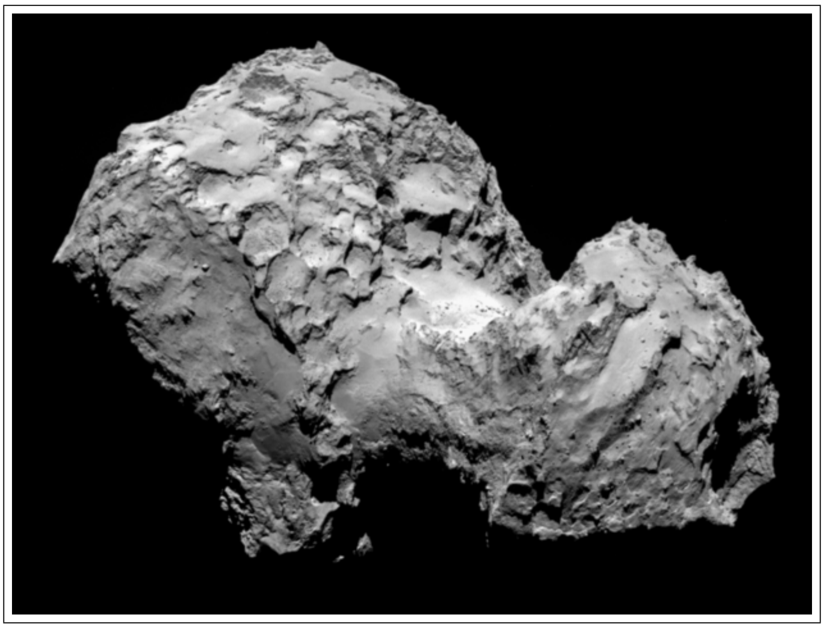

Credits: ESA/Rosetta/MPS for OSIRIS Team

Figure 2.7: One of the first images of comet 67P, taken on 6 August, 2014.

comet takes 12.4 hours to rotate around its axis (Mottola et al., 2014), and that its orbit is inclined 7° relative to the ecliptic. The perihelion is located at 1.25 au, the semi-major axis of its orbit measures 3.46 au (Keller et al., 2015), the eccentricity is 0.64° (Keller et al., 2015), and the mean anomaly is 303.71°. The structure of the comet appeared different from expectations. As shown in Fig. 2.7, comet 67P is defined as a bi-lobate object, composed of two lobes connected by a small structure, called the *neck*. How these two lobes have been generated is still debated. The theory of a merging after a low velocity collision seems to be the most likely explanation. The dimensions of the big lobe are 4.1 km × 3.3 km × 1.8 km. The small lobe measures 2.6 km × 2.3 km × 1.8 km. The volume of the comet is 21.4 km^3 (Sierks et al., 2015), and the mass was estimated to be about $(9.982 \pm 0.003)\times10^{12}$ kg (Pätzold et al., 2016). Based on the mass and volume, the density was fixed at 0.538 ± 0.006 g/cm^3 (Ptzold et al., 2018). The OSIRIS instrument was fundamental to image and investigate the surface of the nucleus. The Narrow and Wide Angle Cameras revealed a complex surface made of a huge variety of terrains and geological features (Thomas et al., 2015b). Smooth and hummocky terrains can be found, that are partially or entirely covered in dust. Furthermore, the comet shows different striking types of landforms: smooth flat regolith plains, vertical cliffs, and talus aprons. The observations of the nucleus surface also revealed layers that corresponded to terraces (planar patches of terrains arranged in staircase patterns of overimposed tabular elements) and/or linear traces on vertical cliffs and on the wall of pits (Massironi et al., 2015; Thomas et al., 2015b; Vincent et al., 2017). These surfaces, their distribution, and the magnitude of insolation (Vincent et al., 2017) seem to define the morphologies that are present on the cometary surfaces. The presence of layering can also exert an effect on the fragmentation processes at the scale of boulders, for instance by producing tabular-shaped boulders rather than spherical ones. Changes were observed on the comet's surface, particularly close to perihelion (El-Maarry et al., 2017). These variations were attributed to cometary weathering, erosion, and transient events driven by exposure to Sunlight. These surface changes included fractures growing in size, collapsing cliffs (Pajola et al., 2017), displaced boulders, and evolution of patterns of shapes in dusty terrains. In October, 2014, the activity of the comet was high enough for water (H_2O) and carbon dioxide (CO_2) to be detected in the coma by VIRTIS. The relative abundance of CO_2 with respect to water was about 4%, stating that comet 67P is rich in water and not in carbon dioxide (Migliorini et al., 2016). MIRO and ROSINA also detected CO_2 and H_2O, confirming VIRTIS results. The COSIMA instrument detected organic matter in the particles collected from the comet. Spectra show signatures of carbon compounds, such as the positive ions of carbon (C), methylidyne (CH), methylene $(CH)_2$, methanetriyl (CH_3), and ethylene (C_2H_3), as well as the negative ions of C and CH, plus a weak contribution signal from CH_2 (Bardyn et al., 2017). COSIMA did not detected organic molecules such as carboxylic acids, polycyclic aromatic hydrocarbons, and amino acids, although ROSINA detected volatile organics such as methyl formate ($HCOOCH_3$) and formamide (NH_2CHO) in the coma (Altwegg et al., 2017).

Thanks to the OSIRIS-Narrow Angle Camera (NAC), the nucleus surface has been divided in 26 regions (El-Maarry et al., 2016; Thomas et al., 2018). Regions on the small lobe are named after Egyptian goddesses (Anuket, Bastet, Hathor, Hatmehit, Maat, Maftet, Neith, Nut, Serqet, Wosret), while regions on the large lobe are named after gods (Anhur, Anubis, Aker, Apis, Ash, Aten, Atum, Babi, Bes, Geb, Imhotep, Khepry, Khonsu, Seth). The two regions on the neck of the comet are named after the Nile gods, Hapi and Sobek (see Fig. 2.8). Further details can be found in Table 2.2, 2.3, and 2.4.

Another focus of the OSIRIS instrument was to generate a high-resolution global map of the comet. This map was fundamental in choosing the landing site because the selection had to meet different scientific requirements and engineering safety criteria. The lander had to be deployed far from activity spots, and the presence of large boulders or fractures has to be taken into

Region	Description
Small Lobe	
Anhur	Scattered boulder fields Debris deposits Niches and alcoves
Anubis	Non-consolidated and smooth region Some scattered boulders and smooth deposits
Aker	Strongly consolidated, dark-toned unit Tectonic-like features Several small smooth areas are evident 200 m-long angular fractures
Apis	Strongly consolidated and smooth unit Irregular and polygonal lineations Polygonal crack patterns
Ash	Non-consolidate and dust-covered material Main debris-covered region of the body
Aten	Depression not covered by debris Possibly formed through a violent short-term event High concentration of talus deposits and rockfalls
Atum	Strongly consolidated and highly complex region Minimal bouldering, small depressions Irregular complex mounds
Babi	Transitional region exposing brittle mantling material
Bes	Terraced and fractured surface Internal layering Polygonally-fractured surface Boulders, pits, debris
Geb	Consolidated cliff regions Rarity of boulders and debris deposits Rectilinear and polygonal fractures
Imhotep	Non-consolidate, smooth material Extremly smooth, probably recently re-surfaced Conical structures and pits, large boulders
Khepry	Strongly consolidated, rough and bright region Numerous ponds of smooth deposits
Khonsu	Exposure of internal structure Lack of smooth material Pancake-like feature
Seth	Lacking a dust cover, bouldered region Presence of circular features that display polygonal cracks Strong evidence of collapse

Table 2.2: Description of the regions located on the small lobe of comet 67P (El-Maarry et al., 2016).

Region	Description
Big Lobe	
Anuket	Strongly consolidated and complex unit
Bastet	Strongly consolidated region with minimal bouldering Oriented lineaments
Hator	Strongly consolidated region 900 m-high cliff Heavly lineated in two dimensions and signs of detachment
Hatmehit	Depression filled with fine-grained
Ma'at	Non-consolidated and dust-covered region Smooth deposits and sharp outcrops
Maftet	Strongly consolidated and rough terrain, bouldered with scattered patches of debris Many small irregular depressions and pits
Neith	Strongly consolidated Main cliff of the big lobe Polygonal fractures
Nut	Bouldered small depression
Serqet	Strongly consolidated material region Smooth plain with few boulders
Wosret	Smooth region Parallel lineaments

Table 2.3: Description of the regions on the big lobe of comet 67P (El-Maarry et al., 2016).

Neck	
Hapi	Non-consolidated and smooth region The most active region and site of regular jet activity Smooth dusty-looking material Dispersed linear large boulders
Sobek	No smooth deposits High concentration of boulders Rough surface texture

Table 2.4: Description of the regions located on the neck of comet 67P (El-Maarry et al., 2016).

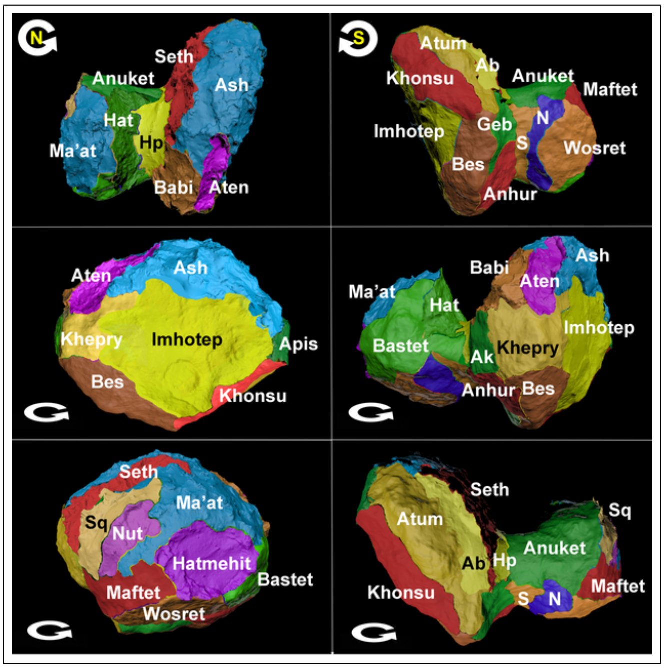

Credits: ESA/Rosetta/MPS for OSIRIS Team, (El-Maarry et al., 2016)

Figure 2.8: Twenty-six geological regions identified on comet 67P.

account. The Landing Site Selection Group (LSSG) selected five potential landing sites. On 14 October, 2014, it was decided to land in Agilkia (see Fig. 2.9) on 12 November, when the comet was at 3 au far from the Sun. This distance ensured that the Sunlight was sufficient for Philae's solar cells to generate enough power to operate. Philae touched down the surface of the comet at 16:34. Unfortunately, the cold gas jets responsible for the stability of the lander and the harpoons failed to fire, causing its bouncing after the first ground contact. It floated above the comet for about two hours. In this period the lander touched the comet twice before the final landing. It was stabilized in an unknown landing site at 18:31 (Biele et al., 2015).

The ROLIS camera imaged the descent of the lander. In all pictures, the regolith appears uniformly dark, boulders and pebbles measure from a few centimeters to five meters in diameter. The CIVA camera system imaged the final landing-site, showing a very dark environment due to the location of the site with respect to the Sun. The battery recharge was strongly compromised, and this situation changed the sequence of experiments. It was not possible to drill the surface and investigate the chemical composition of the terrains. However, the radio investigation revealed a homogeneous internal structure of the comet, and the magnetometer did not reveal an intrinsic

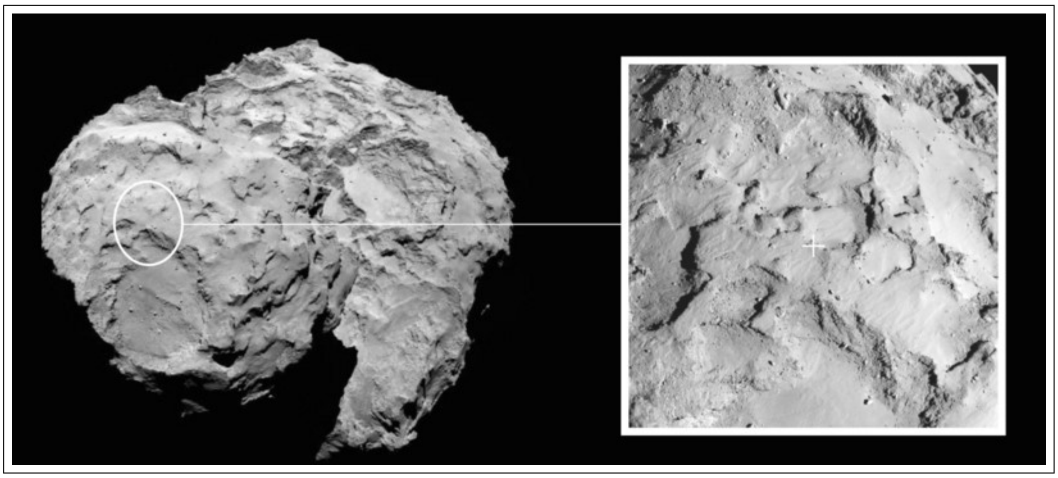

Credits: ESA/Rosetta/NavCam/MPS for OSIRIS Team

Figure 2.9: Agilkia landing site.

magnetic field surrounding the nucleus (Auster et al., 2015). The location of the lander remained unknown for a long period of time, until CONSERT and ROMAP circumscribed the final position, and less than a month before the end of the mission, the OSIRIS-Narrow Angle Camera revealed the Philae lander stuck into a dark crack. High-resolution images of the surface taken by the ROLIS camera revealed a surface with no dust. If the global surface appears covered in dust and regolith, some specific areas of the comet reveal a different scenario. The non-uniform regolith suggests that probably this material has been eroded by the activity of the comet, transported across the surface, and deposited elsewhere. It is also possible that the regolith might be ejected and subsequently fell back on the surface. Some mechanical properties of the material have been measured by the SESAME-CASSE sensor, such as the elasticity and porosity. SESAME measured also the maximum temperature across a cometary day (−165°C) (Möhlmann et al., 2018), and this value was complemented by the MUPUS thermal probe investigations. Having encountered a hard layer, the hummer penetrated only a few millimeters, revealing a material with a low thermal conducivity, and a temperature ranging from −165° at night up to −140° in the daytime (Kossacki et al., 2015).

Chapter 3

Fragmentation and Fractals. The Case of Isolated Boulder Fields on Comet 67P

Fragmentation is a complex phenomenon defined as the breakage of a continuous body into several pieces. This phenomenon is seen ubiquitously in nature and manifests itself in different contexts and at different scales. Its understanding is fundamental to predict the behavior of some materials under different stresses, and this leads to design innovative materials and improve industrial, medical, transport facilities, and many other applications. The physical mechanisms underlying the fragmentation have been studied across different fields such as material properties, geophysics, sub-atomical interactions (Anishetty et al., 1980), mineral formation, astrophysics, and planetary science. At the most fundamental level, the fragmentation may help to recount the history of our Solar System and its components, being limited only by the fundamental units of the matter itself. The wide range of applications led to a new branch of research that aimed to study this phenomenon during the previous century. The complexity and the violence of the fragmentation were recognized immediately, and for this reason scientists began by studying the output of fragmentation, namely the number of fragments and the distribution of the fragment sizes. The size distribution of the resulting material is fundamental to statistically describe the processes underlying the fragmentation, and to predict possible boulder fragmentations once the governing physical processes have been identified. In the context of planetary science, the study of fragmentation is complicated by the fact that often terrestrial models are extended to planetary environments usually rather different from terrestrial conditions, by relying on the universality of the related physical processes.

In the first part of this chapter, a survey of fragmentation processes and their relations with fractal theory are provided. The aim is to define a statistical and mathematical method applicable to planetary surfaces in general. The reason for this is that planetary exploration helps in solving the big enigma of the formation of our own planet Earth, the Solar System, and the galaxy to which it belongs. On one hand, a detailed description of the soil allows to better understand the global geological history of a planet or body; on the other, it complements engineering studies fundamental to the success of a planetary mission. In the second part of the chapter, the case of isolated boulder fields on comet 67P is presented. The Rosetta mission reveals a complex nucleus surface made of different terrains, partially or entirely covered by dust, exposing consolidated materials, fractures, and boulders, from the meter scale to the decimeter scale (Thomas et al., 2015b). This research focuses on boulders, and the aim is to characterize these features to better understand their origin and nature. For doing this, we will apply different techniques to define the size-frequency distribution of boulders, investigate their location, and connect these elements with the fractal theory. Finally, we will introduce a shape parameter set able to describe the morphology of the boulders, when high-resolution images are available.

3.1 Fragmentation Models in the Past Century

In the past century, fragmentation has been studied from different point of views. Empirical, analytical, and physics-based models have been developed to better understand the fragmentation process in different fields. In this section, an overview of the most important models is given.

3.1.1 Empirical Observational Models

Rosin-Rammler particle size distribution

The description of material consisting of various size fractions is a difficult target to describe. In 1933, Rosin and Rammler conducted experiments to determine empirical equations able to fit fragment size distributions resulting from fragmentation. The Rosin-Rammler equation is (Rosin, 1933)

$$y(x) = 1 - e^{-(x/x_0)^n} \tag{3.1}$$

where y is the cumulative fraction of material smaller than the size x, n is the shape parameter describing the material uniformity, and x_0 is the characteristic particle size. The latter indicates an intrinsic size of particle for a given system.

Schumann distribution

Schumann distribution (Schuhmann Jr, 1940) is defined as the limiting case of the Rosin-Rammler distribution. For small fragments, equation 3.1 can be simplified as follows:

$$y(x) = \left(\frac{x}{x_0}\right)^n \tag{3.2}$$

As shown in the next paragraphs, the direct proportionality between the cumulative fraction of material and the size raised to a constant value will be reused by Turcotte in the context of fractal theory.

Mott-Linfoot distribution

Mott-Linfoot distribution is used when the fragments can be easily counted and the mass can be measured. They carried out experiments on fragmentation of bomb shells, and fitted their results with (Mott, 2006b)

$$f(m) = 1 - e^{(m/m_0)^{1/2}} \tag{3.3}$$

where m is the fragment mass, and m_0 is the characteristic mass. This distribution is still used in the context of explosion of ductile materials. The logarithm of the cumulative number of fragments plotted against fragment masses defines the Mott plot.

3.1.2 Statistical and Geometrical Models

Lienau distribution

In 1936, Lienau proposed an exponential distribution. He described the one-dimensional fragmentation problem with a probability distribution function of random fracture. Considering a line that is about to collapse into several fragments, when the size of a fragment l is much smaller than the total length L, the distribution of breakpoints can be described by the Poisson distribution. In this case, the probability density distribution of fragments is

$$f(l) = (1/\lambda)e^{-l/\lambda} \tag{3.4}$$

where λ is the size scale parameter of the distribution. When the fragment size l is not much smaller than the total length, the random distribution of fracture points should be described by a random distribution, and the cumulative distribution is then:

$$f(e) = \frac{n-1}{L}\left(1 - \frac{l}{L}\right)^{n-2} \tag{3.5}$$

where $n = l/\lambda$ is the total number of fragments (Lienau, 1936).
In 1943, Mott and Linfoot extended the Lienau distribution to the multi-dimensional fragmentation. They focused their study on a two-dimension plate submitted to biaxial tension, concluding that the distribution of fragment sizes is strongly dependent on the geometric partitioning of the plate. This conclusion laid the foundation for shape analysis in fragmentation.

Voronoi-Dirichlet distribution

The Voronoi-Dirichlet diagram consists of a random distribution of points in a 2-d plate. The plane is splitted into regions, called *Voronoi cells*, by construction of perpendicular bisecting lines. In one dimension, the Voronoi-Dirichlet construction is considered as the dual of the Lienau distribution, since the single point in the middle of a cell can be represented also by the Lienau's breakpoint. In multi-dimensional context, partitioning an area or a volume, the fragment distribution is described by

$$f(m) = \frac{a}{m_0}\frac{n}{\Gamma(n)}\left(\frac{nm}{m_0}\right)^{n-1} e^{-nm/m_0} \tag{3.6}$$

where m is the fragment mass, and n is a constant equal to 2, 4, or 6 if a line, surface, or volume is considered (Grady, 2007).

3.1.3 Physics-Based Models

Dynamic analysis of fragmentation. Mott approach.

A perfect plastic material with yield strength Y can fail in both time and space. The failure is considered as an instantaneous event, which reduces the stress from Y to 0 at the breakpoint. This sudden failure results in stress waves, which propagate in the surrounding material. At the breaking point, the boundary between rigid and plastic regime is located in the position x:

$$x(t) = \sqrt{\frac{2Yt}{\rho\frac{\delta\varepsilon}{\delta t}}} \tag{3.7}$$

where ρ is the volumetric mass, and $\delta\varepsilon/\delta t$ is the strain rate.
Mott described also the occurrence of fracture in a stressed material. The probability that a fracture occurs in a length dl at strain ϵ is:

$$p(\epsilon) = \lambda(\epsilon) d\epsilon dl \tag{3.8}$$

Considering L as the length of the damaged object, which has not undergone fracture yet, the probability can be rewrite as follows:

$$\frac{dL}{L} = -\lambda(\epsilon) d\epsilon \tag{3.9}$$

Eq. 3.9 describes a complex geometrical situation of dynamic fragmentation, which involves the activation of breakpoints and subsequent stress release waves (Mott, 2006a).

Dynamic models

In his model, Mott assumed that the material is perfectly plastic and that the fractures is istantaneously generated in a breakpoint. These two assumption have been considered as physical limitations because this model does not take into account the failure duration and the dissipation of the energy. Grady (Grady, 2007) suggested that when stress decreases from a maximum value σ_{max} to 0, crack opens releasing the fracture energy

$$G_c = \frac{\sigma_{max}\delta_c}{2} \tag{3.10}$$

where δ_c is the maximum length of the crack. Studying the motion of the fragmentation, Grady derived also the spacing between two consecutive breakpoints as

$$s = \left(\frac{24G_c}{\rho \frac{\delta\epsilon}{\delta t}^2} \right)^{1/3} \tag{3.11}$$

Continuous fragmentation

Fragmentation is a complex phenomenon which occurs through different steps, usually described into three categories (Åström, 2006): uncorrelate breakup history, cascade fragmentation, and statistical rate equations. Description of fragmentation through its time evolution became fundamental to lay the groundwork of a new concept of fragmentation: the continuous fragmentation. The three categories are described as follows:

- *Uncorrelated breakup history*: in the uncorrelated breakup history, if a fragment breaks $i-$times, where i has a Gaussian probability distribution, the density function of the fragment size distribution can be described as follows (Delannay et al., 1996):

  $$f(s) \propto exp^{-\left(\frac{ln(s)-\mu}{\sigma^2}\right)} \tag{3.12}$$

  where μ and σ are constant;

- *Cascade fragmentation*: cascade fragmentation has been studied by different authors (Turcotte, 1986; Bourne et al., 1997; Krapivsky and Majumdar, 2000; Kadono and Arakawa, 2002). Each of them defined this process starting from a fragment of unit area, broken into n pieces of area $1/n$. For a fragment that is not broken, the process is over. Otherwise, each fragment is further split, and the probability density function is described by:

  $$f(s) \propto s^{-\frac{Dln(p)}{ln(n)}-(D+1)} \tag{3.13}$$

  where D is the space dimension, and p is the probability of a fragment to be splitted;

- *Rate equations of fragmentation*: for any application where the sizes of the particles are measured experimentally whereas the fragmentation rates are unknown, a kernel $k(s,x)$ defines the probability to form a fragment of size s from a parent of size x. A general form of the rate equation is:

  $$\frac{\delta f(s,t)}{\delta t} = -a(s,t)f(s,t) + \int_s^\infty f(x,t)a(x,t)k(x,t)dx \tag{3.14}$$

  where $a(x,t)dt$ is the breakup rate for a fragment of size s in a time interval t, and f is the probability density function of the fragment sizes. The first term of Eq. 3.14 is the *loss term*, and determines the breakup of a fragment. The second term is the *gain term*, and defines the formation of fragments.

3.1.4 Material Defects in Fragmentation

Following Mott's approach, the activation of a defect within the materials generates stress waves, which propagate from the activation point to the surrounding area. As a result, scientists began to examine the conditions under which cracks interact.

Fragmentation model with no crack interactions

In the context of no crack interactions, defects placed randomly within the materials do not influence each other. In 1969, Lindborg approached this problem neglecting stress concentration form preexisting cracks and determined the fraction of cracked grains in a sample as follows:

$$p = 0.2 \left(\frac{2n}{N} \right)^{1/n} \tag{3.15}$$

where n is the number of cracks aggregates, and N is the number of grains within the sample. He found that in any case, at least 20% of the grains are cracked before complete fracture (Lindborg, 1969).

Fragmentation model with crack interactions

In 2000, Aström stated that if cracks are close enough, their interaction cannot be neglected, arguing that in the small range, crack merging process prevails and induce scale-invariant size distribution (Åström, 2006). He described the distribution of fragment mass as:

$$F(m) = am^{\alpha} e^{-m/M_0} \tag{3.16}$$

where a and α are constant values depending on loading conditions, m is the mass, and M_0 is a system-dependent length.

3.2 Soil Fragmentation and Fractal Theory

Fragmentation is defined as the action or process of breaking a body into smaller parts. Focusing on soil fragmentation, this process can be classified as instantaneous or continuous. In the first case, the fragmentation is caused by a single and violent event (Hernandez et al., 2012), such as the blasting of a rock or an impact. In the latter case, the fragmentation is due to events occurring progressively in time. Each of them contributes to the formation of a Particle Size Distribution (PSD), and the proper understanding of the physics behind the fragmentation leads to different interpretations of the fragments' distribution. Schmidt (Schmidt et al., 1999) defined the PSD as a fundamental statistical property of a soil since it allows to directly investigate the soil's origin and the processes that have altered it through time. In general, the PSD of a granular material is described as a series of functions that define the amount of particles present in a soil according to their size. Each different soil textural elements are defined into main classes (e.g. sand, silt and clay) and each one of these is described by a statistical cumulative distribution. The differences between the various classes can be detected plotting the data bi−logarithmically. Each class depicts its linear, power-law behavior, suggesting that different processes have influenced the formation and evolution of the soil over time. The power of the PSD is also due to the fact that it may be described by the fractal theory (Turcotte, 1986). The exponents derived from the power-law can be explicitly considered as the fragmentation fractal dimension of the distribution.

3.2.1 Fractal Geometry

Fractal geometry is a branch of mathematics (Mandelbrot, 1983) that describes most physical systems of nature characterized by a non-regular geometric shapes of the standard Euclidean geometry. In fact, unlike Euclidean dimension D_E, the fractional dimension falls in between the integers of topological dimension D_T. This property is defined as *non-integer dimension*. Classical geometry defines objects by means of integer dimensions: points are zero dimensional objects, lines are one dimensional objects, plane figures are two dimensional objects, and solids are three dimensional objects. Fractal geometry describes many natural phenomena using a dimension between the previous. In this scenario, a fractal curve will have a dimension between one and two, depending on how much space occupies as it curves. The *self-similarity* is another important property of fractals. This mathematical features states that parts of the whole pattern are redundantly reproduced at increasingly reduced scales. In other words, the self-similarity is the variation of pattern repetition of a starting object (*initiator*) at one scale, or applied as a *generator* at another. The fractal dimension is determined by generators. An example of this iterative process is shown in Fig. 3.1. The Koch Curve fractal generation starts with the definition of a simple initiator. This can be further divided into different sections, 4 in this case, and each section is 1/3 of the length of the initiator, which has a unit length of 1. In the second order of the Koch Curve, each of the 4 sections of the generator is replaced with the same shape. This results in a shape composed of 16 segments, each of wich with a size of 1/9 of the unit length. The total length of the second order curve is 16/9. The more the iteration continues, the longer the figure, becoming infinitely long.

3.2.2 Fractal Dimension

In 1967, Mandelbrot (Mandelbrot, 1967) discussed self-similar curves examining the *coastline paradox*: the property that the measured length of a

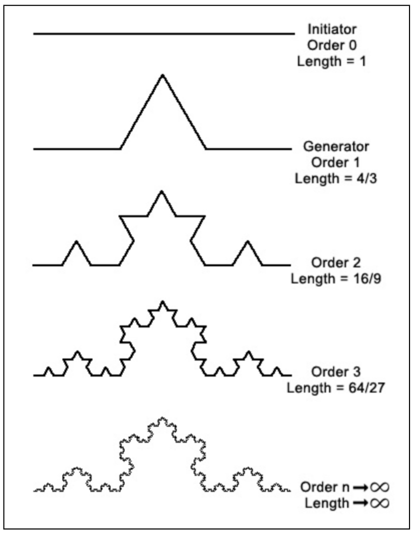

Figure 3.1: Generation of the Koch Curve fractal. The fractal can be made by starting with an initiator (order 0) and replacing every section of the pattern with a smaller copy of the initiator itself.

stretch of coastline depends on the scale of measurement ϵ. In particular, the length of the coast is increased indefinitely as ϵ is getting smaller and smaller. Mandelbrot concluded that the total perimeter length of a coast line L is equal to

$$L(\epsilon) \sim B\epsilon^{1-D} \tag{3.17}$$

with B a constant and D an exponent variable as the measured coast changes. The length of the coast can be considered as proportional to N times the specific scale ϵ, then the total length can be calculated as

$$L(\epsilon) \sim B\epsilon^{1-D} = B\epsilon^{-D}\epsilon = N(\epsilon)\epsilon \tag{3.18}$$

$$\Rightarrow N(\epsilon) = B\epsilon^{-D} \tag{3.19}$$

Adding the concept of self-similarity, Mandelbrot expressed a new relationship by a general definition of number and size distribution

$$N(A > \alpha) = C\alpha^{-D} \tag{3.20}$$

where the right term is the cumulative total number of islands with an area A larger than a possible value α, C is a proportionality constant, and D is the fractal dimension. This number defines the measure to which the fractal fills a space.

This theory can be applied in the context of soil particle sizes as follows

$$N(R > r) = Cr^{-D_F} \tag{3.21}$$

where $N(R > r)$ is the number of particles with a linear dimension R greater than r, C is a constant value, and D_F is the fragmentation fractal dimension. Taking into account the self-similarity of a system, the comparison between the size-frequency distribution of an object $N(r)$ and the cumulative distribution, $N(R < r)$ can be written including the k-iterations needed to form the fractal object as

$$N(r_k) = C(r_k)^{-D} \tag{3.22}$$

for k=0,1,...,∞.
In the context of this research, the cumulative form of Eq. 3.22 is preferred compared to the number-size density distribution. The reason is that we are interested in characterizing particle populations and a cumulative form can apply to discrete objects larger than a specific radius R (Perfect, 1997). Eq. 3.22 becomes thus a scalar-invariant relationship

$$N(r > R) = kR^{-D} \tag{3.23}$$

where $N(r > R)$ is the cumulative number of objects of length r larger than a specific R, k is a constant equivalent to the number of elements at a unit length scale, and D is the fractal dimension.

3.2.3 Fractal Fragmentation Model

As shown in the previous sections, the fragmentation looks like a complex mechanism found ubiquitously in nature. It is also strongly related to fractals since they are the cause of its self-similarity and scale-invariant events. To explain this connection, Turcotte (Turcotte, 1986) proposed a fragmentation model based on fractal theory.
The starting point of this model is that the fragmentation of a given material is due to the propagation of preexisting fractures and damages under applied stress (Allegre et al., 1982). Turcotte began considering a cubic particle of h×h×h side dimensions (see Fig. 3.2).

The cube is divided into eight equal cubes of size h/2 with a probability of catastrophic fragmentation p_c. Each of these has the probability p_e of experiencing a further fragmentation into eight daughter elements of size length h/4, which themselves may be further divided into eight cubes. The probability of fracture p_c is constant in this iterative process, and this latter can be repeated at infinitely logarithmically-spaced smaller scales. This model

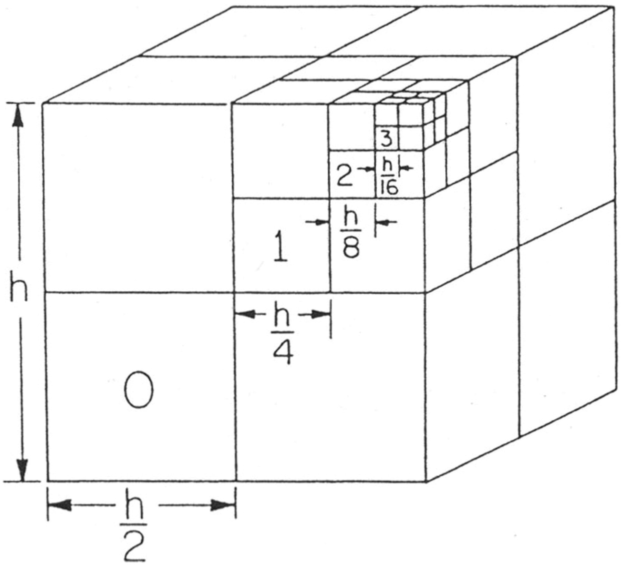

Figure 3.2: Turcotte's cube after the Renormalization Group (RG) approach application. It represents the initial intact cube and the resulting fractal model occurring by the process of fragmentation.

is based on the Renormalization Group (RG) approach, according to which each resulting daughter is assumed to be different from its parent fragment only by a constant scaling factor. The RG approach refers to a mathematical apparatus that allows systematic investigation of the changes of a physical system as viewed at different distance scales.
Let us consider h_0 and h_1 as the length of the initial cube and the daughter particle respectively. The two factors are related by a constant reductive factor a

$$h_1 = ah_0 \tag{3.24}$$

and after i iterations, the geometric progression transforms Eq. 3.24 in

$$h_{i+1} = ah_i \tag{3.25}$$

$$h_i = a^i h_0 \tag{3.26}$$

Mass conserving was the initial assumption for fragmenting the parent cube, and the catastrophic probability of fragmentation p_c has been considered constant. When the initial mass is passed successively at another iteration to smaller scale, it must be exponentially decreased. Assuming unitary density, the mass of the cube is equal to its volume, which is in turn dependent to the length h such that $V = h^3$.

Introducing the mass concept in the fractal fragmentation model, this leads to

$$M_1 = p_c M_0 \tag{3.27}$$
$$M_{i+1} = p_c M_i \tag{3.28}$$
$$M_i = p_c^i M_0 \tag{3.29}$$

where M_0 is the total mass of the initially cube of side length h_0, and M$_i$ is the total cumulative mass at size i.
Since $a^x = b \Rightarrow x = log_a b$ and solving for i gives:

$$\frac{log\left(\frac{M_i}{M_0}\right)}{log(p_c)} = \frac{log\left(\frac{h_i}{h_0}\right)}{log(a)} \tag{3.30}$$

By removal of logarithms and substituting $\nu = log(p_c)/log(a)$,

$$\frac{M_i}{M_0} = \left(\frac{h_i}{h_0}\right)^{\nu} \tag{3.31}$$

Equation 3.31 is a fundamental relationship which completely describes the nature of a scale-invariant fragmentation. In fact, the dependence between the cumulative mass M_i at the i^{th} iteration and the ratio between sizes raised power ν, satisfies the power-law condition.

For mass conservation assumption, the initial mass of the cube M_0 must be equal to the total mass of the final fragments. The total mass is related to the largest observable fragment of size h_0, which is considered the upper size limit of the distribution. In this context, Eq. 3.31 becomes (Tyler and Wheatcraft, 1992)

$$\frac{M_{(r<R)}}{M_T} = \left(\frac{R}{R_{upper}}\right)^{\nu} \tag{3.32}$$

where $M_{(r<R)}$ is the cumulative mass with linear size smaller than a specific value R, M_T is the total cumulative mass up to the upper observable limit (R_{upper}), and ν is a constant exponent.
Since it is not alway possible to have information about the initial mass of a fragmented system, the upper mass limit in Eq. 3.32 must be removed, and the equation becomes

$$M(r < R) = cR^v \tag{3.33}$$

To link the mass and size distributions with the volume, the probability density functions can be obtained deriving the Eq.s 3.23 and 3.33

$$\frac{dN}{dR} = R^{-D-1} \tag{3.34}$$

$$\frac{dM}{dR} = R^{v-1} \tag{3.35}$$

Since $M \propto V \propto R^3$, assuming a constant density $\rho = M/V$, we obtain

$$R^3 dN \propto dM \tag{3.36}$$

Combining equations 3.35 and 3.36, the following relationships are obtained:

$$R^3 dN \propto R^{v-1} dR \tag{3.37}$$

$$\frac{dN}{dR} = \frac{R^{v-1}}{R^3} \tag{3.38}$$

$$\Rightarrow R^{-3+v-1} = R^{-D-1} \tag{3.39}$$

Finally, $-D-1 = -3+v-1$ and

$$D = 3 - v = 3 - \frac{log(P_c)}{log(a)} \tag{3.40}$$

The fractal dimension D can also be related to the volume and surface area of the resulting fragments. The total volume of fragments can be calculated as

$$V = \int_{r_{min}}^{r_{max}} r^3 dN \sim \frac{1}{3-D}(r_{max}^{3-D} - r_{min}^{3-D}) \tag{3.41}$$

where r_{max} is the size of the object which has been fragmented, and r_{min} is a value controlled by the scale of the heterogeneity responsible for fragments. If $0 < D < 3$, it is not necessary to specify r_{min} because the volume is predominantly in the largest fragments. In contrast, if $D > 3$ the role of smaller particles is predominant.
The total surface area A of the fragments is similarly

$$A = C \int_{r_{min}}^{r_{max}} r^2 dN \sim \frac{C}{D-2}\left(\frac{1}{r_{min}^{D-2}} - \frac{1}{r_{max}^{D-2}}\right) \tag{3.42}$$

Considering the initial cube of density ρ_0 and initial length size r_0, the density of the fractal medium scale is finally calculated as follows:

$$\frac{\rho}{\rho_0} = \left(\frac{r_0}{r}\right)^{3-D} \tag{3.43}$$

3.3 Quantitative Analysis of Isolated Boulder Fields on Comet 67P

As described in the first chapter, the surface of the comet shows different terrains and surface features. The large blocks are one of the ubiquitous and most important geological features of 67P: these boulders can be found both isolated and in clusters, and their size distribution depends on the formation and evolution they have undergone (Pajola et al., 2015). Being exposed on the surface of the comet, these objects undergo intense thermal fatigue, and reveal imprints of erosional and geological processes (Ehlmann et al., 2008). It is therefore important to understand the origin of these boulders and what this means in the framework of cometary evolution.

In this section a method to quantitatively analyze boulder fields is shown. We are interested in characterizing isolated boulder populations that are unrelated to specific niches or detachment scarps. Boulders are scattered all over the surface of the comet, and we cannot be sure about their origin. These boulders could have been the result of past collapses or gravitational events. However, by discarding boulder populations originating from confirmed gravitational phenomena, we can investigate other types of fragmentation, such as the thermal fatigue and the sublimation of ices. Fragmentation processes on a cometary body are indeed thought to be the result of cumulated thermal fatigue (Pajola et al., 2017), propagating fractures within the material, and the combined effect of gravitational force (Pajola et al., 2015). It is important to note that the following analysis focuses on specific and confined areas within three regions of 67P, and the obtained results might not be representative of the entire regions.

3.3.1 Data Selection

We selected three areas (Fig. 3.3) located on the head, neck, and body of 67P, in order to study the correlation between boulder fragmentation and their location on the comet nucleus. The selected regions are Imhotep, Hapi, and Hatmehit respectively (Thomas et al., 2015b; El-Maarry et al., 2015).

The Hatmehit region is located on the small lobe at the equator, where the sublimation of ices can be strong and the erosion can be fast (Kossacki et al., 2015). The Hapi region is located in the northern hemisphere of 67P, in the neck that joins the large and small lobe of the comet. Because of its location and self-shadowing, Hapi experiences day-night cycles twice every comet rotation (Pajola et al., 2019) during the northern summer when the

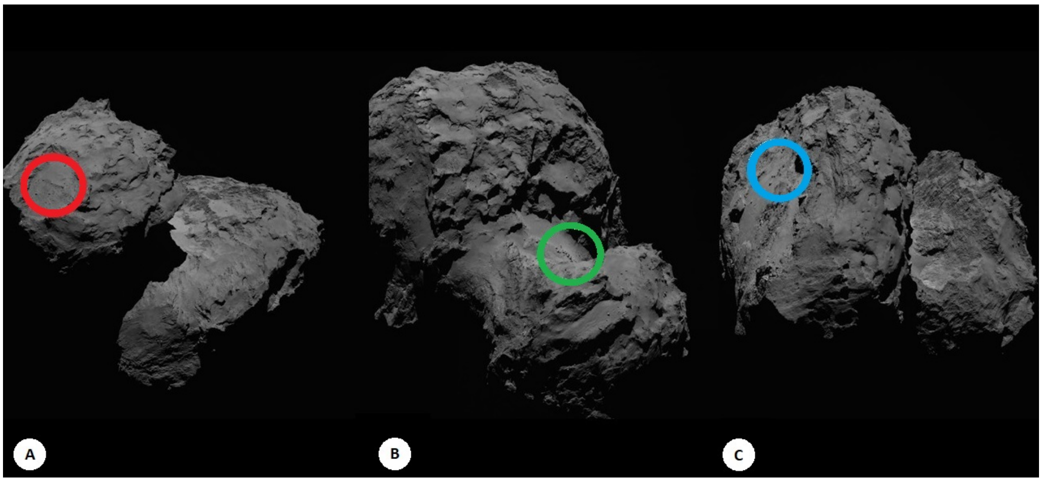

Figure 3.3: OSIRIS NAC images taken on 5 and 6 August, 2014 showing the location of the Hatmehit (A, red), Hapi (B, green), and Imhotep (C, blue) regions of 67P. The first image of this set (A) was taken at 23.19.25 UT at a distance of 123.3 km and a scale of 2.30 m/pixel. Image B was taken at 03.19.25 UT at a distance of 115.2 km and has a scale of 2.14 m/pixel, while the last one (C) was taken at 06.19.26 UT at a distance of 109.7 km and a scale of 2.04 m/pixel.

comet is at heliocentric distances >1.6 au pre-perihelion and > 2.6 au post-perihelion (Keller et al., 2015). Imhotep is a complex region located close to the cometary equator. It is illuminated daily from aphelion (5.7 au) to perihelion (1.2 au), and it is relatively flat compared to the shape of the nucleus (Auger et al., 2015). Because of its location, illumination conditions, and geomorphology, this region is a good candidate for investigating sublimation erosion close to perihelion. The size of boulders located in this region has no obvious correlation with the gravitational slope of the terrain on which they stand (Auger et al., 2015), and they vary widely in size, shape, and surface texture.

As mentioned in the previous paragraph, we focused on areas that are unrelated to detachment scarps and niches. To confirm that these populations are not altered by local gravitational slopes, we report the gravitational slope maps (Fig. 3.5, the centrifugal force is included), that is, the angle between the local surface normal and the vector opposite to the estimated acceleration fields (Penasa et al., 2017). All areas have gravitational slopes ranging between 0° and 20°, which is below the angle of repose of loose granular material on 67P, that is 30° (Vincent et al., 2015b).

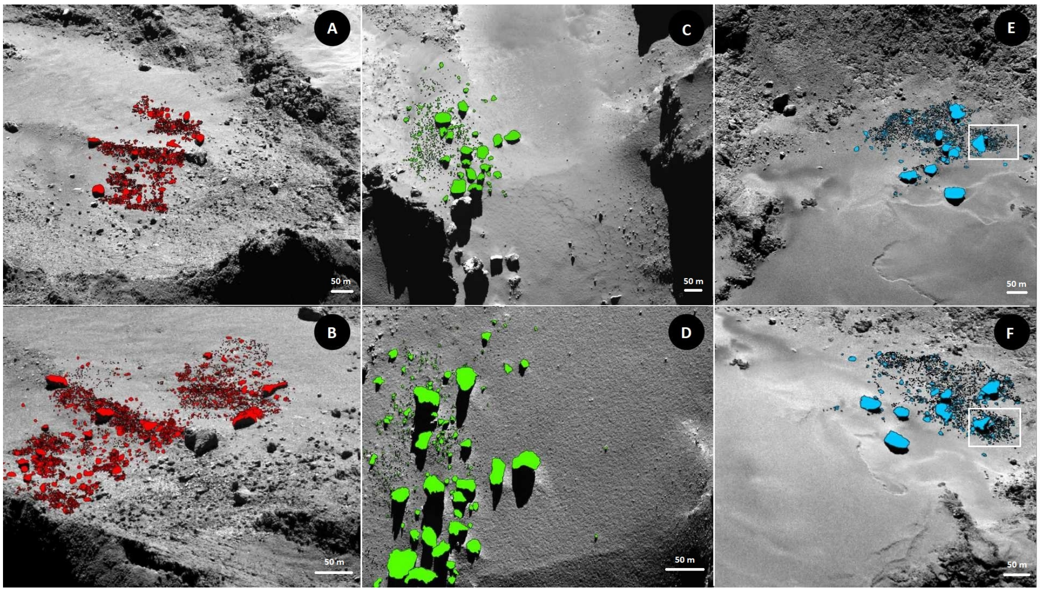

Figure 3.4: OSIRIS NAC pre- and post-perihelion images used in this work (see Table 3.1 for image ID). (**A**) OSIRIS NAC image taken on 12 December, 2014. The spatial scale of the image is 0.36 m/pixel. This area is located in the Hatmehit region. (**B**) OSIRIS NAC image taken on 23 July, 2016 with a spatial scale of 0.19 m/pixel. This area is located in the Hatmehit region. (**C**) OSIRIS NAC image taken on 10 December, 2014 with a spatial scale of 0.38 m/pixel. This area is located in the Hapi region. (**D**) OSIRIS NAC image taken on 20 July, 2016. The spatial scale of the image is 0.17 m/pixel. This area is located in the Hapi region. (**E**) OSIRIS NAC image taken on 29 September, 2014. The spatial scale of the image is 0.35 m/pixel. This area is located in the Imhotep region. (**F**) OSIRIS NAC image taken on 23 July, 2016 with a spatial scale of 0.28 m/pixel. This area is located in the Imhotep region. In panels E and F we highlight a detail of the Imhotep case study area.

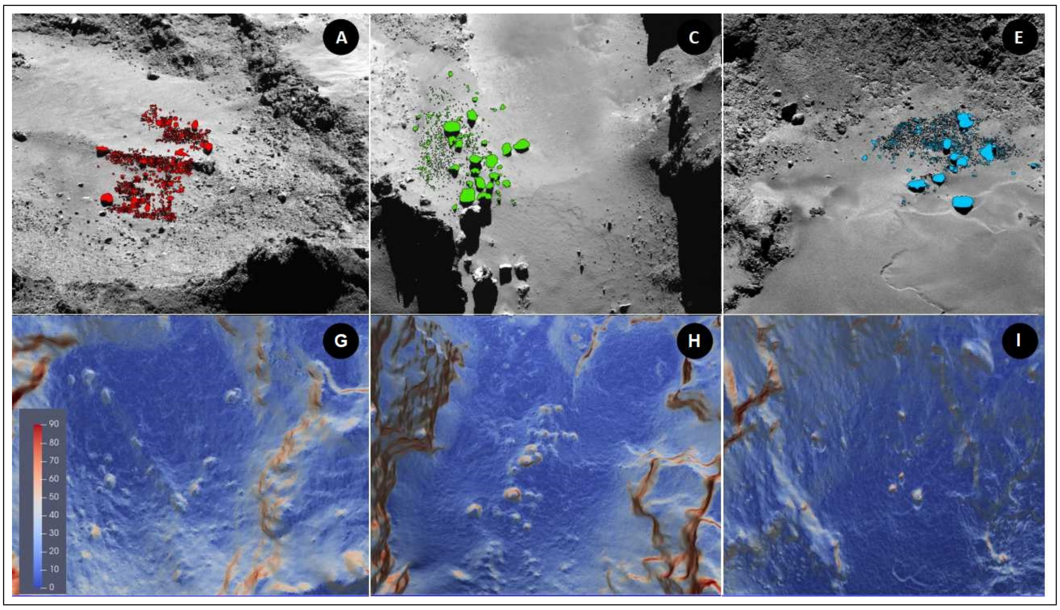

Figure 3.5: Gravitational slopes of the selected areas. Panels **A**, **C**, and **D** show the OSIRIS NAC pre-perihelion images used in this work (see Table 3.1) for image ID. In panels **G**, **H**, and **I** the related slopes maps are shown. The value ranges from 0 to 90 degrees.

3.3.2 Size-Frequency Distribution and Cumulative Fractional Area

Boulders on a rocky surface result from geological processes that have formed and altered the surface. Understanding the size-frequency distribution and the position of these objects is important because may lead to a better comprehension of the geologic history of the surface itself (Garvin et al., 1981). Boulder counting can be used to characterize surface properties (Tang et al., 2017) and the processes that result in fragmentation. Using orthorectified images from the OSIRIS-NAC, we derived the cumulative size-frequency distribution of three populations of boulders located in Hapi, Imhotep, and Hatmehit. In Fig. 3.4 the areas of interest are shown. Following the definition of "boulder" given by Pajola et al. (2015), we used the Arcgis 10.3.1 software (ESRI, 2011) to manually outline all positive reliefs detectable in multiple images obtained with different observing geometries. This software allows to measure the position of boulders on the surface, the corresponding projected area, and their mean long axis. We only considered fully resolved boulders, that is, features larger than 3 pixels (Pajola et al., 2015), to minimize the possibility of misidentification (Nyquist, 1928). This implies a boulder size of at least 1.08 meters on Hatmehit, 1.05 meters on Imhotep, and 1.14 meters on Hapi.

We performed our analysis on images acquired before and after the perihelion passage (13 August, 2015). Being the closest point of the comet's orbit to the Sun, the surface receives the largest quantity of insolation. Hence, it is expected that perihelion plays a fundamental role in terms of fragmentation. Pre- and post-perihelion images have a different spatial resolution because of the different spacecraft distance, which affects boulder mapping. To directly compare these two situations and to obtain a homogeneous data set, we used the lowest resolution images as reference, and degraded the highest resolution images to the same levels. The spatial reference scale for the Imhotep case study area is that obtained on 29 September, 2014, at 13:29 UT and is equal to 0.35 m/pixel. For the Hapi area we used a spatial scale of 0.38 m/pixel, derived from an image dated 10 December, 2014. For Hatmehit we used an image acquired on 12 December, 2014, with a spatial scale of 0.36 m/pixel. In Table 3.1 we present the observing log of the image dataset we used in this work. As displayed in the panels E and F of Fig. 3.4, a sub-population of the Imhotep region is highlighted (white boxes in Fig. 3.4 are used to indicate this particular). We decided to analyze both the entire population of the Imhotep region and this sub-population consisting of a main boulder surrounded by its smaller fragments (hereinafter 'detail') to compare this situation with the entire population, assuming that the fragments derive from the parent body.

Finally, we derived the cumulative fractional area, which is the curve of area covered by boulders versus diameter represented in a log-log plot (Golombek et al., 2003). As shown by Golombek and Rapp (1997), a general cumulative area distribution of blocks can be described by the following equation:

$$F(R) = CR^{-S}, \tag{3.44}$$

where $F(R)$ is the cumulative fractional area covered by blocks of a given diameter R or larger, C is a constant derived from the cumulative area covered by boulders greater than 3 pixels, and S is a parameter that explains how abruptly the area covered by rocks decreases with increasing diameter.

3.3.3 Fractal Theory

As shown in the previous section, empirical data indicate that the size-frequency distribution of material expected from fractures and fragmentation follows a fractal rule (Bittelli et al., 1999). Fragmentation is caused by the propagation of fractures at different length scales (Li et al., 2017), and this

Image ID	Region	Day (UT)	Time (UT)	Spatial Scale (m/pixel)	Phase Angle (degree)	Incidence Angle (degree)	Emission Angle (degree)
A	Hatmehit	12-12-2014	17:42	0.36	95.34	8.76	88.91
B	Hatmehit	23-07-2016	17:53	0.19	101.81	16.47	87.79
C	Hapi	10-12-2014	06:29	0.38	91.79	31.79	99.84
D	Hapi	20-07-2016	08:02	0.17	89.02	71.65	25.16
E	Imhotep	29-09-2014	13:29	0.35	92.94	63.44	39.47
F	Imhotep	09-09-2016	11:25	0.28	89.95	56.38	44.93

Table 3.1: Observing log of the OSIRIS NAC images.

behavior can therefore be described by connecting the number of crack initiators with the fractal dimension. In this context, a fractal fragmentation model can be used to quantify and predict the size-frequency distribution of fragments produced by a given energy input. The size-frequency distributions can be interpreted as the fractal behavior of the boulder populations, produced by fragmentation processes, and the power-law exponent determined by the size-frequency analysis can be interpreted as a fractal dimension.
The size-frequency distribution of the boulders for an area combines the number of counted boulders N and their size R, with the relation (Mandelbrot, 1983; Matsushita et al., 1985; Turcotte, 1986)

$$N(R) = kR^{-D} \tag{3.45}$$

where $N(R)$ is the number of boulders with a diameter larger than a fixed value R, k is a constant proportionality, and D is the power-law exponent. D characterizes the population itself and the degree of fragmentation. Eq. 3.45 can also be interpreted as the number of elements N at the R-th level in the hierarchy of a fractal system, k is the number of crack initiators of unit length, R represents the element size, and D is the fractal dimension (Mandelbrot, 1983).
To verify the fractal behavior of the analyzed populations, we used the box-count approach (Smith et al., 1989; Miloevic et al., 2013), which is a common method for analyzing complex patterns and to determine their fractal dimension in a Euclidean space. The image is overlaid with a grid (Miloevic et al., 2013) and is subdivided into progressively smaller squares. Then, each box is checked to determine whether it contains any boulders. At each scale a different number of boxes N will contain boulders, and that number is used

to obtain the fractal dimension. If $N(r)$ is the number of boxes of side length r required to cover the image, the fractal dimension D_f is defined as

$$D_f = lim_{r \longrightarrow 0} \frac{log(N(r))}{log(1/r)} \tag{3.46}$$

If the definition of limit is not met and this limit does not exist, the analyzed image does not show fractal behavior.

3.3.4 Shape of Boulders

The primary measuring information of image analysis is the projected area of a boulder, which contains key information about both the boulder size and shape. The shape of boulders may provide indications on geological processes that leave morphological marks on rock surfaces at different spatial scales (Viles, 2001). The original shape of a particle, its lithology, its composition, and the duration of the processes responsible for the erosion are the main influencer on its final shape. In particular, the lithology of a block is the primary factor that constrains whether and how a particle breaks (Yingst et al., 2007). The shape of a boulder can be quantitatively described by shape factors, which are dimensionless quantities independent of boulder size. They represent the degree of deviation from an ideal shape, such as circle or sphere, and are calculated from measured dimensions, such as diameter (d), perimeter (P), area (A), and major (a) and minor (b) axis. The shape factors used in this study are described below.

SHAPE FACTORS to describe a boulder

- *Elongation*: the major-to-minor axis ratio of a particle (i.e., the projection of its shape) is defined by

  $$E = b/a, \tag{3.47}$$

  where a and b are the major and minor axis respectively.

- *Cox Circularity*: the measure of how closely a polygon shape matches that of a circle is defined by the Cox circularity. These parameters indicate the presence or absence of edges and corners and may therefore describe if the polygon has a relatively simple boundary with vertices that are relatively equidistant from the centroid. This parameter is defined as:

  $$Circ = 4\pi A/P^2, \tag{3.48}$$

  where A is the area, and P is the perimeter.

- *Solidity*: if A is the area, and H is the convex hull area of the shape (Ballan et al., 2005)), the solidity describes the extent to which the shape is convex or concave. In particular, it expresses how the border is ruffled or how many concave cavities are on the surface and is defined as follows:
$$S = A/H. \tag{3.49}$$
The convex hull is defined as the smallest convex region that contain the polygon, constructed by connecting a subset of the polygon vertices.

- *Feret diameter*: the size of an object along a specified direction is quantified by the Feret diameter (d_f). In general, it can be defined as the distance between the two parallel planes that restrict the object perpendicularly to that direction.

In addition to these parameters, another important particle shape factor is its *sphericity.* This is the measure of how closely the shape of an object approaches that of a mathematically perfect sphere. This is a three−dimensional parameter that can be estimated by measuring only two dimensions of a particle. This is possible because the correlation coefficient between sphericity values calculating two to three dimensions is 0.85 (Riley, 1941). Defined by Wadell (1933), the sphericity Ψ of a particle is the ratio of the surface area of a sphere, which has the same volume as the given particle, to the surface area of the particle. To address the problem of the dimensionality, particle sphericity has been defined in various ways (Zheng and Hryciw, 2015). The four most commonly used formulations are

- *the area sphericity,*
$$\Psi_1 = \frac{A_s}{A_{circ}}, \tag{3.50}$$
where A_s is the projected area of a particle, and A_{circ} is the area of the minimum circumscribing circle.

- *The diameter sphericity*,
$$\Psi_2 = \frac{D_c}{D_{circ}}, \tag{3.51}$$
where D_c is the diameter of a circle that has the same projected area as the particle, and D_{circ} is the diameter of the minimum circumscribing circle.

- *The circle ratio sphericity*,
$$\Psi_3 = \frac{D_{ins}}{D_{circ}}, \tag{3.52}$$

where D_{ins} is the diameter of the largest inscribing circle and D_{circ} is the diameter of the minimum circumscribing circle.

- *The perimeter sphericity,*

$$\Psi_4 = \frac{P_c}{P_s}, \tag{3.53}$$

where P_c is the circumference of a circle that has the same projected area as the particle and P_s is the perimeter of the particle.

The method we present here was adapted to the specific limitations of data derived from boulders in the OSIRIS NAC images. To evaluate the boulder shape, we manually outlined every boulder on the selected image to fix the shape and to calculate the area of all boulders, their perimeter, and the major and minor axes. After the image mapping, we analyzed every shape through a Java program called *ImageJ* (Schneider et al., 2012) to quantify the shape parameters.

3.3.5 Error Sources

The poor pixel selection in outlining the border of the boulder represents one of the sources of error for particle shape analysis (Yingst et al., 2007). These errors depend on the capability of the analyst to create an accurate contour of the particle. Yingst et al. (2007) estimated uncertainty by the mean values of resulting morphologic parameters derived by each one of several operators. The resulting error is approximately 3% for sphericity and 20% for roundness. Analyzing pre- and post-perihelion images of the same regions, errors due to different incidence angles or inclination of the focal plane with respect to the target surface and the position of the spacecraft, are introduced. In this context, to assess the reliability of the shape parameter set, we performed two tests to validate our method.

Two-dimensional test

We created a test image containing different shapes, ranging from the simplest, like a circle, to the most complex, like a star (see Fig. 3.6). We rotated and tilted the image under different angles, varying the azimuth and the elevation angles of the view in order to simulate the real conditions of the observations. This process is equivalent to applying different homographies, increasing perspective (high elevation), or changing the image plane rotation (by changing the azimuth) to the image. We randomly rotated the image for the first test; we tilted the image by an azimuth angle of 120° and an

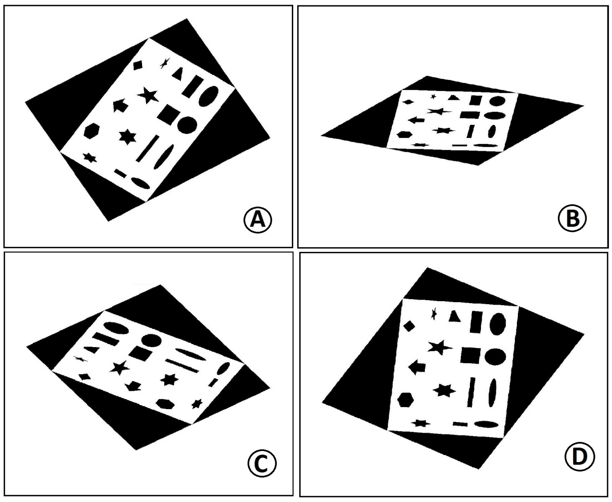

Figure 3.6: Variation in azimuth and elevation angle of the test image. (A) Random rotation of the test image. (B) Azimuth=120°, and elevation=20°. (C) Azimuth=55°, and elevation=40°. (D) Azimuth=120°, and elevation=50°.

elevation of 20° for the second test; used an azimuth of 55° and elevation of 40° for the third test; and finally, an azimuth angle of 120° and elevation of 50° for the last test. We repeated the test several times with different values of azimuth and elevation. Following the method described in the previous section, all the test images were then given as input to ImageJ for the shape detection and parameter measurements. Table 3.2 shows that the circularity and solidity are invariant shape factors. Their invariance allows us to use them to characterize the boulder populations.

Three-dimensional test

To quantify the biases introduced by measuring a two-dimensional projection of a three-dimensional object, we simulated a boulder field and accordingly measured the shape parameters. The surface has a cometary texture and is composed of 10 boulders, the sizes of which vary from 1 to 5 meters. Figure 3.7 shows an example of the synthetic boulder field. The shape of the boulders is random. We combined different emission and incidence angles to include shadows and to measure the shape at different observational geometries. The emission values are 0°, 20°, 35°, and 60°. The incidence angles are 0°, 30°, 45°, and 60°. The zero-emission and zero-incidence cases set the shape parameters, because they are able to measure them in a nadiral way. Table 3.3 shows that the results are consistent with the previous test, and

Image	Circ	S	Feret (pixel)	E	Sph1	Sph2	Sph3	Sph4
Original	0.55	0.86	698.28	0.57	0.45	0.65	0.46	0.76
Random	0.54	0.85	83.85	0.55	0.46	0.66	0.46	0.75
120° - 20°	0.54	0.85	61.21	0.44	0.34	0.56	0.36	0.72
55° - 40°	0.54	0.85	80	0.45	0.49	0.65	0.47	0.83
120° - 50 °	0.55	0.85	80.55	0.57	0.47	0.47	0.47	0.77
Mean	0.54	0.85	80.55	0.55	0.46	0.65	0.46	0.76
Stdev	0.01	0.01	278.25	0.07	0.06	0.08	0.05	0.04

Table 3.2: Shape parameters determined with the synthetic image test, including circularity (Circ), solidity (S), Feret's diameter (Feret), elongation (E), and the four formulations of sphericity (Sph). Mean values and standard deviations are shown.

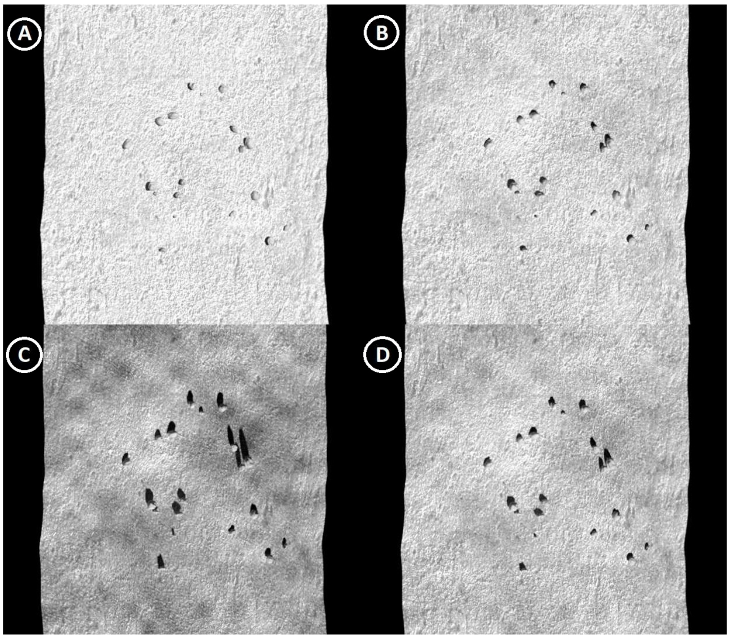

Figure 3.7: Simulation of a boulder field composed of 10 boulders. (A) Emission=0°, and incidence=0°. (B) Emission=0°, and incidence=30°. (C) Emission=0°, and incidence=45°. (D) Emission=0°, and incidence=60°.

Image	Circ	S	Feret (pixel)	E
Em=0 In=0	0.89	0.96	44.56	0.81
Em=0 In=30	0.79	0.94	53.94	0.68
Em=0 In=45	0.79	0.93	51.65	0.71
Em=0 In=60	0.83	0.95	58.70	0.78
Em=20 In=0	0.86	0.95	43.57	0.75
Em=20 In=30	0.86	0.96	52.88	0.63
Em=20 Inc=45	0.84	0.95	53.60	0.66
Em=20 Inc=60	0.87	0.95	42.68	0.73
Em=35 In=0	0.86	0.95	41.81	0.66
Em=35 In=30	0.85	0.94	40.09	0.55
Em=35 In=45	0.82	0.95	73.11	0.58
Em=35 In=60	0.86	0.94	32.56	0.63
Em=60 In=0	0.86	0.96	55.27	0.41
Em=60 In=30	0.85	0.95	40.97	0.34
Em=60 In=45	0.85	0.94	41.81	0.40
Em=60 In=60	0.86	0.95	41.55	0.39
Mean	0.85	0.95	48.40	0.60
Stdev	0.03	0.01	9.77	0.15

Table 3.3: Shape parameters resulting from the three-dimensional test. Circularity (Circ), solidity (S), Feret's diameter (Feret), and elongation (E) are listed. Mean values and standard deviations are shown.

the solidity and circularity are invariant even in this test.

3.3.6 Results

Size-frequency distribution and cumulative fractional area

By excluding boulders with diameters smaller than 3 pixels, a power-law function can be used to fit the data from each boulder population to represent the general form of the size-frequency distribution:

$$n(R) = kR^{-D}, \tag{3.54}$$

where $n(R)$ is the cumulative density of boulders per km^2 with diameter larger than R. K and D are constants. The cumulative distribution is approximately linear, and we applied a nonparametric statistical method (e.g.,

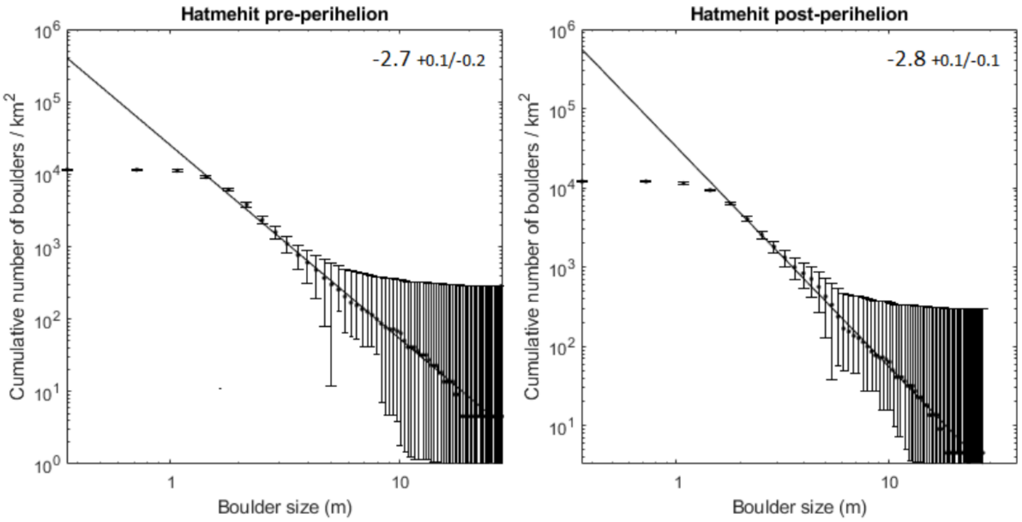

Figure 3.8: Cumulative size-frequency distribution of boulders per km^2. The left panel refers to the Hatmehit pre-perihelion image, and the right panel refers to the Hatmehit post-perihelion image. The vertical error bars indicate the root of the cumulative number of counting boulders. The fitted regression curves have a power-law index of -2.7 +0.1/-0.2 and -2.8 +0.1/-0.1.

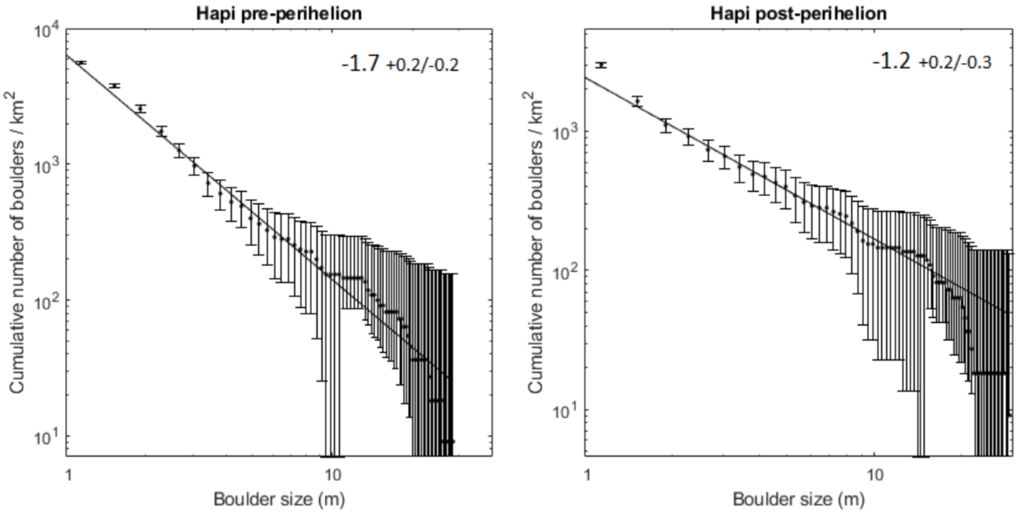

Figure 3.9: Same as Fig. 3.8 for Hapi. The fitted regression curves have a power-law index of -1.7 +0.2/-0.2 and -1.2 +0.2/-0.3.

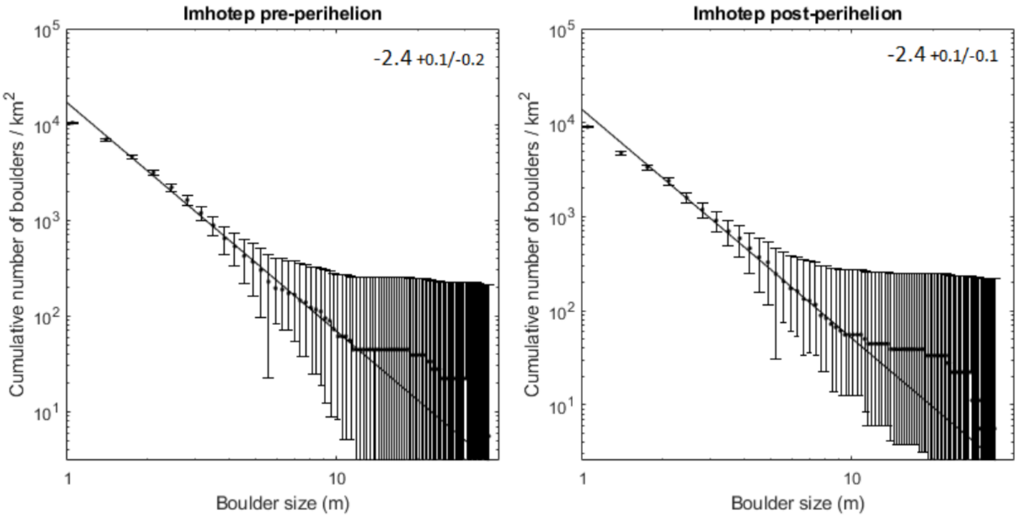

Figure 3.10: Same as Fig. 3.8 for Imhotep. The fitted regression curves give a power-law index of -2.4 +0.1/-0.2 and -2.4 +0.1/-0.1.

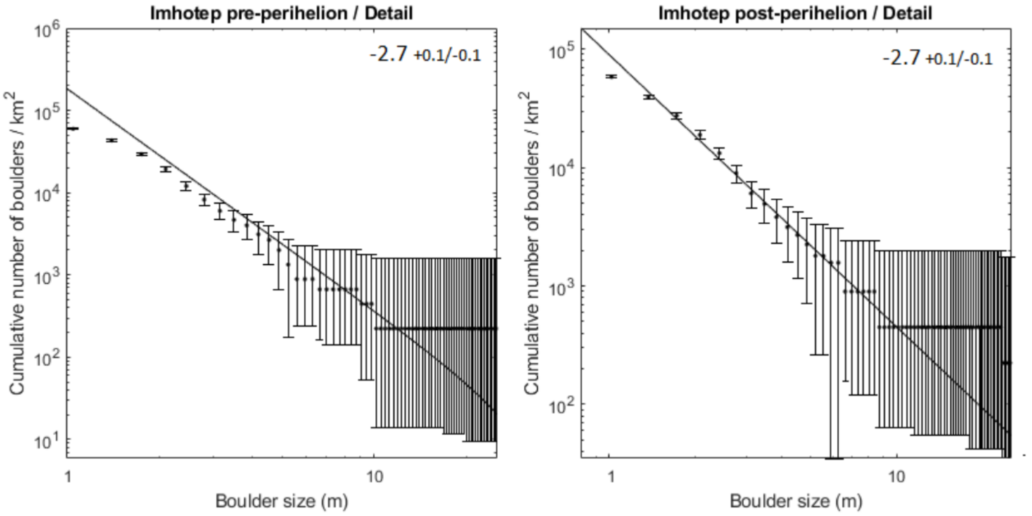

Figure 3.11: Same as Fig. 3.8 for Imhotep (detail). The fitted regression curves have a power-law index of -2.7 +0.1/-0.1 and -2.7 +0.1/-0.1.

Kolmogorov-Smirnov method) to find the slope of the cumulative distribution (for the method, see Lamy et al. (2004); also Pajola et al. (2017)). We derived the cumulative size-frequency distribution per km^2 using the equivalent area computed from the 3D shape model of 67P (Preusker et al., 2017). For each size-frequency distribution we used a constant bin-size of 0.35 m, 0.36 m, and 0.38 m for the Imhotep, Hapi, and Hatmehit study areas, respectively. This corresponds to the size of the pixel resolution of the OSIRIS NAC images.

The total number of identified boulders in this analysis is 11811, of which 4581 belong to the Imhotep case study area, 641 to the Imhotep detail, 1402 to the Hapi case study area, and 5187 to the Hatmehit study area. The cumulative boulder size-frequency distribution per unit area on the Hatmehit area has a power index of -2.7 +0.1/-0.2 before perihelion and -2.8 +0.1/-0.1 after perihelion. The Imhotep population shows a power-law trend with an index of -2.4 +0.1/-0.2 before perihelion, and -2.4 +0.1/-0.1 after perihelion. The results for the detail of the Imhotep boulder population (see Fig. 3.4, panel E) show a power index in the pre-perihelion image equal to -2.7 +0.1/-0.1, and -2.7 +0.1/-0.2 for the post-perihelion picture. The Hapi study area shows a power index of -1.7 +0.2/-0.2 before the perihelion passage, and -1.2+0.2/-0.3 after the perihelion passage. In Table 3.4 we summarize the power-law indices for the areas we analyzed. In Figs. 3.8, 3.9, 3.10, and 3.11, the cumulative size-frequency distributions of boulders per km^2 are shown. We also included the total number of counted boulders, the area calculated trough triangulating the boulder point cloud on the 3D shape model, the corresponding fragmented area, the minimum, the maximum, and the average diameters. The squared correlation R^2 resulting from the least-squares fit of Eq. 3.54 is larger than 98% for all of the cases.

Finally, we analyzed the cumulative fractional area, i.e. the area covered by boulders with a diameter larger than R as a function of the diameter itself. As shown in Table 3.5, these distributions can be fit by the following power-law equation:

$$F(R) = CR^{-S(R)}, \tag{3.55}$$

where $F(R)$ is the cumulative fractional area covered by boulders with diameters equal to or larger than R, C represents the total area covered by all boulders, and $S(R)$ indicates how abruptly the area covered by boulders decreases with increasing size. We found that the Hatmehit and Imhotep areas show a cumulative fractional area that is well fit by a power law, as expected. The Hapi case study area instead shows a lower value of the square correlation. This suggests that this population does not cover the area in the

Region	# (..)	A (km^2)	%A (%)	Min (m)	Max (m)	Avg (m)	D (..)	+ΔD (..)	-ΔD (..)
Hatmehit (pre)	2538	0.22	30	0.41	27.65	1.91	-2.7	0.1	0.2
Hatmehit (post)	2649	0.22	26	0.39	28.21	1.86	-2.8	0.1	0.1
Hapi (pre)	692	0.11	16	0.43	28.14	2.10	-1.7	0.2	0.2
Hapi (post)	710	0.11	30	0.27	28.66	1.53	-1.2	0.2	0.3
Imhotep (pre)	2192	0.18	18	0.40	36.53	1.62	-2.4	0.1	0.2
Imhotep (post)	2389	0.18	17	0.32	33.76	1.28	-2.4	0.1	0.1
Imhotep detail (pre)	300	0.0045	96	0.40	31.45	1.69	-2.7	0.1	0.1
Imhotep detail (post)	340	0.0045	98	0.32	29.05	1.44	-2.7	0.1	0.2

Table 3.4: Results from the size-frequency distributions analysis. We list the name of the selected region, the area (A), and the corresponding fragmented area (%A), the total number of boulders #, the minimum and maximum diameter (Min, Max), the average diameter (Avg), the power-law index (D), and the associated errors (+ΔD, -ΔD).

Region	Trend line	R^2
Hatmehit pre	y=0.0632$x^{-0.792}$	0.9942
Hatmehit post	y=0.0594$x^{-0.639}$	0.9875
Hapi pre	y=0.0648 $x^{-0.179}$	0.9120
Hapi post	y=0.0556$x^{-0.150}$	0.8545
Imhotep pre	y=0.0697 $x^{-0.364}$	0.9945
Imhotep post	y=0.0548 $x^{-0.378}$	0.9910
Imhotep detail pre	y=0.0041 $x^{-0.377}$	0.9865
Imhotep detail post	y=0.0032 $x^{-0.496}$	0.9908

Table 3.5: Trend lines and square correlations of the cumulative fractional area distributions.

same way.

Fractal behavior

To further investigate whether the analyzed boulder populations can be described by a fractal law, we used the box-count method. The aim of this approach is to quantify the fractal scaling, although this factor is not always known a priori. The calculation begins with an arbitrary number of boxes of size r. These elements are then applied to the dataset and counted. This optimized way of cutting an image will reveal the scaling factor.
The number N of boxes of size r needed to cover the set follows a power law:

$$N = N_0 r^{-D_f}, \tag{3.56}$$

with D_f the fractal dimension. Applying the algorithm, we determined the number of boxes N as a function of the size r, and it is represented by a solid line in Figs. 3.12, 3.13, 3.14, and 3.15. In the same figure, the scaling law $n \propto r^{-2}$ (required to completely space-fill a 2-dimensional image) is represented by a dashed line. A clear separation between the two curves indicates a possible fractal behavior of the data set.

The analyzed populations seem to be fractal at all sizes, without differences before and after the perihelion passage. The Hapi distribution, however, does not show a fractal behavior at large sizes. Table 3.6 lists the resulting fractal dimensions D_f .

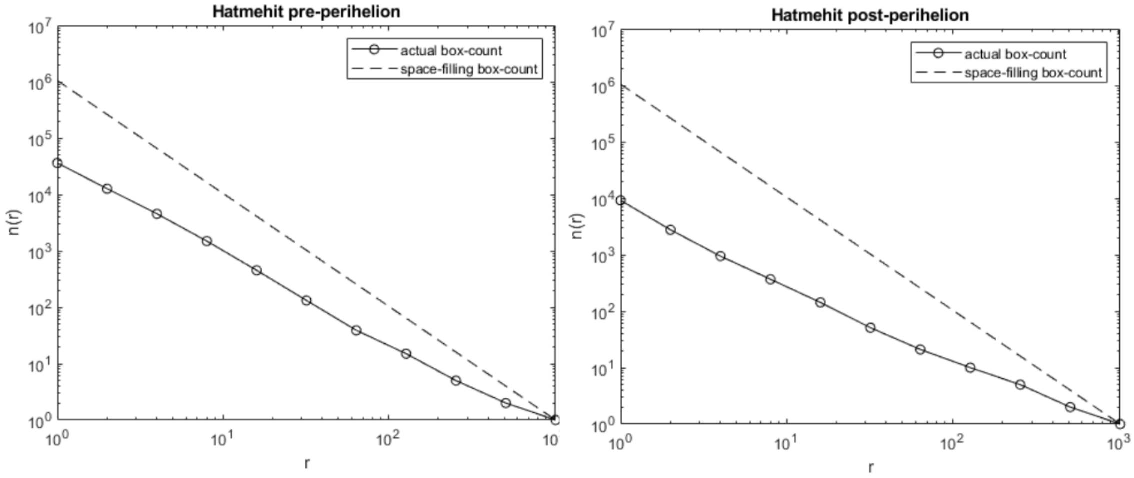

Figure 3.12: Results of the box-count method for the Hatmehit region. The dashed line shows the scaling $n \propto r^{-2}$ expected for a space-filling 2D image. The solid line represents the power law $N = N_0 r^{-D_f}$. The possible fractal behavior of the dataset is indicated by the discrepancy between the two curves.

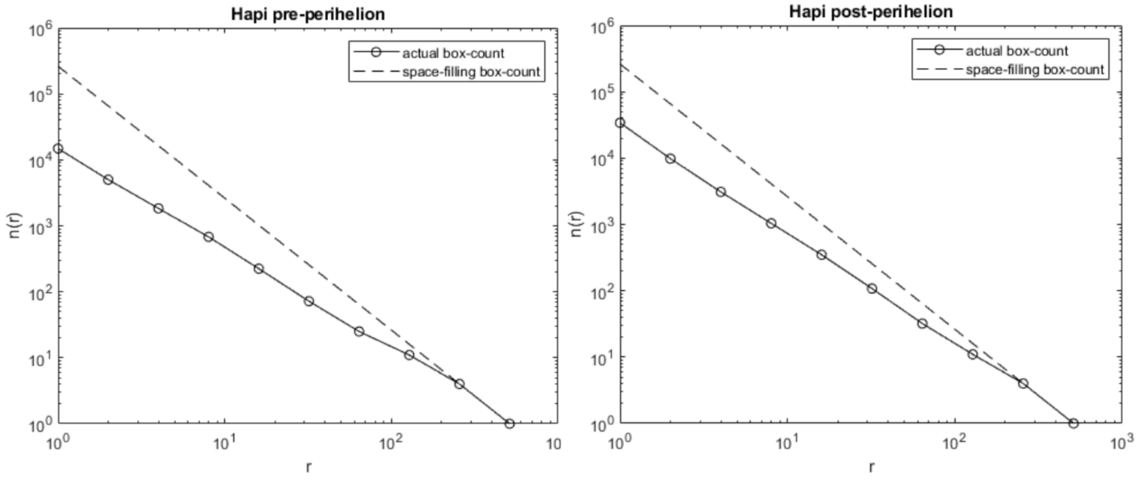

Figure 3.13: Results of the box-count method for the Hapi region. The dashed line shows the scaling $n \propto r^{-2}$ expected for a space-filling 2D image. The solid line represents the power law $N = N_0 r^{-D_f}$. The possible fractal behavior of the dataset is indicated by the discrepancy between the two curves.

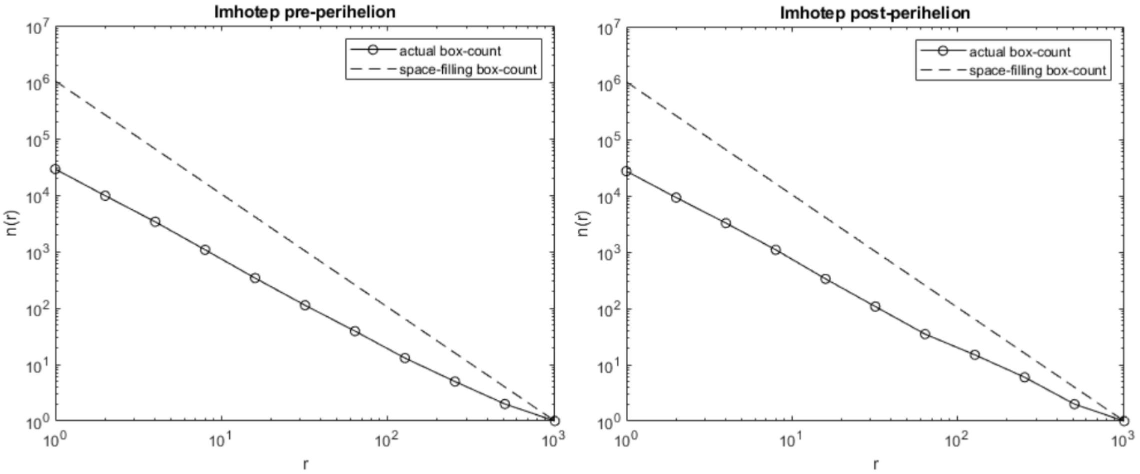

Figure 3.14: Results of the box-count method for the Imhotep region. The dashed line shows the scaling $n \propto r^{-2}$ expected for a space-filling 2D image. The solid line represents the power law $N = N_0 r^{-D_f}$. The possible fractal behavior of the dataset is indicated by the discrepancy between the two curves.

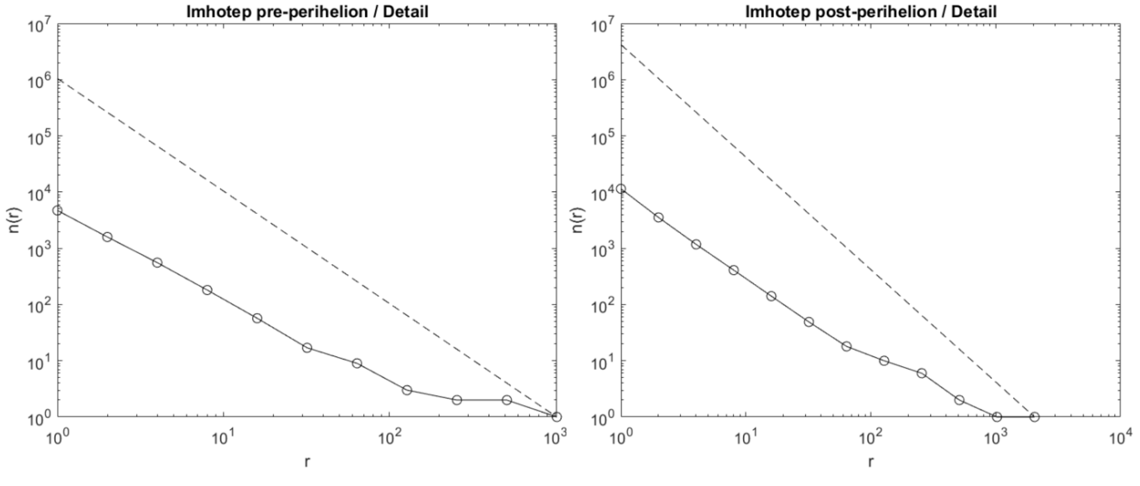

Figure 3.15: Results of the box-count method for the Imhotep (detail) area. The dashed line shows the scaling $n \propto r^{-2}$ expected for a space-filling 2D image. The solid line represents the power law $N = N_0 r^{-D_f}$. The possible fractal behavior of the dataset is indicated by the discrepancy between the two curves.

Region	D_f	StDev
Hatmehit pre	1.64	0.17
Hatmehit post	1.54	0.21
Hapi pre	1.48	0.18
Hapi post	1.44	0.08
Imhotep pre	1.55	0.11
Imhotep post	1.50	0.22
Imhotep detail pre	1.30	0.52
Imhotep detail post	1.23	0.72

Table 3.6: Results from box-count analysis. We list the name of the region, the fractal dimension D_f, and the associated standard deviation.

Boulder shape

The quantitative shape factors can provide a powerful method for assessing the geological history of the surface when the data provision is limited (Yingst et al., 2007). The mean value of each boulder shape factor is considered representative of the entire population. Table 3.7 shows that the average solidity of boulders ranges from 0.87 to 0.89. The concept of circularity is strictly connected to the compactness and complexity of a particle. The values range from 0.83 to 0.92, and this means that boulders at all sites are generally compact and there are small cavities at the edge of the boulders. We graphically represent the values of circularity and solidity for all populations (Fig. 3.16).

Finally, we report a comparison between circularity, solidity, and boulder size for each population (Figs. 3.17, 3.18, 3.19, and 3.20). The trend lines show that the circularity and solidity decrease with increasing diameter. This result would be consistent with the fragmentation process due to thermal fatigue. This process removes facets and corners and rounds smaller features more quickly because they are characterized by fewer sensing elements.

3.4 Discussion

From our analysis of 11811 boulders we found differences between the Imhotep, Hapi, and Hatmehit study areas in size-frequency distribution, cumulative fractional area, and fractal analysis. The fractal mathematical approach applied to the size-frequency distribution allows to characterize par-

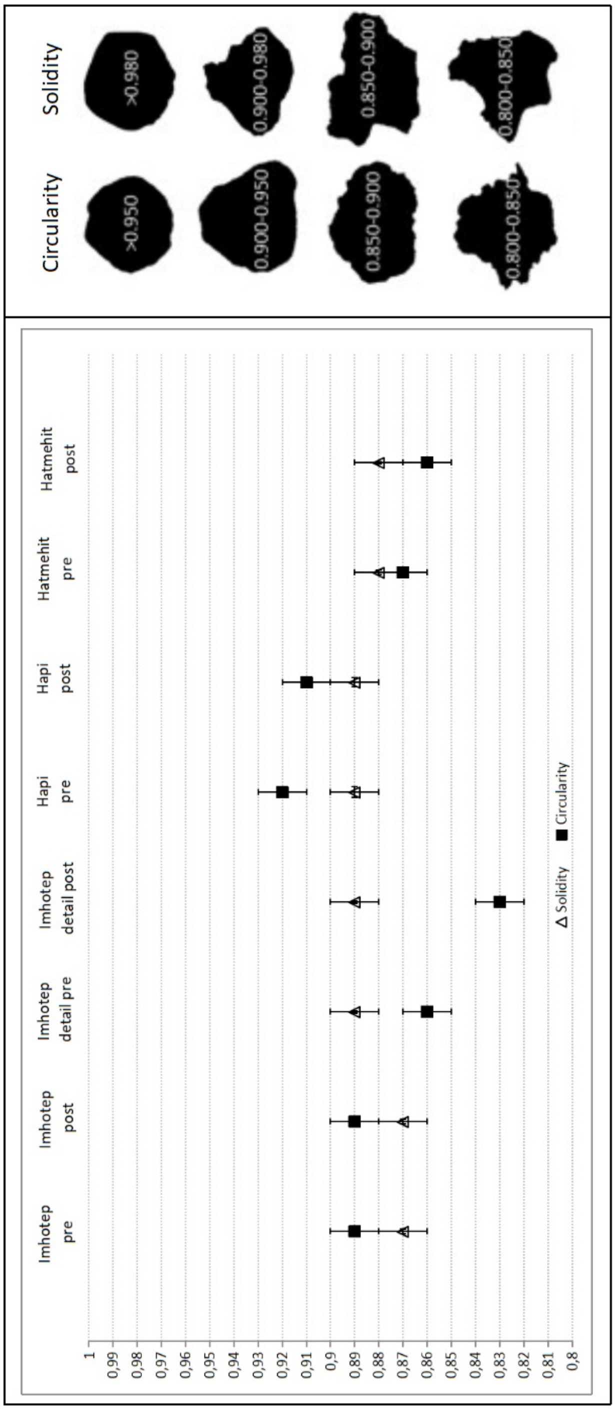

Figure 3.16: Graphical representation of circularity (square) and solidity (triangle). The average values of these shape parameters suggest boulders with a moderate circularity and solidity. These values are considered as representative of the entire populations.

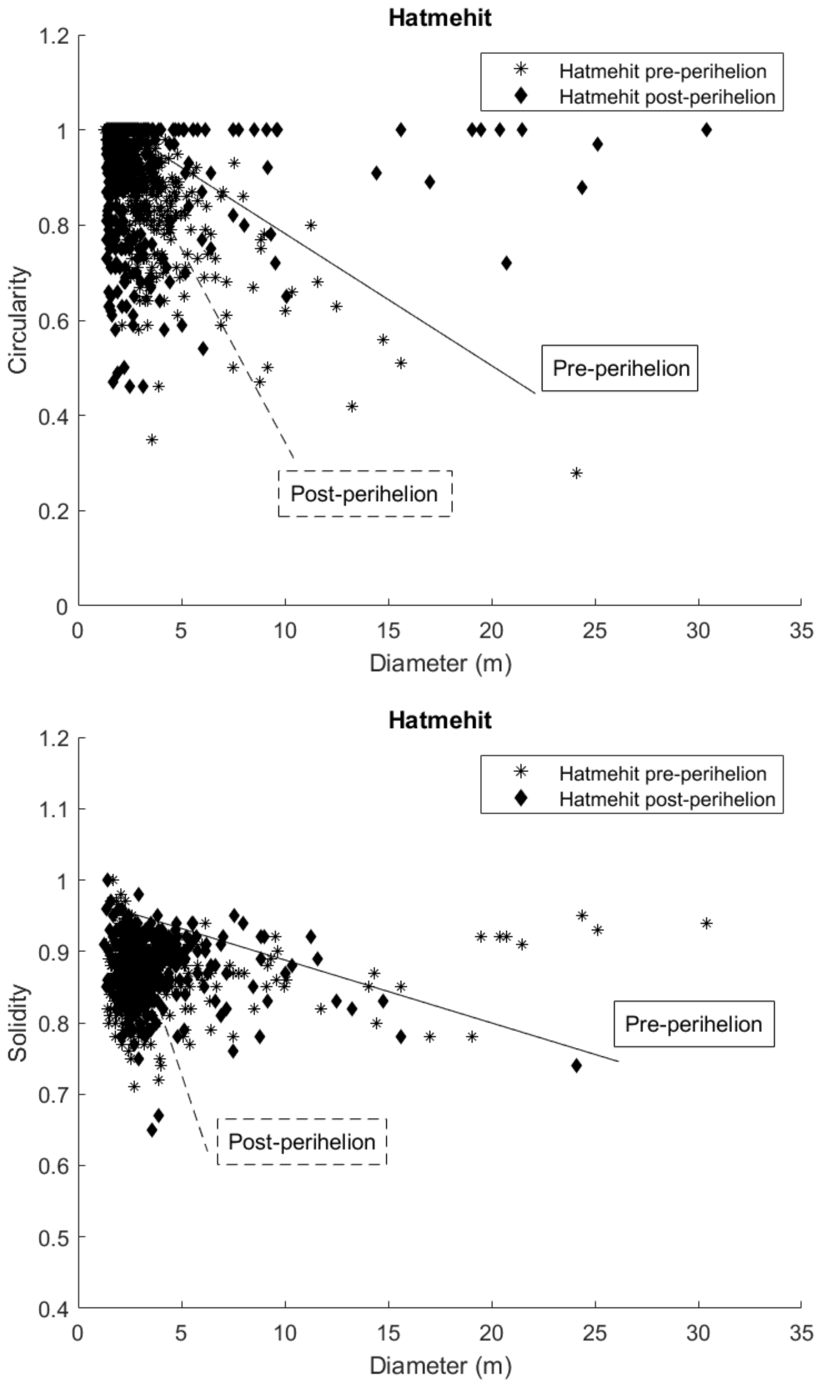

Figure 3.17: Comparison between circularity, solidity, and boulder size. The upper panel refers to the circularity, and the lower panel refers to the solidity. The stars represent the Hatmehit pre-perihelion case (the solid line is the corresponding trend line), and the diamond represents the Hatmehit post-perihelion case. The dotted trend line refers to the post-perihelion case.

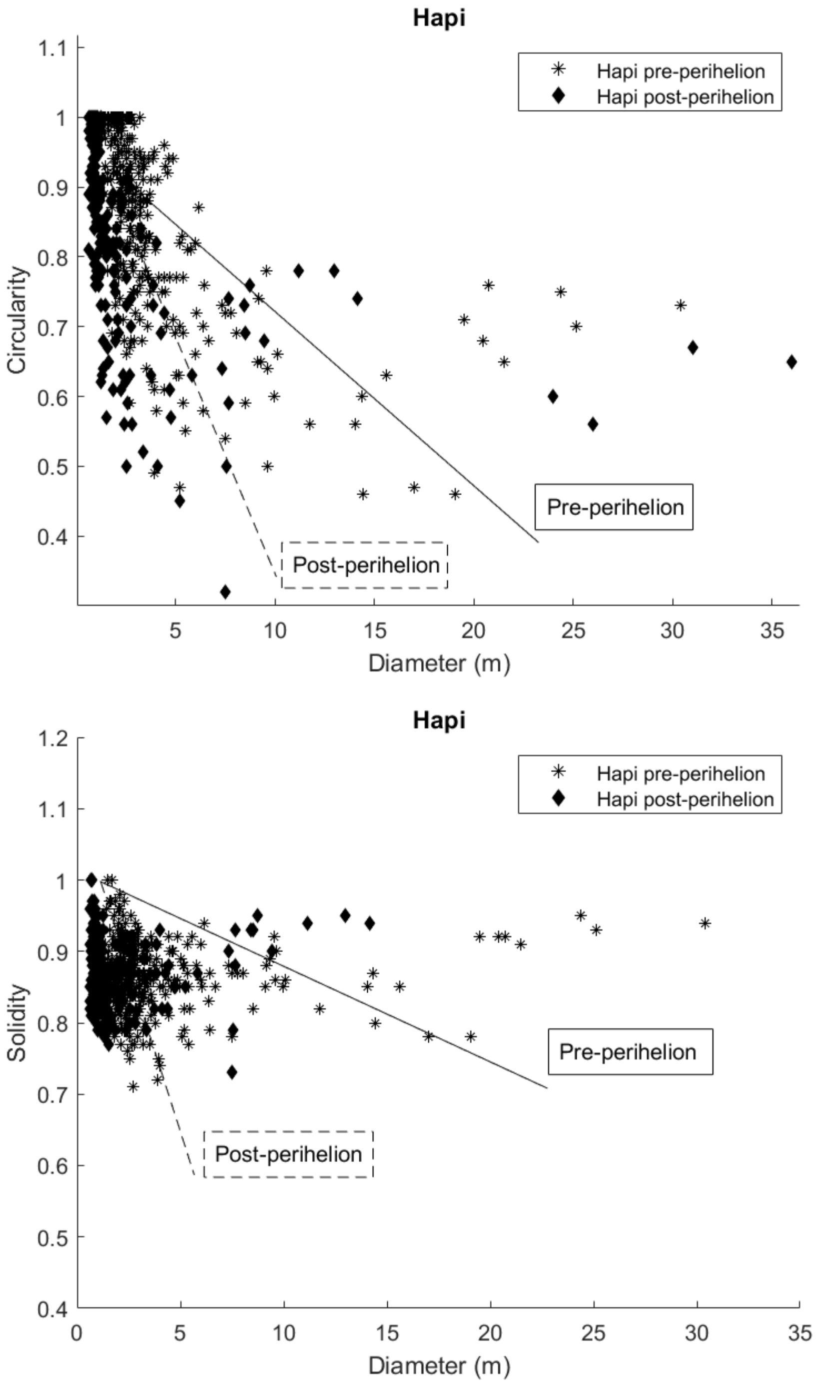

Figure 3.18: Comparison between circularity, solidity, and boulder size. The upper panel refers to the circularity, and the lower panel refers to the solidity. The stars represent the Hapi pre-perihelion case (the solid line is the corresponding trend line), and the diamond represents the Hapi post-perihelion case. The dotted trend line refers to the post-perihelion case.

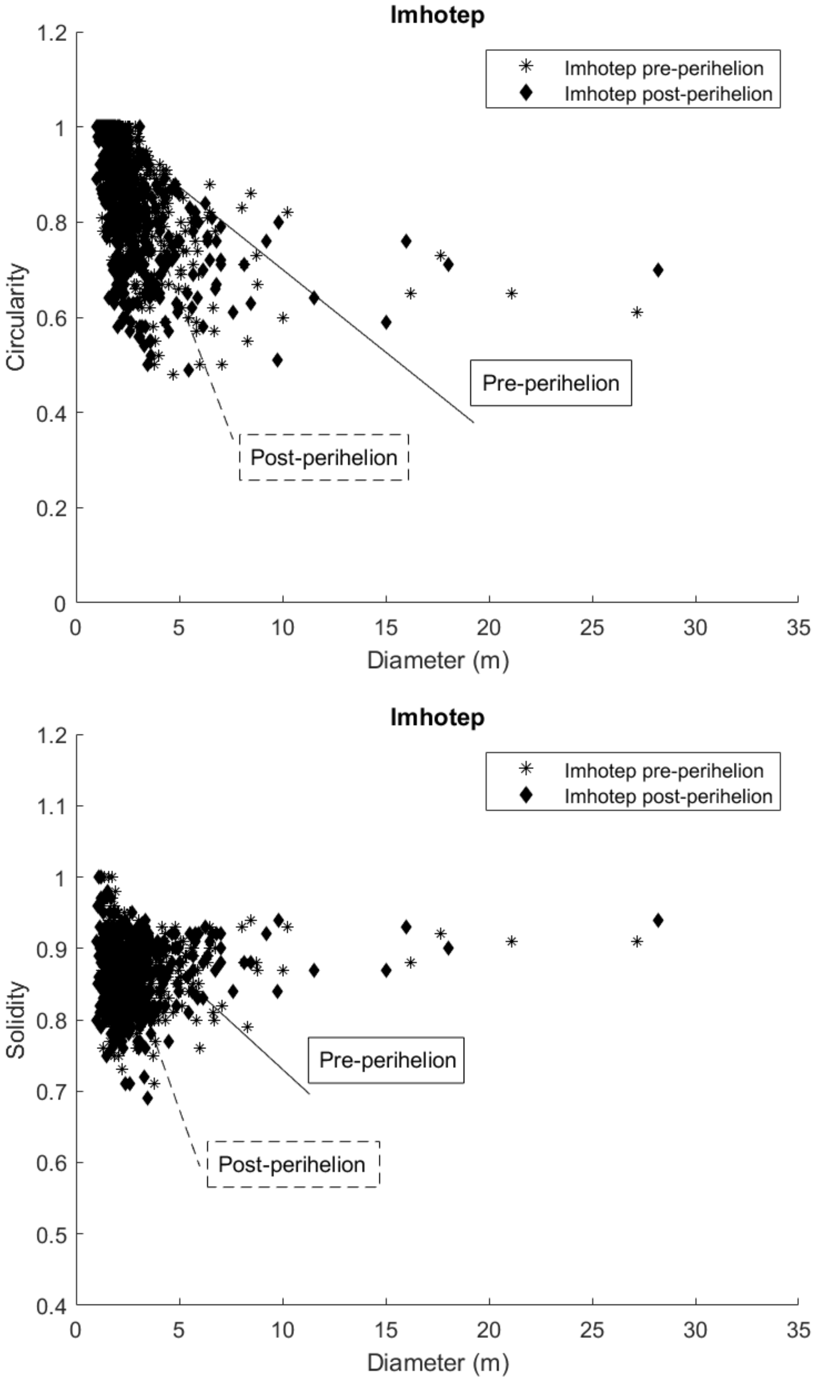

Figure 3.19: Comparison between circularity, solidity, and boulder size. The upper panel refers to the circularity, and the lower panel refers to the solidity. The stars represent the Imhotep pre-perihelion case (the solid line is the corresponding trend line), and the diamond represents the Imhotep post-perihelion case. The dotted trend line refers to the post-perihelion case.

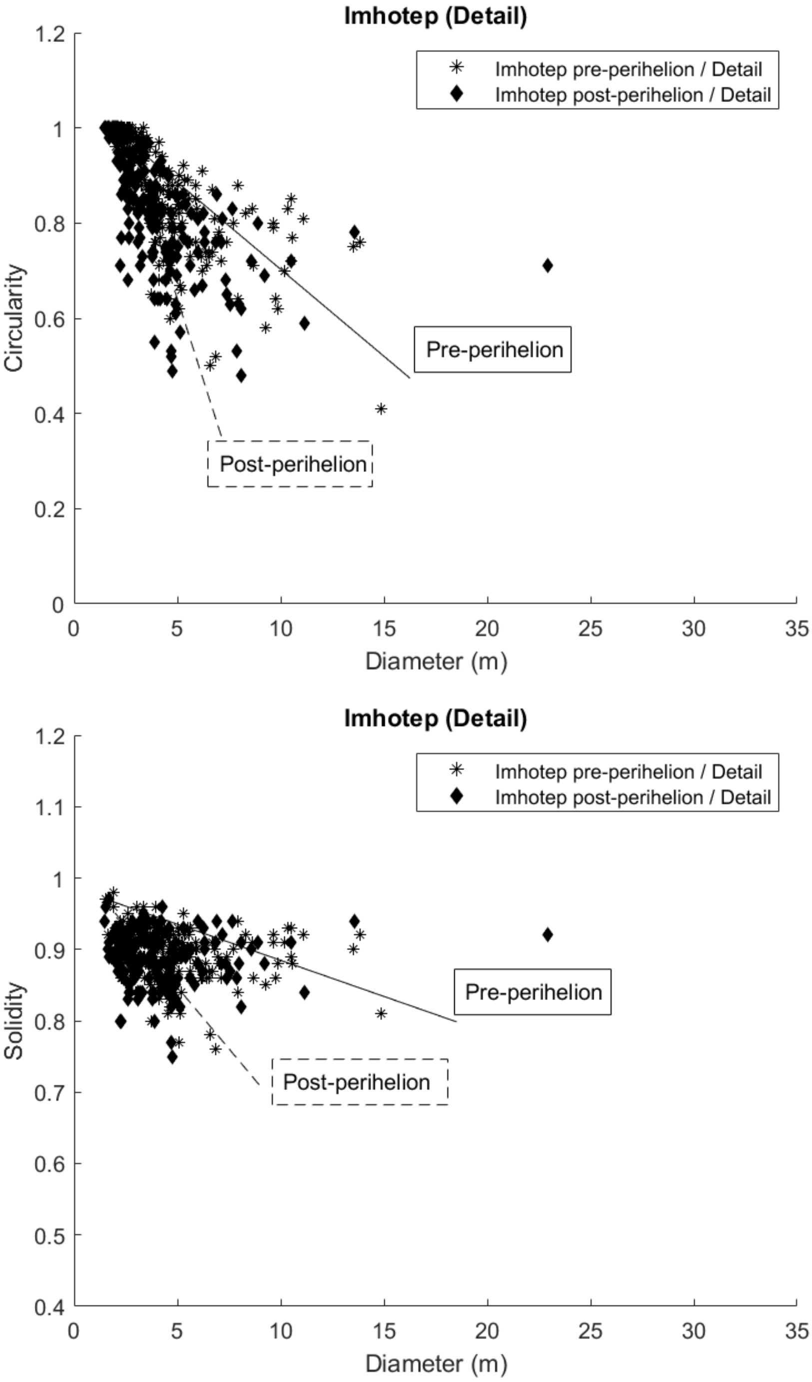

Figure 3.20: Comparison between circularity, solidity, and boulder size. The upper panel refers to the circularity, and the lower panel refers to the solidity. The stars represent the Imhotep (detail) pre-perihelion case (the solid line is the corresponding trend line), and the diamond represents the Imhotep (detail) post-perihelion case. The dotted trend line refers to the post-perihelion case.

Region	Circularity	Stdev	Solidity	Stdev
Hatmehit pre	0.87	0.02	0.88	0.04
Hatmehit post	0.86	0.01	0.88	0.03
Hapi pre	0.92	0.05	0.89	0.05
Hapi post	0.91	0.04	0.89	0.05
Imhotep pre	0.89	0.02	0.87	0.05
Imhotep post	0.89	0.02	0.87	0.05
Imhotep Detail pre	0.86	0.01	0.89	0.04
Imhotep Detail post	0.83	0.01	0.89	0.04
Mean	0.88	0.17	0.88	0.17

Table 3.7: Average shape parameters. Circularity and solidity are given for pre- and post-perihelion passage. Mean values and standard deviations are shown.

ticle sizes in soil. These distributions are often considered as cumulative function, in particular as number of particles larger than a certain diameter, or a mass smaller than a certain diameter. A power-law relations characterize the behaviors of these distributions, and the exponent D can be considered as the fractal dimension, reflecting different domains or setting lower and upper limits to the validity of fractal relations. Analyzing the cumulative size-frequency distributions, we noted a substantial difference between the power index of Imhotep, Hatmehit, and Hapi populations. The first two are in the range of -2.3/-2.7. The Hapi area differs from this behavior, with a value of -1.2/-1.7 pre- and post-perihelion. As suggested by Pajola et al. (2015), these data might indicate different formation processes of the boulders. In particular, collapses and pit formation are characterized by power-law exponents of about -5 to -6.5. Indices between -3.5 to -4.5 are typical for gravitational events caused by sublimation and thermal erosion, while material formed during gravitational events and collapses that has undergone continuous sublimation typically shows power-law indices of -1 to -2 (Pajola et al., 2015). The values of -2.3 to -2.7 could therefore represent a transition between these two scenarios.

Table 3.4 shows that the minimum, maximum, and average values of the boulder diameters change after perihelion passage. The highest resolution of post-perihelion images allows us to outline more boulders and more details, decreasing the minimum and the average value of diameters. The maximum diameter changes because pre- and post-images have different observing conditions, and this is reflected in a diameter variation that is justified by an intrinsic error in the boulder selection method. From this, we conclude that the distribution of boulders does not show significant variations with respect to the perihelion passage, in agreement with what is found in other works (Stern et al., 2007; Pajola et al., 2015). There may be several explanations for this: a first reason might be that the heat flux density received during perihelion passage is not enough to change the examined populations. Second, there could have been changes, but the erosion was uniform and the shape parameters can only distinguish differential erosion. This erosion occurs at irregular or varying rates caused by the differences in the resistance and hardness of surface materials. This uniformity in erosion could therefore reflect the uniformity of cometary material.

We examined the spatial distribution of the boulders with respect to their size. The cumulative fractional area explains how abruptly the area covered by the boulders decreases with increasing diameters. A power law fits well the Imhotep and Hatmehit populations, but not the Hapi one. Moreover in Hapi, that is on the neck of the comet, the analyzed boulders also reveal a spatial distribution different from the other populations.

To verify the fractal behavior of the analyzed populations, we used the box-count approach. This method allows to calculate the fractal dimension displaying a plot in which the scaling line $n \propto r^2$ expected for a space-filling 2D image, and the power-law $N = N_0 r^{D_f}$ are shown. The possible fractal behavior of the data set is indicated by the discrepancy between the two curves. The calculated fractal dimension indicates that all study areas show a possible fractal behavior, except for the bigger boulders of Hapi. In fact, as shown in Fig. 3.13, the discrepancy between the two curve is evident only for boulders of small size. We then hypothesize that the analyzed boulders on the neck of 67P do not follow the fractal fragmentation rules, suggesting the possibility of a different origin of these features. The results obtained so far show that the Hapi area differs from the others in size-frequency distribution, cumulative fractional area, and fractal analysis. One possible explanation could be that these boulders collapsed during gravitational events and their fragmentation in situ is controlled by thermal fatigue. This can be justified by the location of Hapi, which is a connecting region between the two lobes of comet 67P that represents a gravitational potential well. Another scenario takes into account the configuration of the Hapi region. Penasa et al. (2017) showed that the peculiar alignment of boulders in the Hapi region is geometrically consistent with the inner layering of comet 67P (Massironi et al., 2015). The boulders appear to be aligned along a specific layer of the large lobe. The low values of the power index derived for the boulders of Hapi and the differences found in the various parameters analyzed here compared to other populations might reflect this particular relationship with a specific layer of the large lobe. This layer may have undergone fragmentation, which left behind a field of boulders that is aligned with the layering. These boulders would then represent the tops of outcrops, immersed in a deposit of back-fall material that is several tens of meters thick (Keller et al., 2007).

We defined a set of shape parameters to describe the boulder morphology. Solidity and circularity are invariant shape parameters under changes of observing geometries. We noted that boulders have a homogeneous morphology across the different populations. They consist of compact, convex, rounded, and solid boulders without many inlets. Boulders with average dimensions appear not to exhibit an enhanced tabular shape (i.e., low elongation values), which would be expected for a fragmentation that preferentially occurs along planes that are defined by a tight alternation of layers. The current rounded shape might be connected to a pattern of equally spaced planes of weakness and/or to the weathering processes that follow any kind of fragmentation (i.e., sublimation processes). This result also indicates how sublimation and thermal stress act on the surface of the comet. The near-circularity of all boulders points to a limiting case, where uniform erosion shrinks the boulders on all sides. This might also reflect that the processes involved in the fragmentation are not much influenced by preexisting planes of weakness such as layers or fractures (and hence other factors exert larger control on the final shape), or that layering on this scale (as opposed to the global scale of the body) might be not present at all. This case would be consistent with the observations made by Belton et al. (2018), who suggested a layer thickness of about 10 meters, and with the observation that the studied boulders do not exhibit evident layering. Similarly, a tight alternation of layers characterized by a variable attitude to sublimation would have been expected to produce more inlets by favoring differential sublimation (enhancing the sublimation of the more erodible layers), suggesting that this kind of heterogeneity is not present at the boulder scale either, or that it cannot be observed due to other prevailing processes. On the other hand, larger boulders have diameters of 20-30 m, comparable to the layer thickness (or multiples of it) suggested by Belton et al. (2018). In that case, decameter-scale layers would provide decameter-scale boulders with moderate to high values of circularity and solidity (Fig. 3.16). Finally, when we compare the mean values of the shape parameters before and after perihelion, we do not note significant differences among the analyzed regions.

3.5 Conclusions

Size-frequency distribution in soil is one of the most fundamental tools for analyzing soil physical properties. Commonly, they are reported as cumulative distributions, and different functions have been proposed to fit experimental data. In this chapter, we introduced the concept of soil fragmentation, investigating fragmentation models in the past century, and exploring the link between this process and the fractal theory. In this context, we presented a detailed quantitative analysis of isolated boulder populations that are located in three different regions of the cometary nucleus of 67P: Imhotep, Hapi, and Hatmehit. By using OSIRIS-NAC images, we identified 11811 boulders, 4581 of which belong to the Imhotep population, 641 to the Imhotep detail, 5187 to the Hatmehit population, and 1402 to the Hapi region. We proposed techniques for analyzing boulder populations that can complement previous studies, analyzing the size-frequency distribution and the cumulative fractional area of these populations, and connecting these data with the fractal theory. We also outlined the boulder morphology, providing a shape parameter set that does not depend on variations of observing geometries. The analysis of the cumulative fractional area, the link with the fractal theory, and the analysis of the shapes can provide additional information about the population of boulders. As demonstrated by the Hapi case study area, anomalies can be identified, and these differences give the possibility to further investigate the origins of these boulders. The analysis was also performed to understand the role of the perihelion passage of 67P in the fragmentary and erosive processes. We expected some variations in terms of number and shape of fragments after the perihelion passage, which is the point of the comet orbit closest to the Sun and results in the position with the highest insolation. Our results do not show variation of this type, at least within the limit of this image resolution.

Chapter 4

Time Evolution of Dust in the Hapi Region

The comet rendezvous mission Rosetta revealed that the nucleus of comet 67P consists of two lobes (Sierks et al., 2015), connected by a narrow neck (see Fig. 4.1), with a stable spin axis. The nucleus rotates with an obliquity of 52° (Keller et al., 2007). Due to the inclination of the axis of rotation, the comet experiences strong seasons, resulting in significant differences in insolation between the northern and southern hemispheres. This strong dichotomy is reflected in the morphology between the two hemispheres. The OSIRIS observations revealed that the northern regions, such as Ash, Ma′at, Seth, and Hapi (Thomas et al., 2015b; El-Maarry et al., 2015) are fully covered by dust. On the contrary, equatorial regions such as Anubis, Aket, and Bastet, look different. In these regions, dust deposits appeared to have been replaced by consolidated and coarse terrains (Keller et al., 2017). Differences between the two hemispheres are mainly due to differences in insolation. Southern summer coincides with the perihelion passage and this causes the erosion in the southern hemisphere to be much stronger than on the northern regions (Jorda et al., 2016; Keller et al., 2017). The approach to perihelion causes the rise in nucleus temperature, sublimating the ices. Observations of the coma revealed water to be the most abundant volatile (Gulkis et al., 2015). Keller et al. (2017) calculated the erosion due to sublimation of water ice to investigate the link between insolation, erosion, and water content of the nucleus surface. The value was found to be four times stronger on the southern hemisphere, than on the northern one. The strong insolation and the water ice content in the south could erode the surface up to 20 m (Keller et al., 2017) at the perihelion. In Fig. 4.2, the erosion due to water ice sublimation is shown. The northern hemisphere, particularly Hapi, is characterized by a minimal amount of insolation, and therefore a minimal erosion. These

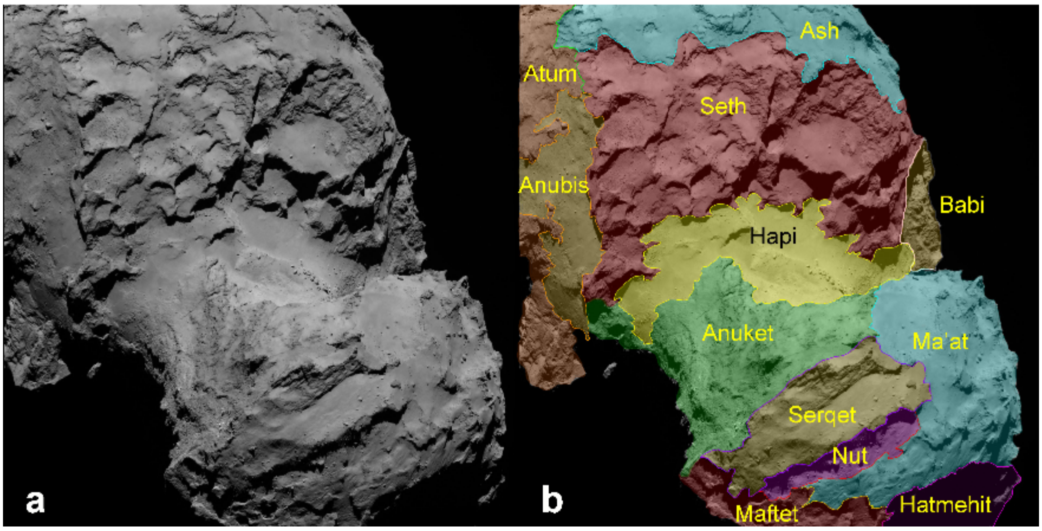

(El-Maarry et al., 2015)

Figure 4.1: (a) NAC image of comet 67P taken on 16 August, 2014, at 10.59.16 UT. (b)Same image with regional boundaries.

evidences confirmed that the dichotomy in appearance between the two hemispheres is linked to the dichotomy in erosion, and that the dust cover in the northern regions can be the result of transport mechanisms of particles from the southern hemisphere during the southern summer (Keller et al., 2015). The erosion of the southern hemisphere, the subsequent transport of material, and then its fallout on the nucleus, are fundamental to investigate the pristine water ice abundance in comet 67P, assuming that 67P's ice content is representative of the average value of all comets.

In this chapter, we describe the mass transfer mechanism from the southern hemisphere to north, linking this process with the activity of the comet and the erosion of the comet's surface. The erosion is linked to the comet's pristine ice content, which represents a long-standing problem of the comet's formation. Comets formed beyond Neptune and water was incorporated in form of ices embedded in the refractory matrix of their nuclei (Blum et al., 2017). The difference in water content between different bodies is essential to shed light on their distinct formation processes, clarifying the different efficiency in trapping water ice from the protoplanetary disc (Lorek et al., 2016). To provide an upper limit of comet's water ice fraction, fixing the pristine 67P ice content, we quantified the seasonal erosion and deposit/accretion in the Hapi region. We developed a tool which allows to monitor the time

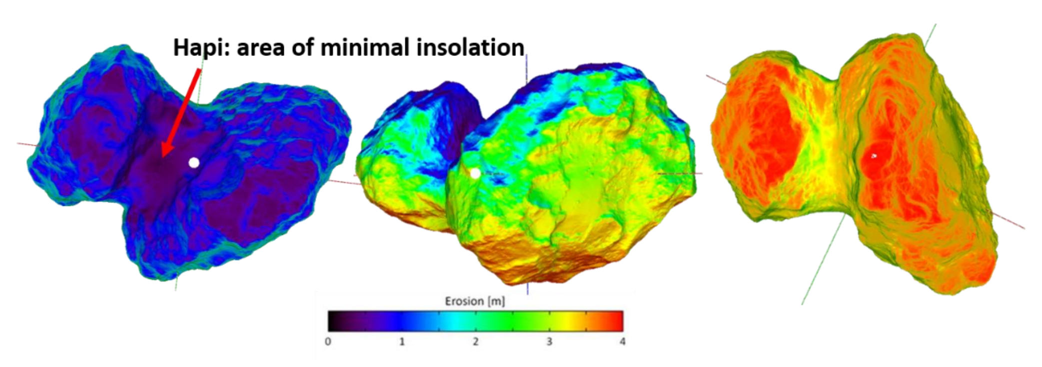

Figure 4.2: Total (integrated over one orbit) water erosion. Left: northern areas and neck, middle: equatorial view, right: southern view. (Keller et al., 2015).

evolution of boulders height, defined as the difference between the top of the boulders and the surrounding pebble deposit surfaces. This technique has led to measure the seasonal evolution of the deposit erosion/accretion of the Hapi region with a vertical accuracy of 0.2 m, fixing the pristine 67P ice content of the meters-thick layers eroded every perihelion from the southern hemisphere.

4.1 The Refractory-to-Ice mass ratio

Water content and delivery to the terrestrial planets is still today subject of debate. Water is present in different bodies of the Solar System, even in the outer asteroid belt and beyond in form of ices. In Fig. 4.3, the association between water contents of materials and heliocentric distance is shown. Primitive meteorites such as CI chondrites are believed to come from C-types asteroids that dominated the outer part of the asteroid belt (Burbine et al., 2002), and can have $\sim$ 5-20% water by mass (OBrien et al., 2018). Growth processes of carbonaceous CI-chondrites, characterized by a chemical composition mostly resembling the solar photosphere, allow water to be trapped in their silicates at a molecular scale (Garenne et al., 2014). Ordinary chondrites are linked to S-type asteroids, which are present in the inner asteroid belts, and contain a different amount of water. Water in comets was incorporated in form of ices embedded in the refractory matrix of their nuclei (Blum et al., 2017). The radial distribution of water and ices is recorded in the refractory-to-ice mass ratio in comets (Fulle et al., 2018b). This ratio is a fundamental parameter which constrains the origin of comets

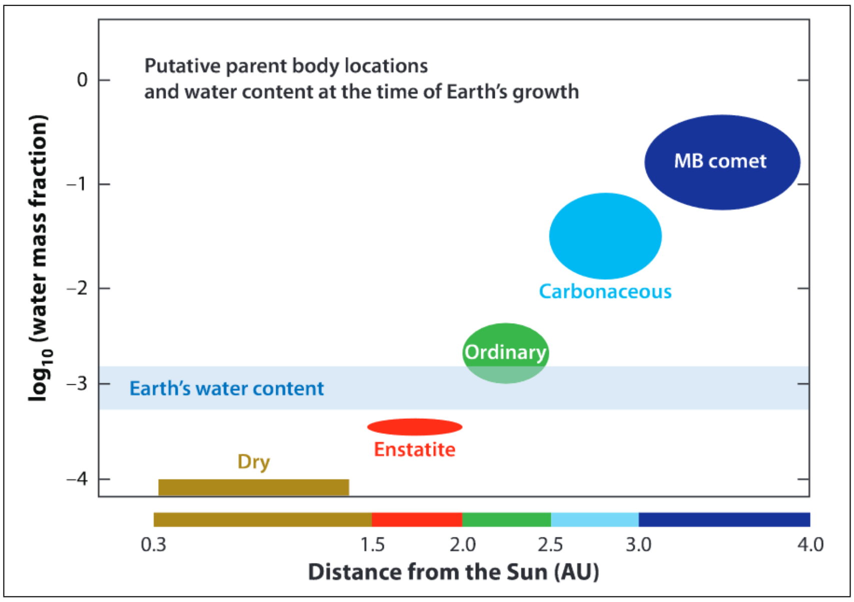

Figure 4.3: Water contents of material estimated to have formed at different heliocentric distances. The range of Earth's possible water content is shown for comparison (Morbidelli et al., 2012).

and KBO's. Quantifying the difference in water content between comets and other bodies allows to distinguish between different formation processes, providing knowledge on the origin of the Solar System.

4.1.1 Mass Transfer on 67P

Differences in insolation between the northern and southern hemispheres cause differences in erosion. The eroded southern surface is subjected to a strong insolation (Keller et al., 2015), and this leads to strong water sublimation, which contributes to release dust particles of different sizes. Small dust particles are in the size range from 3×10^{-3} to 45 mm (Fulle et al., 2016). Larger particles have also been detected by OSIRIS. These particles, named *chunks*, are defined as pieces of the nucleus of average mass of 1 kg, in the 10 to 20 cm range (Fulle et al., 2018b). To constrain the refratory-to ice mass ratio, Fulle et al. (2019) calculated the chunk volume ejected by 67P from 24 July, 2015, to 15 September, 2015. The lost volume is about 4×10^7 m^3, corresponding to an eroded southern surface of about 10 km^2 (Keller et al., 2015; Blum et al., 2017). This corresponds to an average erosion thickness of about 4 m (Fulle et al., 2018b). Assuming that the southern erosion occurrs because of the ejection of chunks, Keller et al. (2015) estimated the southern erosion from a nucleus surface of 65 m^2 due to a constant insolation, finding a water loss rate of about 20 g s^{-1}, which correspond to a negligible mass fraction of the corresponding chunk loss rate ($Q^{\cdot}v = 8.3 \pm 2.1$ m^3 s^{-1} (Fulle et al., 2016)). This result suggests that the chunk ejection from the nucleus surface is dominated by perihelion erosion of the southern hemisphere, but behaves independently of water ejection. In this context, chunks at their ejection reflect the refractory-to-ice mass ratio of the 67P nucleus, and the comparison between the chunk loss rate and gas loss rate is no longer a useful strategy to constrain the refractory-to-ice mass ratio of comet 67P.

As mentioned before, the dichotomy in appearance between the two hemispheres is linked to the dichotomy in erosion. The dust cover in the northern regions is the result of transport mechanisms of particles from the southern hemisphere during the southern summer (Keller et al., 2015). Furthermore, OSIRIS observation of the nucleus reveal a surface characterized by a varied surface granularity. Pebbles of ≈ 25 cm in size have been observed in Sais region (Pajola et al., 2017), suggesting a deposit built up by chunks, and confirming the chunk mass distribution in the 67P coma (Fulle et al., 2016; Ott et al., 2017). This distribution can be explained with the dust fallout mechanism, which causes chunks ejected during perihelion falling back over the whole nucleus. Finally, as the outbound equinox approaches, the southern erosion decreases, and the outgassing in the northern hemisphere self-cleans the fallout, removing the dust and leaving chunks, because the nuclues outgassing is too low to lift these objects.

The peculiar shape of comet 67P and its inclination are not the only factors influencing the distribution of material deposit. The distribution is also strongly influenced by the local activity of the comet. When a comet approaches the inner Solar System, the heating of the nucleus can cause the sublimation of ices below the surface. The sublimation generates gases which break out of weak spots on the surface of the nucleus, causing a stream of dust and gas. The activity can be described by two different events, which differ by their duration and strength. First, regular flows of material have been observed coming from comet 67P. These events regularly recur from one comet rotation to the next. Second, outburst events are characterized by a sudden release of dust, and look brighter than the previous jet-like features. Outbursts are transient events, and three types of jets have been identified:

- *Type A*: collimated and very bright jet that extend far from the nucleus;
- *Type B*: broad plume with a wise base;
- *Type C*: hybrid event between types A and B.

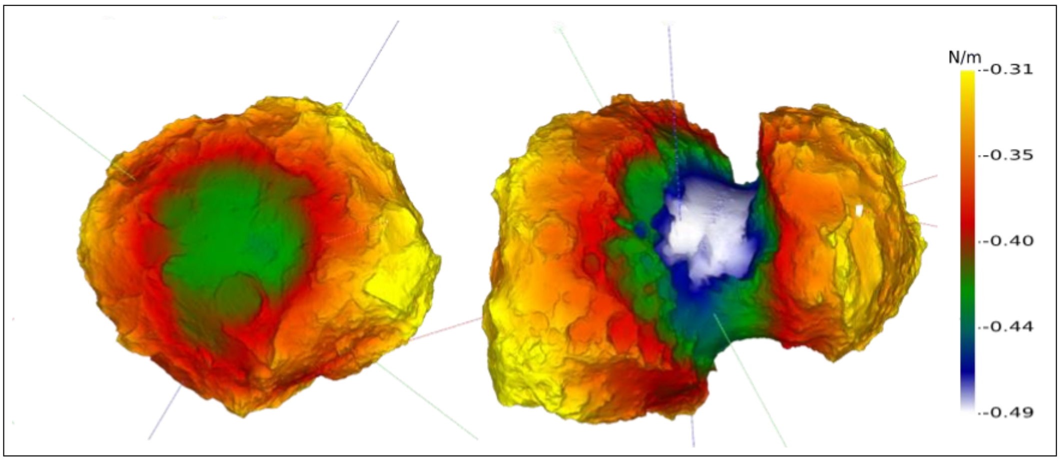

Figure 4.4: Gravitational potential of comet 67P. The central green region on the left projection is Imhotep; the white region on the right is Hapi (Keller et al., 2017).

The strong seasonal variation causes the ejection of chunks from the south during the southern summer around perihelion, and deposition during the northern summer as a result of the strong activity of the comet (Keller et al., 2017). The activity is therefore linked to the appearance and physical properties of the surface. An increasing activity is the indication of an increasing insolation which modifies the properties of the comet's surface.

4.1.2 The Hapi Region

The Hapi region is located in the northern hemisphere (Thomas et al., 2015b), between the two lobes of comet 67P. It has been classified as a deposit of debris (Thomas et al., 2015b), and is characterized by a distribution of boulders and/or outcrops (Cambianica et al., 2019) scattered all over the debris plain. Hapi is also dominated by smooth terrains (El-Maarry et al., 2015) and dune fields. Due to the presence of boulders and outcrops of tens of meters in size, El-Maarry et al. (2015) suggested a dust deposit thickness of several meters. In Fig. 4.4, the gravitational potential of comet 67P is shown. The neck region corresponds to the gravitational minimum of the nucleus (Keller et al., 2017), and is therefore considered as the preferred location for the accumulation of the back falling material (Keller et al., 2017). A secondary local minimum gravitational potential is located in the small lobe, in the center of the Imhotep region. This area lies near the equator, and is also fully covered by dust.

δ	Crust thickness (cm)	Δ	Q_g (kg m^{-2} s^{-1})
2.5	0	2.5	10^{-5}
5.0	1	5.4	10^{-5}
10	3	13	10^{-5}
20	5	32	10^{-5}

Table 4.1: Refractory-to-ice mass ratio in the nucleus (δ) and in the chunks (Δ). The increase of these values are due to the crust dehydration after 1.8 days of perihelion insolation with an average erosion of 1 cm (Fulle et al., 2018b). In the last column, the water production rate is reported.

Chunks ejected at perihelion fall back over the whole nucleus, including Hapi. The deposit of pebbles in this region can be explained in terms of self-cleaning (Pajola et al., 2017), as well as for Sais and Agilkia regions. As the outbound equinox approaches, the outgassing where fallout occurred increases. This event self-cleans the fallout, removing dust and leaving chunks on the surface. Hapi's outgassing is significant from 2.5 to 4 au outbound (Fulle et al., 2018b), and negligible elsewhere. This implies that Hapi ejects sub-cm dust only (Rotundi et al., 2015), acting as a chunk deposit with a thickness of meters. This can be explained as follows. Chunks ejected at perihelion have a refractory-to-ice mass ratio larger than inside the nucleus, having an upper exposed dehydrated crust, whose thickness increases as the refractory-to-ice mass ratio increases (Fulle et al., 2018b). Fresh ice on the surface of Hapi is exposed to Sunlight by water ice migration to the surface (De Sanctis et al., 2015) and by the removal of chunks dehydrated crust. This causes outgassing coming from the interior of the chunks, preventing any outgassing from below the surface. Because the strength of the outgassing depends on the ice mass fraction in chunks, Fulle et al. (2019) calculated the variation of refractory-to-ice mass ratio in the chunks by varying the dehydrated crust thickness (see Table 4.1).

Keller et al. (2017) calculated the water production of the nucleus along its orbit. They found that the production rates of the northern regions follow the insolation trend, controlled by the peculiar shape of the nucleus and the inclination of the spin axis. Hapi represents the conjunction point between the two lobes. This cavity reached insolation for short intervals of a cometary day because of the shading by the lobes. This should mean that this region cannot be active as other regions located in the south. However, Hapi appears to be the most active area during northern summer. The solution of this enigma lies in the composition of the surface. Spectra reveal that Hapi

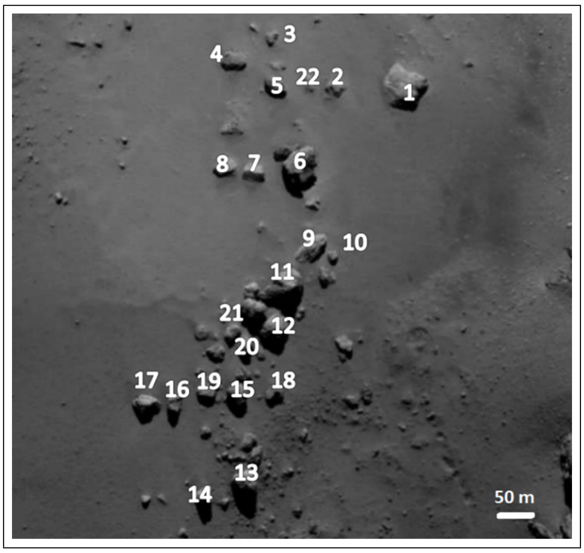

NAC_2014-08-21T16.42.56.549Z_ID30_1397549300_F22

Figure 4.5: Zoom of the 21 August, 2014 image. The figure reports the corresponding ID for each boulder.

contains more water ice than the plains covered with the back fall material (Keller et al., 2017). Because of the morphology of this region, the absorbed energy is not sufficient to sublimate ices producing a strong gas flux, but this big cavity provides up to 50% additional energy input by self-heating from Hator and Seth regions. This amount of energy is then enough to activate the neck. The enhancement is due to a thinner dessicated dust layer formed during the inactive aphelion passage (Keller et al., 2017). This dust cover is composed of dust which remains on the top of the dust-to-ice ratio matrix material. This fact explains the variation of the spectral slope of the Hapi region which becomes bluer during the approach of the comet towards the Sun and turning red after southern equinox (Fornasier et al., 2016). The dessicated dust cover is reduced during approach and accumulated after perihelion, thereby justifying the reddening of the spectra. In this context, the seasons of Hapi allow to link (Fulle et al., 2018b) its processed ice abundance to the pristine ice content of the meters-thick layers eroded every perihelion from the southern nucleus hemisphere.

To provide an upper limit for Hapi's water ice fraction, fixing the pristine 67P ice content, we measured the seasonal evolution of Hapi's deposit erosion/accretion with a vertical accuracy of 0.2 m. The adopted method is described in the following section.

4.2 Method

4.2.1 Data Selection

For the analysis of dust erosion and deposit on the Hapi region we used 19 OSIRIS NAC images (see Table A.1 in Appendix A for image IDs) and the photogrammetric SHAP8 V.2.1 comet shape model, which represents an advanced model based on a data set of 20679 OSIRIS-NAC images and 6072 OSIRIS-WAC images acquired between 11 July, 2014, and 30 September, 2016 (https://www.cosmos.esa.int/web/psa/rosetta). The first set of 16 NAC images was acquired from 21 August, 2014, to 10 December, 2014, that is before the comet inbound equinox. The spatial scale ranges from 1.26 m/pixel to 0.37 m/pixel. The second set of 3 NAC images was acquired from 19 June, 2016, to 30 September, 2016 (spatial scale of 0.56 m/pixel, 0.54 m/pixel, and 0.26 m/pixel, respectively) after the outbound equinox. To fix the value of the 67P's pristine ice content, we monitored the time evolution of boulders heigth from 21 August, 2014 up to the end of the mission. For doing this, we developed a MATLAB (MATLAB, 2010) tool, which is based on the measurement of the shadow length projected by the boulder itself. Here, the height is defined as the difference between the top of the boulders and the surrounding pebble deposit surfaces. This technique requires high resolution images (at least 1.30 m/pixel). High resolution NAC images provided global views of the Hapi region, allowing us to analyze as many boulders as possible. According to the illumination and visibility conditions, we measured the height of 22 boulders. Boulders location is shown in Fig. 4.5. The figure reports the corresponding ID for each boulder (see Table A.2 in Appendix A for the ID of the boulders and their latitudes and longitudes).

4.2.2 Surface Plane Definition and Image Alignment

The procedure to measure the height H of the boulders is based on the interaction between the OSIRIS NAC image and the 3D shape model of the comet. This is allowed by the projection of the image on the 3D model. To obtain the correct projection, we defined a set of uniquely identified tie points both on the shape model and on the images. From the correspondence between these points, we derived the proper homography transformation for each projective system. As a result, we could associate to each pixel of the images the corresponding 3D point on the comet nucleus surface photogrammetric model. In Fig. 4.6, an example of the bundle adjustment procedure and a possible misalignment between the two is shown. Once this misalignment is corrected and the proper boulder is identified, having the knowledge

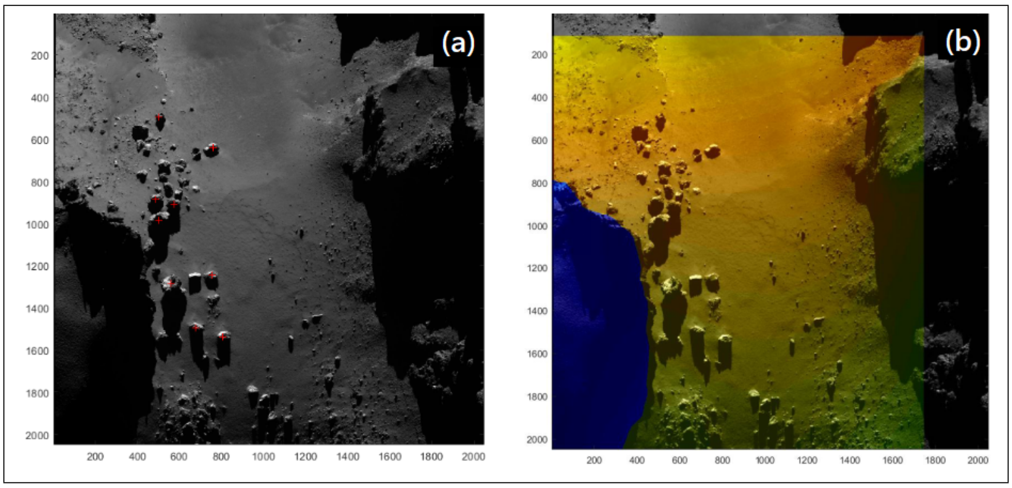

Figure 4.6: (a) 10 December, 2014 OSIRIS NAC image. (b) Results of the bundle adjustment procedure. The misalignment between the shape model and the image is evident. Axis report the number of pixels along the two dimensions.

on the photogrammetric model of the 3D surface imaged by OSIRIS, it is possible to draw on it the contour of the boulder. Considering a grid of 3D points around this contour and by suitable interpolation, it is possible to define the surface plane Σ around the boulder (see Fig. 4.7). This is the surface in which the boulder shadow is projected. The definition of an average surface plane is fundamental to avoid the local granularity of the mesh and to smooth possible surface irregularities, since the topography and surface texture of Hapi are non-homogeneous. Other parameters to be defined are the incidence angle i of the solar direction with respect to the normal to the plane Σ, and the length L of the boulder shadow. These three elements completely define the adopted geometry for determining the boulder heigth.

4.2.3 Boulder Profile Reconstruction and Height Calculation

The definition of the incidence angle allows to know the direction of the illumination vector. This vector uniquely identifies the position of the peak of the shadow on the average surface, and therefore on the 3D model (the peak of the shadow is the point Q in Fig. 4.7). It is assumed that the peak is the point of the shadow contour with the longest extension along the illumination direction. Following this, it is necessary to define a plane Π perpendicular to Σ which contains the direction of the illumination direction, and passes

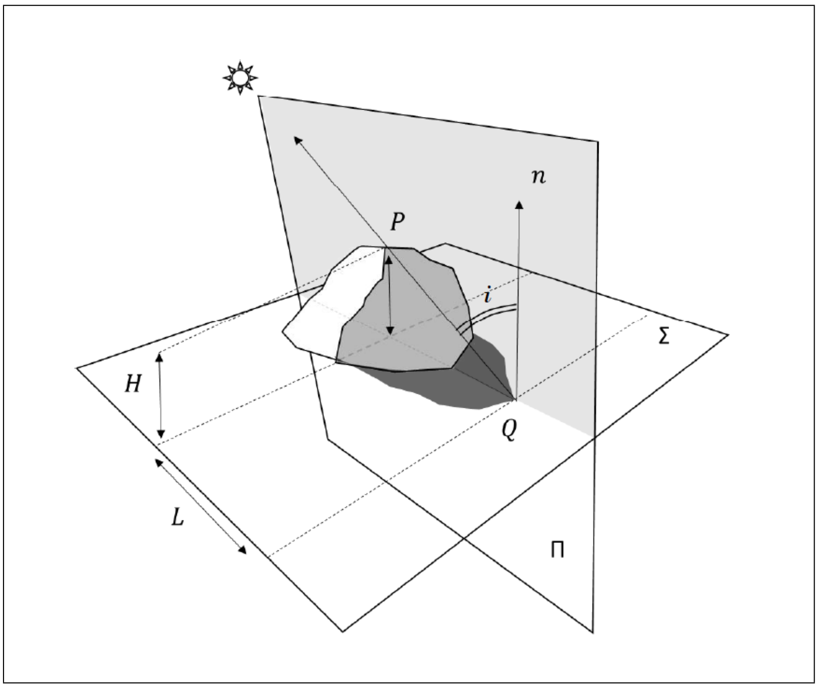

Figure 4.7: Schematic representation of the adopted geometry and of the parameters used for determining the boulder height.

through the point Q. This plane cuts the boulder along the direction of the solar illumination and passes through its highest point P. The bi-dimensional boulder profile obtained by sectioning the comet shape model with the plane Π finally allows us to determine the position of the peak P, being the highest boulder point tangent to the illumination direction (see Fig. 4.7). Then, the length L of the shadow on the Σ plane can be defined as the distance between the Q point and the projection of P on Σ. Finally, the boulder height H can be calculated as follows:

$$H = L \cdot tan\left(\frac{\pi}{2} - i\right) \tag{4.1}$$

In Fig. 4.8 an example of the height measurement is shown.

4.2.4 Gravitational Slopes

To validate our analysis, it is necessary to confirm that our measurement has not been performed on a deposit of thickness altered by local gravitational instabilities processes, i.e. landslides and granular flows, or on a local point of fallout accumulation on the comet surface. For this reason, we analyzed the surface gravitational slope, i.e. the angle between the local surface normal

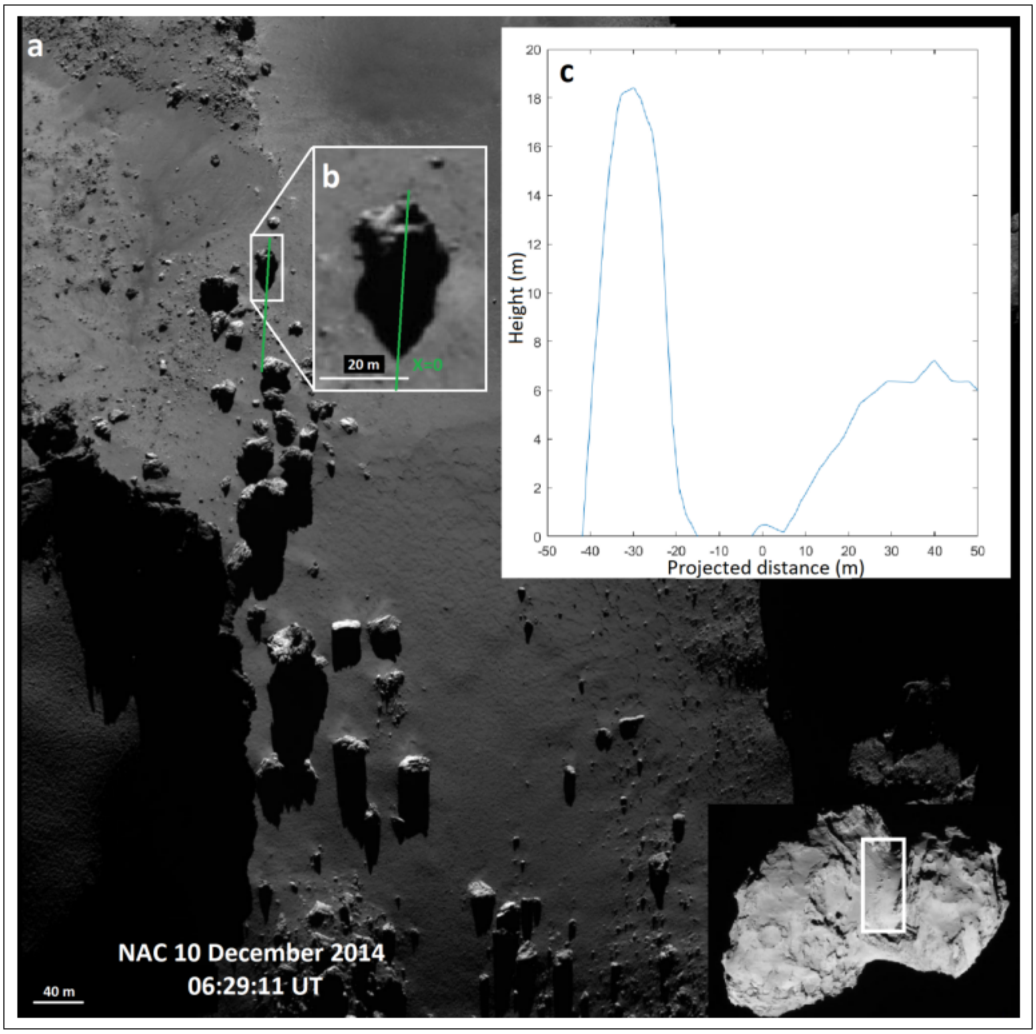

Figure 4.8: (a) NAC view of the Hapi region (0.37 m/pixel); this image was acquired in 2014. (b) Close-up of a boulder and of its shadow. The green line represents the projection of the Sun illumination direction. (c) Boulder section (note the different scales on the plot axes deforming the boulder shape). The y-axis is oriented as the normal to the average plane around the peak of the shadow. The x-axis is obtained by projecting the green line in panel b on this average plane; the x-axis origin coincides with the peak of the shadow. Note that by comparing the b and c panels, the shadow lengths appear different. The reason is that measuring the length of the shadow directly on the image causes underestimates due to the projection effects.

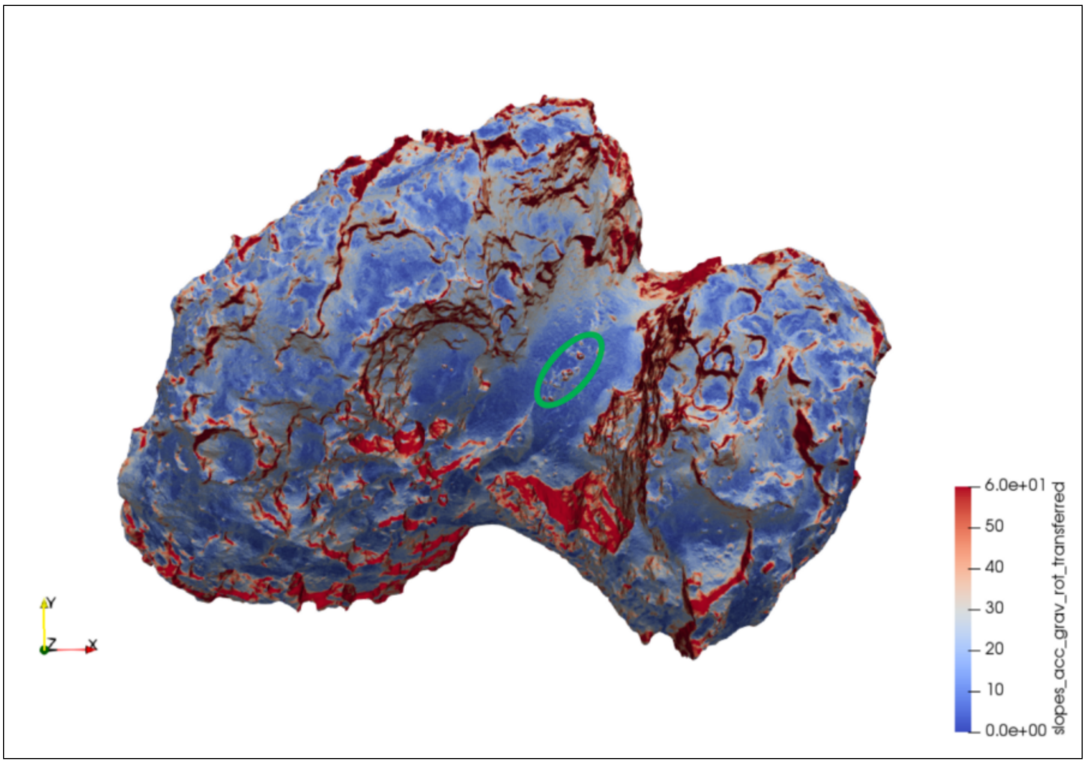

Figure 4.9: Gravitational slopes of the 67P nucleus surface. The values are restricted to the 0°-60° ranges to emphasize the slopes below the repose angle of loose materials (Groussin et al., 2015). The green ellipse defines the surface of 0.2 km^2 encircling all the boulders considered in this work.

and the vector opposite to the estimated acceleration field (Penasa et al., 2017) (see Fig. 4.9, the centrifugal force is included). The whole Hapi region has gravitational slopes ranging between 0° and 20°, below the angle of repose of loose granular materials on 67P (Groussin et al., 2015) of (45 ± 5)° . This is consistent with the assumption that Hapi's deposits are the result of a homogeneous deposition driven by fallout.

4.2.5 Method Validation

To validate the used method, we performed a comparison test. El-Maarry et al. (2017) measured the height of a boulder located in the Imhotep region (see Fig. 4.10 for the location of the region and the considered boulder) finding a value of 3.9 +0.1/ -0.2 m high. We applied our method to the same boulder, and we found 4.08 ± 0.35 m, , that is a value perfectly consistent with the determination of El-Maarry et al. (2017). Being the two methods

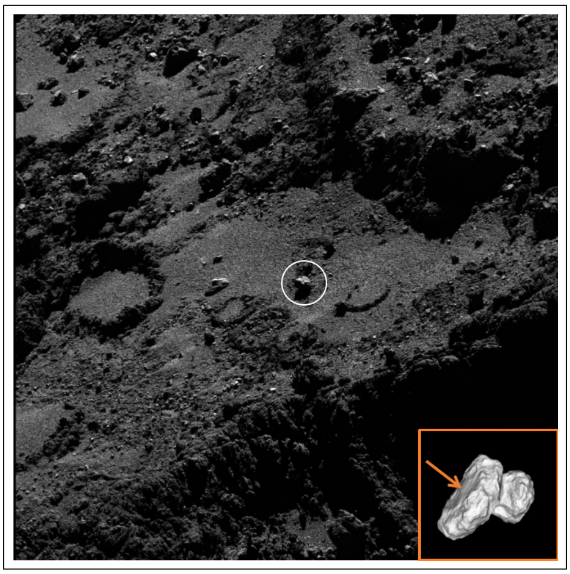

NAC_2016-05-25T15.32.54.769Z_1397549100_F22

Figure 4.10: OSIRIS-NAC image taken on 25 December, 2016. The white circle indicates the analyzed boulder. The bottom right panel shows the location of the Imhotep region on the comet nucleus.

completely independent, this check confirmed the reliability of our method.

4.3 Results

4.3.1 Data Analysis

A summary of the boulder height measurements is reported in Table A.3 in Appendix A. We provide the corresponding acquisition time UTC, the calculated incidence (i) and emission (e) angles, the measured length of the shadow (L), and the height (H) of boulders with the associated average error bar (δH). As shown in Eq. 4.1, the height calculation does not depend on the emission angle, defined as the angle of camera boresight relative to the surface normal. However, we report both the emission and incidence values to show the statistical variability of the images used. To mediate the error bars, we used OSIRIS high resolution images with the best visibility conditions to compare as much heights as possible. We measured 22 boulders, but some measurements have not been included because of their large uncertainty due to the adverse illumination or visibility conditions. The reported error bars have been estimated propagating the individual errors associated to the

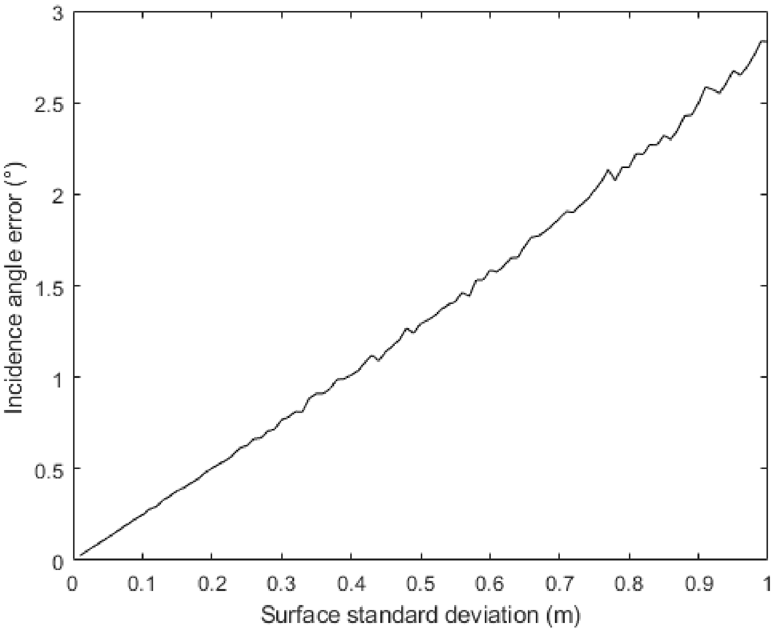

Figure 4.11: Incidence angle error as a function of the surface standard deviation.

selection of the pixel identified as the shadow peak, and the calculation of the incidence angle. The accuracy of the manual selection of the pixel depends on the ability of the operator in selecting the proper pixel. The accuracy of the incidence angle strongly depends on the accuracy of the normal to the Σ plane. This is intrinsically associated to the standard deviation of the distance of the surface points around the boulder from the Σ plane. Figure 4.11 shows the Montecarlo analysis of the impact of the surface granularity with respect to the definition of the surface normal. Being the incidence angle related to the definition of the above mentioned normal, the derived standard deviations for the measured surfaces range between 0.02 and 0.1 m. As seen in Fig. 4.11, in this range the maximum error on the incidence angle value is lower than 0.5°.

After measuring the height of each boulder, we calculated the corresponding maximum and minimum values considering the associated errors (see Table A.3). These values have been obtained as follows:

$$H_{min/max} = [L \mp \delta p(POG \mp \delta l)]\, tan\Big(\frac{\pi}{2} - (i \pm \delta i)\Big) \tag{4.2}$$

where L is the calculated length of the shadow, δp is the error due to the manual selection of the peak of the shadow, the POG is the pixel on ground

(target-spacecraft distance × pixel size / focal length), δl is an error related to the uncertainty of the Digital Terrain Model ($\delta l = \delta h tan(e)$, where δh is the average uncertainty of the location of the DTM with respect to the zero level of the image and e is the emission angle), i is the incidence angle, and the error on the incidence angle, δi, is estimated to be equal to 0.5° (see Fig. 4.11).
To better analyze the data and provide the calculated difference Δ's between the height measurement of a generic image and the height measured on 21 August, the images have been divided as follows: *Subset 1*: 21 - 22 August, 2014, *Subset 2*: 28 August, 2014 - 1 September, 2014, *Subset 3*: 10 - 22 September, 2014, *Subset 4*: 10 December, 2014, *Subset 5*: 19 June, 2016, and *Subset 6*: 30 September, 2016. Having used 19 images, per each subset there are more than one images for which the boulder heights can be measured. Therefore, we have calculated the weighted average height of each boulder $< H >$. The associated error $\delta(< H >)$ is calculated as follows:

$$\delta(< H >) = \frac{1}{\sqrt{\Sigma(1/\delta H)^2}} \tag{4.3}$$

where δH is the largest absolute value difference between the measured height and $H_{Min/Max}$. The reported Δ values are the differences between the $< H >$'s of two subsets, $\Delta =< H_1 > - < H_2 >$. The associated error is finally calculated as:

$$\delta\Delta = \sqrt{\delta(< H_1 >)^2 + \delta(< H_2 >)^2} \tag{4.4}$$

In Table A.4 and A.5, the time evolution of the weighted average height of each boulder and the time evolution of the boulder height difference Δ are shown.

4.4 Discussion

We present observations by the Rosetta mission of comet 67P addressing its pristine ice content. As discussed before, the refractory-to-ice mass ratio represents a long standing problem in cometary formation, and the value we have found solves this part assuming that 67P's ice content is representative of the average value of all comets. Figure 4.12 shows the time evolution of the boulder heights during the observations. Here the difference Δ between the height measurement of a generic image and the height measured on 21 August, 2014 is shown as a function of time. We found a systematic increase of Δ of about 2 m during all of 2014, followed by a decrease of similar amount

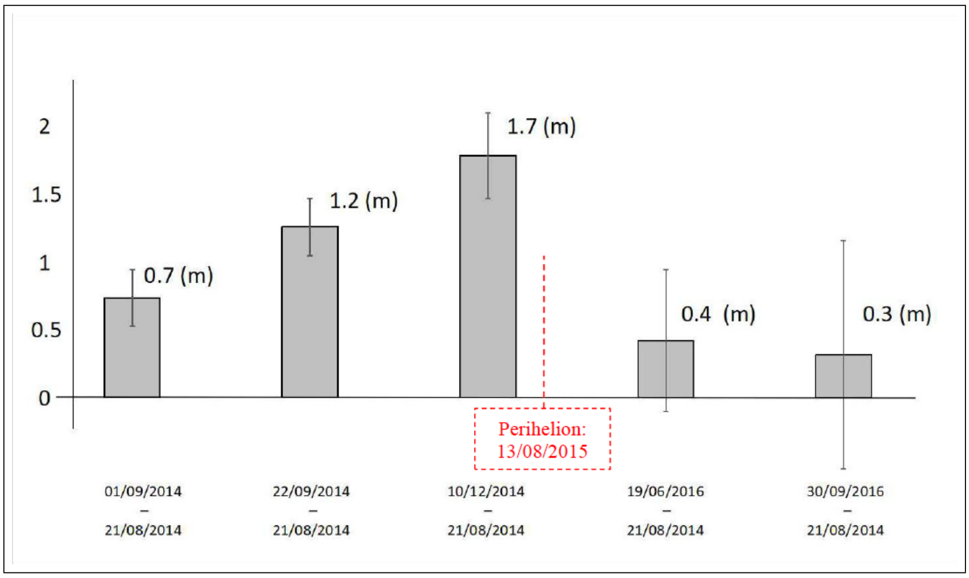

Figure 4.12: Time evolution of the boulder height differences Δ (as defined in text). Each time step contains information related to 22 boulders and the values correspond to the weighted average. The erosion during inbound orbit until December, 2014 nearly balances the fallout from the southern hemisphere during perihelion cometary activity. The dotted red line indicates the perihelion.

between the equinoxes and by a plateau up to the end of the observations. The assumption here is that any height variation is not due to boulder intrinsic changes but to erosion or accretion of the surrounding pebbles and dust deposit. Furthermore, we assumed that due to the dominant cross section of the fallout chunks (≈ 500 cm^2 (Fulle et al., 2018b)), only a minimal fraction of the fallout sticks on the boulder's top. Following the method developed by Cambianica et al. (2019), we analyzed the location and the morphology of these boulders/outcrops, and no variation in morphology or position of the boulders was seen during the mission.

The erosion of the southern hemisphere, the subsequent transport of material, and then its fallout on the nucleus (Fulle et al., 2018b; Keller et al., 2017) are responsible for the time evolution of the boulder height, which is linked to the likely source of the deposit surrounding them. This mainly happens at the perihelion phase (Fulle et al., 2018b; Keller et al., 2017), as evidenced by the similarity between the size distributions of large particles suspended in the coma (Fulle et al., 2016; Ott et al., 2017), and of the cobbles in Sais and Agilkia (Pajola et al., 2017). The measured decrease of the boulder heights at the perihelion phase from 2014 to 2016, $\delta\Delta_{2014-2016} =$

-1.4 ± 0.4 m has thus to be interpreted as a direct measurement of the fallout thickness. This value matches the predicted (Fulle et al., 2018b) fallout thickness of 1.8 ± 0.7 m, making consistent the perihelion erosion with the total nucleus lost mass per orbit (Pätzold et al., 2018). The height difference between boulders and debris field steadily increases during the inbound orbit, indicating an ongoing erosion of Hapi's deposits before the comet reached its spring equinox. As shown in Fig. 4.12, between June and September, 2016, Δ variations are lower than their error bars, consistent with negligible fallout and erosion after the outbound equinox. This is consistent with the suggested process mainly driving the fallout (Fulle et al., 2018b; Bertini et al., 2018), i.e. the expelled chunks in bound orbits are slowed by the friction with the coma gas and finally collapse onto the nucleus. After the outbound equinox, the coma of 67P is too tenuous to further affect the chunk motion. The negligible Hapi's erosion from June to September, 2016 also suggests that Hapi maintains all its ice during the outbound orbit, up to the next inbound activity (Fulle et al., 2018b; Keller et al., 2017). Any possible ice regression without dust ejection would soon build-up an insulating crust of thickness of a few cm at most (sufficient to dump any further ice sublimation), much thinner than the chunk size. Knowing the amount of eroded material (Δ), we calulated the average erosion rates. This value can be calculated as follows:

$$Rate_{Erosion} = \frac{\Delta \times A}{\delta t} \tag{4.5}$$

where A is the area of the considered elliptical surface encircling all boulders. The average erosion rates decrease from 0.15 ± 0.07 m^3/s in August, 2014, to 0.06 ± 0.03 m^3/s in September, 2014, and to 0.012 ± 0.010 m^3/s in October-December, 2014. Since the adopted surface of 0.2 km^2 is only 10% of Hapi's one, and there is no reason that Hapi's deposits occurs only around the boulders, the provided erosion rates are probably lower limits only. Such a trend is consistent with a self-cleaning (Fulle et al., 2018b; Pajola et al., 2017) of the deposits due to the outgassing of the chunks composing them. This self-cleaning erodes the ice-rich fallout from the previous perihelion, and exposes the underlying strata that may be either less rich in ice, or consolidated terrain of material bonded by tensile strengths much stronger than in the chunks. This justifies the fact that Hapi's erosion rate decreases as the comet approaches the Sun. At the same time, the activity of the southern hemisphere acts increasing the total gas and dust loss rates as the comet approaches the Sun (Fougere et al., 2016). By comparing the Hapi's erosion rate and the dust volume loss rate measured in the coma, it is possible to directly estimate the fallout from the activity of the neck region. The measured erosion rate in August, 2014 is 0.15 ± 0.07 m^3/s, a factor 25 larger than the volume loss rate measured in the coma (0.006 m^3/s (Migliorini et al., 2016)). This means that the fallout from Hapi is ∼96% in volume (0.006 m^3/s represent the 4% of the total erosion rate calculated in the same period). Fulle et al. (2018) estimated the fallout of the perihelion southern erosion. This value is about 80% in volume, lower than the fallout from Hapi's activity. This probably means that the structure of the neck, which is a region surrounded by steep walls, causes dust particles to direct collide with the walls themselves (Shi et al., 2018). The power index of the differential dust size distribution is -4 at dust sizes >1 mm (Rotundi et al., 2015), and this allows to assume that the fallout is mainly composed of particles smaller than about 1 cm, and that the bulk density of the fallout is about 800^{+500}_{-100} kg/m^3. In this context, the erosion rate in August, 2014 from the considered 0.2 km^2 becomes 120^{+160}_{-60} kg/s, which, divided by the corresponding water vapor loss rate of 1.2 kg/s (Gulkis et al., 2015), provides Hapi's dust-to-water mass ratio (Rotundi et al., 2015) at the erosion of 100^{+140}_{-50}. The inverse of the lower limit of the dust-to-water ratio provides Hapi's water ice fraction of 2% in mass. Since the Hapi's surface ejecting dust was probably larger than 0.2 km^2, this value can be considered as an upper limit because a larger area means an increasing of the dust volume loss rate. Coming from the crust of the chunks in the deposit (Fulle et al., 2018b), the dust ejected by Hapi is dry (Fulle et al., 2018a). This is supported by the match between the water loss rates provided by local (ROSINA) and remote (MIRO) observations (Marshall et al., 2017) in August, 2014, which are $< 1\%$ in mass of the measured Hapi's erosion rate. The fallout from Hapi is inert, but Hapi's erosion of 1.7 m during the inbound orbit is statistically diluted by a factor about 250 (namely, the total nucleus surface divided by 0.2 km^2), providing an average dry fallout <1 cm thick over all the nucleus. This layer is negligibly thin with respect to the total southern erosion of at least 4 m (Fulle et al., 2018b), with about 97% in volume of the total ejected material in chunks of size >1 cm, according to the perihelion dust size distribution (Fulle et al., 2016). VIRTIS measured the average water ice abundance at a maximum depth of a few μm (Capaccioni et al., 2015). At Hapi's sunrise, the water ice fraction was up to 15% in volume due to the surface ice accumulation during the night. This frost sublimates after sunrise and is consistent with the found average upper limit of 2% in mass. This value is also consistent with the assumptions of thermo-physical models (Blum et al., 2017; Hu et al., 2017a,b) fitting the inbound time evolution of the water loss rate.

4.5 Conclusions

In this study, we measured the seasonal evolution of Hapi's deposit erosion/accretion with a vertical accuracy of 0.2 m, providing an upper limit of 2% in mass for Hapi's water ice fraction, which fixes the pristine 67P ice content in the range from 1% to 15% in mass. The corresponding Hapi's fallout of about 96% is consistent with the model (Fulle et al., 2018b) linking the meters thick southern erosion of pristine nucleus material to the northern fallout. With this model, considering all the possible ice losses during the transfer of the fallout from the southern sources onto Hapi (using Eq.s 2 and 3 in Fulle et al. (2018b)), the water ice fraction in Hapi's deposit of $(1.2 \pm 0.8)\%$ in mass provides a refractory-to-ice mass ratio ranging from 6 to 110 in the perihelion-eroded volume of pristine nucleus material of 4×10^7 m^3, corresponding to a 67P pristine ice mass fraction of $(8 \pm 7)\%$ in mass. This value is in the range from 5% (Mogi et al., 2017) to 20% (Garenne et al., 2014) measured in CI-chondrites and in the InterStellar Medium (ISM) (about 20%). The molecular abundance of water ice in molecular clouds (Boogert et al., 2015), and likely in the outer protoplanetary discs, $H_2O/H \approx 10^{-4}$, and the hydrogen-to-refractory mass ratio ≈ 100 in the InterStellar Medium (Spitzer Jr, 2008) imply a refractory-to-water mass ratio $\approx 10^4/(18\times100) \approx 5$ in the discs beyond the snow line. This implies that either the water abundance of the ices incorporated into comet 67P were lower than the ISM value mentioned above, or some water was lost in its formation. The first hypothesis is supported by observations indicating a $\leq 10^{-4}$ abundance of the water sublimated from ices in the hot corinos of Solar-type protostars (Ceccarelli et al., 2000; Visser et al., 2013). These results imply water trapping mechanisms more efficient in possible asteroidal chondritic parents than in comets (Lorek et al., 2016), a negligible water loss by the catastrophic collisions fragmenting asteroids into chondrites (unless CI-chondrites, after their formation were enriched of water to values higher than the ISM average), and a rather uniform water ice radial distribution in the protoplanetary disc beyond the snow line, consistent with the significant radial mixing of the disc explaining the minerals found in comets (Fulle et al., 2017; Ogliore et al., 2009). The possibility that such a mixing from the inner to the outer disc involved also water ice might help to explain the differences in the D/H ratio measured in comets, and the possible origin of some CI-chondrites much more external than the asteroidal belt (Walsh et al., 2011; Gounelle et al., 2006).

Chapter 5

Thermal and Stress Analysis in Boulders of Comet 67P

The output from a fragmentation process depends on the geometry of the parent body and on the type of fragmentation applied to this material. Thermally induced fragmentation is considered to be an active process in the Solar System. Thermal stress weathering is defined as rock breakdown due to the expansion and contraction of a rock induced by heating and/or cooling (Lamp et al., 2017). The two mechanisms responsible for the breakdown of rock via thermal stress weathering are thermal shock and thermal fatigue (Hall and Thorn, 2014). Thermal shock causes rapid failure in the material as a result of a sudden variation in temperature. Thermal fatigue failure results from cyclic thermal contraction and expansion of the material. This stress leads to deformation and macroscopic cracks in the involved medium. In this scenario, temperature changes, spatial temperature gradients, and high temperatures are considered as the main constraints responsible for thermal fatigue that can result even without mechanical loads. In addition to macroscopic cracks, rocks contain microscopic cracks at the scale of their individual mineral grains, and thermally induced rock breakdown is driven by the propagation of cracks at both scales (Kranz, 1983; Molaro et al., 2015). The minerals expand and contract by different amounts as the temperature changes, and propagate in different directions with respect to their crystal lattice. The accumulation and propagation of microcracks in boulders over time contributes to propagation of macroscopic-scale fractures, resulting in an overall reduction in strength of material and disaggregation of rocky material (Molaro et al., 2017). The response of rocks to the application of heat depends upon their composition, structure, density, thermal properties, and mechanical properties. Furthermore, the morphology and superficial texture of a boulder determines the amount of radiation received from the Sun (Molaro et al., 2015).

There are many active processes on airless bodies that contribute to rock breakdown, such as space weathering (physical, chemical, and sublimation weathering), impact cratering, and micrometeorite bombardment.

These processes will interact with each other to some degree, but each of these dominates on a given body. For example, micrometeorite bombardment dominates regolith generation on the Moon (Basilevsky et al., 2015; Ghent et al., 2014; Hörz and Cintala, 1997), and on Mercury macro- and micro-impactor flux plays an important role in regolith production (Cintala, 1992; Le Feuvre and Wieczorek, 2011). However, breakdown due to thermal stress is not yet well constrained, and a better understanding about how this process acts on airless surfaces will lead to a better characterization of mechanical and thermal processes of these bodies.

In 1936, Griggs performed a series of experiments to determine whether thermal stress can cause and contribute to rock breakdown. The effects of pressure and temperature on fracture was investigated, and he concluded that there were insufficient evidences to link solar insolation and deformation of rocks (Griggs, 1936). However, the thermal stress weathering has assumed an increasing role in the study of fragmentation, allowing the emergence of new laboratories focused on the understanding of how changes in rock temperature can contribute to rock breakdown. Fatigue and shock processes can be studied from two different perspectives. The deformation of the material and the propagation of fractures can occur both at the level of mineral grains, but also at the macro level. The thermal expansion behavior of consecutive mineral grains due to the expansion and contraction of the material can propagate microfractures along several grains (Kranz, 1979; Sprunt and Brace, 1974). The propagation of microfractures over time may disaggregate the material, increasing the porosity, and decreasing the material strength (Viles and Goudie, 2007). If the stress exceeds the strength of the material, the object's structure fails. The large diurnal temperature range and the repeated heating and cooling exerts stress on the outer part of the rock, contributing to microfractures to coalesce into larger cracks. It became clear soon that laboratory tests should have been supported by field studies, to collect in situ data. The desert was considered to be the ideal place for analyzing the solar-induced fragmentation. McFadden et al. (2005) and Eppes et al. (2016) investigated fractures in desert boulders in Australia and Mongolia, finding that these boulders show a predominant N-S orientation, suggesting a link between cracks formation and Sun moving (D. McFadden et al., 2005; Eppes et al., 2016). Viles and Goudie (2013) monitored marble in the Namib desert to detect any possible structural weakening of rocks due to daily temperature fluctuations. Fracture mechanics was developed during World War

I by A. A. Griffith. He formulated a theory according to which the amount of energy required to propagate cracks is related to the amount of energy of the crack walls at the edge (Griffith and Gilman, 1968). He performed several experiments to calculate the strength of materials, noticing that this parameter was higher in vacuum than in atmosphere. This led to the exploration of the role of the atmosphere in fragmentation. What distinguishes the two situations is the presence of fluids in materials. This can be reflected in the variation of some physical properties of materials, such as the strength, which is influenced by the presence of fluid within the microcracks (Orowan, 1944). The presence of fluids causes a decrease of localized strength of the material. Experiments on lunar analogue showed that thermal expansion in a vacuum is the same as in atmosphere (Thirumalai and Demou, 1974), suggesting that vacuum may not arrest the solar-induced thermomechanical fragmentation, but may change its properties (Molaro et al., 2017).
In this context, the opportunity to study the thermal stress weathering on airless bodies became fundamental. Spacecraft observations allow to measure diurnal temperatures and temperature gradients, while numerical simulations contribute to the analysis of thermal stresses.

In this chapter we examine the question whether thermal fatigue weathering plays a role in the fragmentation of boulders on comet 67P. Following the work of Molaro et al. (2017), we performed a theoretical study of transient temperature, thermal stress, and fracture analysis in the context of general fracture mechanics theory. The aim is to determine if subcritical crack propagation is likely to occur under thermal stresses. To model stresses in boulders, we use COMSOL Multiphysics Modeling Software, a cross-platform finite element analysis, solver and multiphysics simulation software. This simulation environment allows to set up the model by defining the geometry and mesh, specifying physics and material properties, solving the model, and post-processing the results.

5.1 Thermal and Stress Model

In this section, we will model temperatures and stresses in a specific boulder located in the Imhotep region of comet 67P. We selected two specific points of the comet's orbit, aphelion (22 May, 2012) and perihelion (13 August, 2015). This choice was made to compare the two points with the largest possible insolation difference. To build a suitable thermo-mechanical model, we used a terrestrial approach based on quantifying temperature changes and use them as the cause of thermally induced damage and crack propagation.

Figure 5.1: Left panel: split rock from the Atacama Desert, Chile. Volcanic rocks in the coastal plain here are affected by intense heating and cooling as well as salt weathering. Right panel: fissuring through displacive growth of gypsum in limestone, Namib Desert (Bourke et al., 2007a).

The obtained preliminary results do not intend to describe the global behavior of the comet, but are considered as a starting point to extend the analysis to different areas of the comet nucleus.

5.1.1 Data Selection

The selection of the proper boulder is not a straightforward matter because it is difficult to link the morphology and texture of a rock with the processes responsible for its appearance. As shown in the *Photographic atlas of rock breakdown* (Bourke et al., 2007a), physical and thermal weathering (Dorn, 2003) can enhance the preexisting weakness, such as fractures and joints, within boulders and produce split rocks. In Fig. 5.1, examples of boulders affected by thermal weathering are shown. The processes responsible for the production of split rocks are scalar dependant (Bourke et al., 2007a). In fact, larger blocks may be produced by unloading, whereas smaller blocks are likely to be formed by physical weathering.

The cyclic stresses that develop within boulders due to the sudden temperature variation related to the day/night cycle, lead to crack's growth at different scales. Cracks can be produced by different processes, but each of them is reflected in the final pattern and orientation of the resulting cracks. Eppes et al. (2016) collected crack orientation measurements in 1500 rocks photographed by Spirit rover on the Martian surface, concluding that cracks exhibit preferred orientation compatible with solar-induced thermal stresses. On the contrary, fractures produced by shattering would exhibit random az-

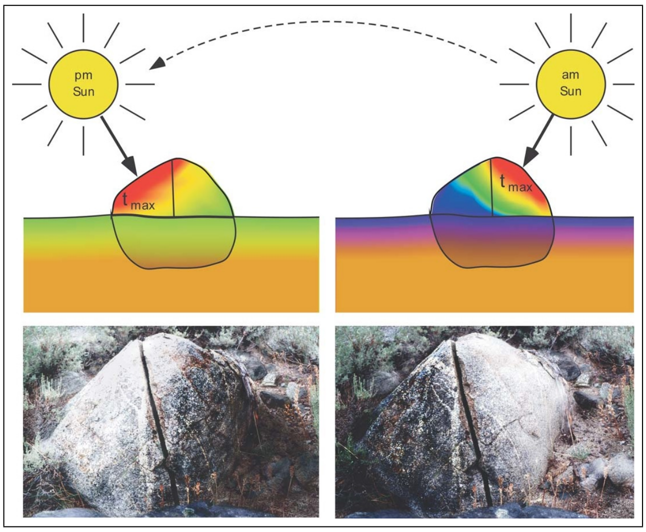

(D. McFadden et al., 2005)

Figure 5.2: Link between the diurnal solar pattern that creates tensile stress in rock, and boulder that exhibits cracking. The crack is perpendicular to the direction of the Sun's rays. Hot and cold temperatures are associated to warm and cool colors.

imuthal orientation, and the freezing process would not produce orientations depending on the Sun's angle. The preferred orientation can be explained by directional insolation heating, as they reflect the recurring thermal stresses (Eppes et al., 2015). In Fig. 5.2, a cartoon depicting the link between the diurnal solar pattern and boulder cracking is shown. In this figure, it is evident that the crack is perpendicular to the direction of the Sun's ray. For these reasons, we looked for a boulder showing signs of erosion, small fragments around it, and a preferred cracks orientation. In Fig. 5.3, the selected boulder is shown. As described in Chapter 3, Cambianica et al. (2019) characterized this sub-population calculating the cumulative size-frequency distribution, and analyzing the shape of fragments. The cumulative boulder size-frequency distribution per unit area has a power-index of 2.7 +0.1/ -0.1 (see Fig. 3.11). This population is composed of a main boulder (23.1 m in size) and 341 fragments, the size of which ranges from 0.3 to 8.3 m in diameter. The distribution of the fragments follows fractal rules (see Fig. 3.15), and the fragments are generally compact and roundish in shape (see Fig. 3.20). To complete the quantitative description, we analyzed the visible cracks on the surface of the boulder. We measured the cracks dimensions, the spacing between them, and their orientation. Following the definition of

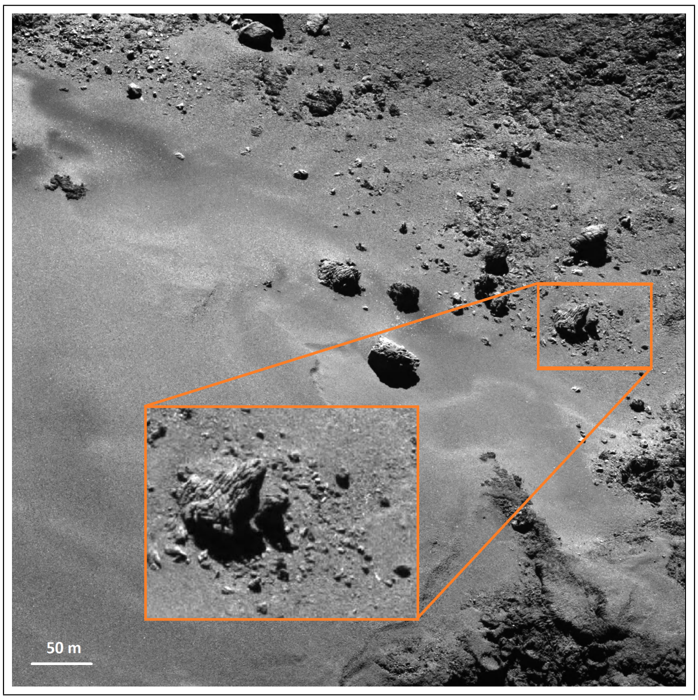

Figure 5.3: OSIRIS NAC image taken on 23 July, 2016, with a spatial scale of 0.28 m/pixel. This area is located in the Imhotep region. The selected boulder is singled out (orange box).

crack as a linear void of which ambient light does not illuminate the bottom (Eppes et al., 2015), we used Arcgis 10.3.1 software (ESRI, 2011) to manually track all cracks. The 12 measured cracks are between 3.8 and 26.6 m in length, and the average length is 13.2 m. We also measured the spacing between two adjacent fractures, coming up with an almost constant value of 1 m. In Fig. 5.4, a sketch of the crack distribution is shown. The measurements are reported in Table 5.1. Finally, we analyzed the orientation of the cracks. All traced cracks show a non-random, and strong north-south orientation. This preferred orientation is compatible with solar-induced thermal stresses.

5.1.2 Geometry and Mesh

The geometry used in this study consists of a geodesic polyhedron embedded in a rectangular volume (see Fig. 5.5). Geodesic polyhedra are a good approximation both of a sphere (for the basic model) and a boulder, allowing to define more complex and realistic shapes. To define the radius of the boulder, we virtually joined all fragments to the parent body, knowing

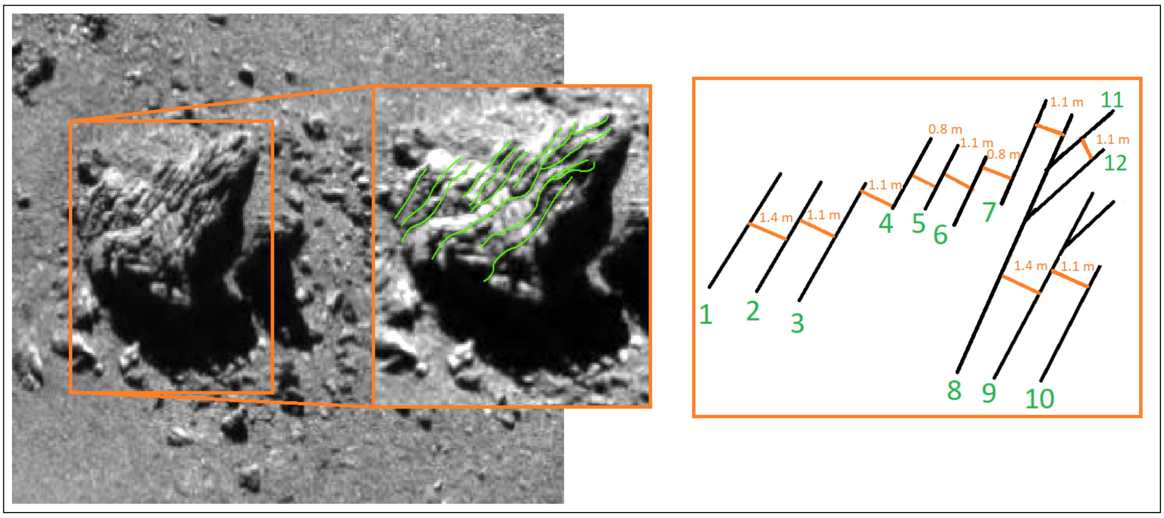

Figure 5.4: Detail of the OSIRIS NAC image taken on 23 July, 2016. The middle box shows the mapped cracks (in green). In the right box, a sketch of the fractures pattern is shown. The green number defines the ID of each crack (see Table 5.1), the orange number defines the spacing between two consecutive fractures.

ID	Length (m)	Spacing (m)
1	5.6	
2	13.7	1.4
3	11.8	1.1
4	10.1	0.8
5	10.9	1.1
6	10.7	0.8
7	26.6	1.1
8	18.1	0.8
9	18.2	1.4
10	19.1	1.1
11	3.8	1.1
12	9.5	1.1
Average length	13.2	
Average spacing		0.98

Table 5.1: Length of cracks and spacing between two consecutive cracks (distance between the referred crack and the previous one). The ID of each crack refers to Fig. 5.4.

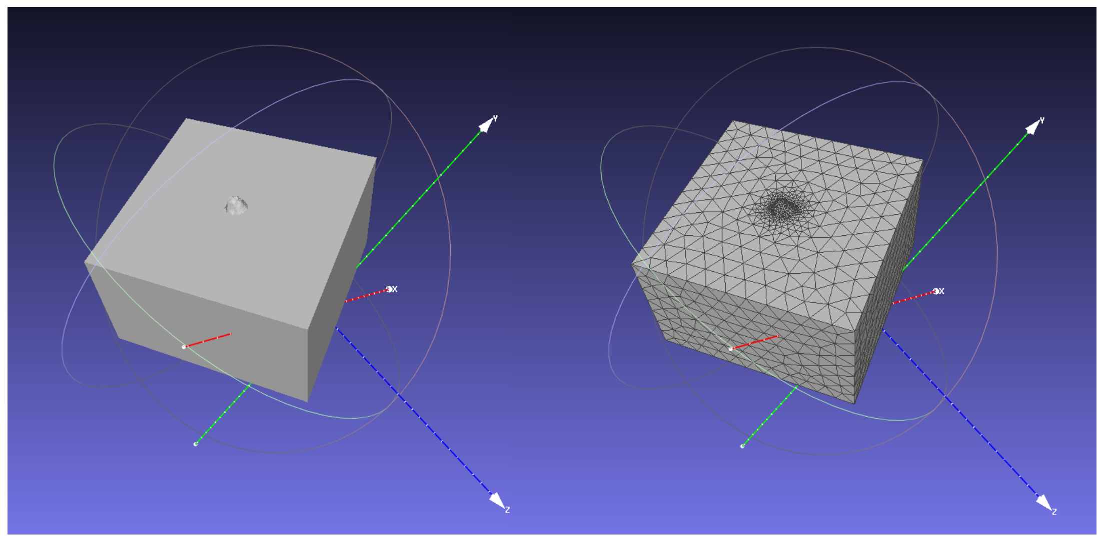

Figure 5.5: Geometry and mesh of the cubic volume (1 km × 1 km × 1 km) with a 40 m size boulder.

their number and sizes. The final shape is composed of a 40 m size boulder, and the volume is modeled with a width and depth of 1 km.

As the size of the model domain can affect its thermal behavior, we defined the depth of the cubic volume much larger than that of the diurnal thermal skin depth (estimated to be ~ 6 mm by MIRO (Gulkis et al., 2015)). COMSOL provides tools to generate objects and perform Boolean operation on them, but we preferred to use BLENDER (R Core Team, 2013), an open source 3D creation suite, because it allows to build objects directly on the 3D comet shape, keeping the proper orientation of the selected region. We used the SHAP8 V.2.1 comet shape model, which represents an advanced model based on a data set of 20679 OSIRIS-NAC images and 6072 OSIRIS-WAC images acquired between 11 July, 2014, and 30 September, 2016. The average image resolution is 4.2 m/pixel. This model covers the whole surface of the nucleus including the south pole region which was not imaged at the time the SHAP2 was reconstructed. As shown in Fig. 5.6, the z-axis of the reference system is parallel to the rotating axis of the comet. This assumption allows to calculate the insolation in realistic geometric conditions. We performed Boolean operations on the two domains. The boulder and the block are contacting (but not intersecting) objects, and the cloud of contact points is defined as a smooth depression of where the boulder is placed. To generate the mesh we used COMSOL's built in tools. Physically, the two objects are discrete and have different properties. Therefore, we generated

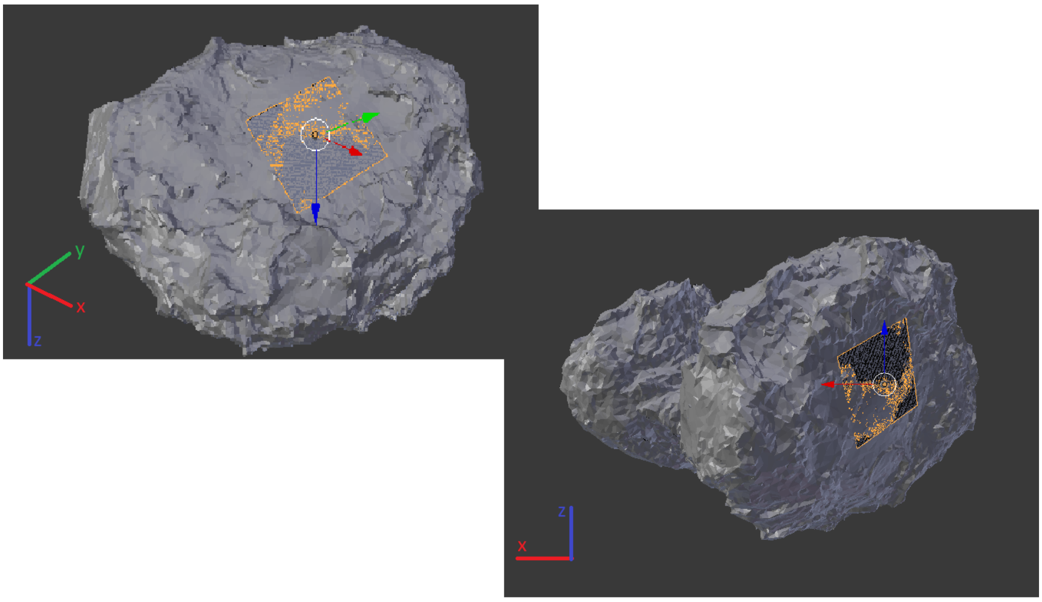

Figure 5.6: Location of the used reference system with respect to the comet nucleus. The z-axis is parallel to the rotating axis of the comet 67P.

two different meshes, one for the boulder and one for the block. The boundary between the two domains is defined as *Thermal contact*, since heat is exchanged between them. This approximate method computes the effective thermal conductance between two surfaces in contact. The resulting mesh is composed of 6552 tetrahedral facets (of which 2232 are superficial elements), and the sizes parameters in each domain has been adjusted to ensure the quality of the elements was appropriate. The reason is that the shape of the mesh elements directly affects the numerical convergence and accuracy of the solution. A mesh element has a good quality, if these effects are beneficial. In Fig. 5.7 the skewness of the superficial mesh elements is shown. The minimum quality of the elements is 0.33 and the average value is 0.85, where unity expresses the highest quality.

5.1.3 Material Properties

Comets nuclei composed of rock, dust, H_2O and CO_2 ices (as major components), represent a general picture of the nucleus composition. One of the major achievements of the Rosetta mission has been the possibility to analyze the chemical composition of the surface. A recent review about the current knowledge of comet 67P nucleus composition (Filacchione et al., 2019)

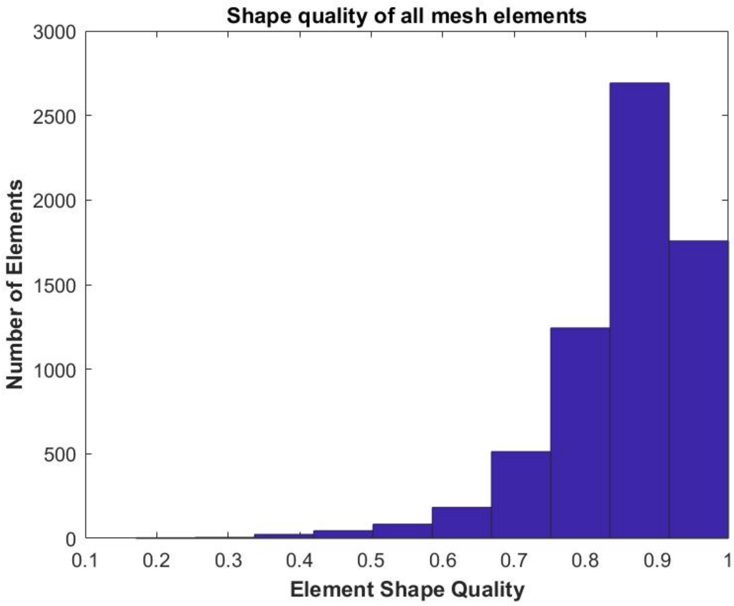

Figure 5.7: Statistical analysis of the mesh shape elements. The x-axis shows the element shape quality in terms of skewness, while the y-axis shows the number of triangular elements.

Property	Symbol	Unit	Value
Thermal Conductivity	k_g	W/m K	24
Density	ρ_g	kg/m^3	2250
Porosity	p_g	%	0.7-53
Surface Emissivity	ϵ_g		0.90
Heat Capacity	Cp_g	J/kg K	708
Coefficient of Thermal Expansion	α_g	1/K	4-8 10^{-6}
Modulus of Elasticity	E_g	GPa	20
Thermal Inertia	I_g	K/m^2 s$^{1/2}$	10-50

Table 5.2: Material properties for graphite.

states that the nucleus consists of a mixture of organic components, minerals, and water ice. The organic compounds contain COOH- and OH-groups, polycyclic aromatic hydrocarbons, and refractory macromolecular materials (CH_2 and CH_3). Carbons are considered as the most plausible materials contributing to the reflectance spectra of the comet. These elements are mixed with minerals, including silicates, Fe-sulfides (pyrrohtite and/or troilite), and possibly ammonia salt. Carbon can be found in two natural crystalline allotropic forms, such as diamond and graphite. In this scenario, the boulder and the block are assigned with the properties of graphite. The material properties for graphite are provided in Table 5.2. All of these properties are constant. In the case of 67P it was found by MIRO that the thermal inertia of the cometary surface is between 10 and 50 K/m^2 (Gulkis et al., 2015). We decided to modify this property of graphite to simulate the propagation of heat in a material as realistic as possible.

5.1.4 Physics

To model temperatures and stresses throughout a cometary day, COMSOL solves the heat equation for heat transfer in solids and displacement over time. The two heat equations are given by:

$$c_p \rho \frac{dT}{dt} + \bigtriangledown Q = 0 \tag{5.1}$$

and

$$\rho c_p = k \frac{dT^2}{dz^2} \tag{5.2}$$

where c_P is the specific heat, ρ is the density, T is the temperature, Q is the heat flux, k is the thermal conductivity, and z is the depth into the rock interior. The heat equation for the temperature used to model heat transmission by conduction, convection, and radiation in solid domains, corresponds to the differential form of the Fourier's law. Deformations in solids may be caused by external loads, chemical reactions, weathering, and changes in temperature. To evaluate the transformation of a body from a reference configuration, the following equation can be used:

$$M \frac{d^2 u}{dt^2} + \bigtriangledown \sigma = 0 \tag{5.3}$$

where M is the mass density tensor, u is the displacement field, and σ is the stress tensor. The displacement u is proportional to the Cauchy Stress Tensor (S):

$$\rho \frac{\delta^2 u}{\delta t^2} = f - \nabla S \tag{5.4}$$

where f is the volume force vector, and the density is that of the deformed state. The Cauchy Stress tensor is a second order tensor composed of nine components σ_{ij} that defined the state of stress at a point inside the material. According to Cauchy's fundamental theorem, by knowing the stress vectors and the three mutually perpendicular planes of point, the stress vector on any other plane passing through that point can be found through coordinate transformation equations. In the case of thermal stress, the stress tensor is related to both the elastic strain (Σ_{el}) and strain tensor (Σ_{th}):

$$S = D : (\Sigma_{el} - \Sigma_{th}) = D : (\Sigma_{el} - \alpha(T - T_0)) \tag{5.5}$$

where T_0 is the strain reference temperature, and D is a 4^{th} order elasticity tensor that depends on the poisson's ratio (ν) and Young's modulus (E) of the material as follows:

$$D = \frac{E}{(1+\nu)(1-2\nu)} \begin{pmatrix} 1-\nu & \nu & \nu & 0 & 0 & 0 \\ \nu & 1-\nu & \nu & 0 & 0 & 0 \\ \nu & \nu & 1-\nu & 0 & 0 & 0 \\ 0 & 0 & 0 & \frac{1-2\nu}{\nu} & 0 & 0 \\ 0 & 0 & 0 & 0 & \frac{1-2\nu}{\nu} & 0 \\ 0 & 0 & 0 & 0 & 0 & \frac{1-2\nu}{\nu} \end{pmatrix} \tag{5.6}$$

The heat transfer and solid mechanics physics are coupled by the COMSOL's Multiphysics tool, which creates a thermal expansion link between the two environments.

COMSOL can perform the calculation using a fully coupled or segregated method. The fully coupled approach forms a single system of equation that solve for all the fields and includes all of the couplings between the multiphysics effects at once, within a single iteration. The segregated approach will not solve for all the fields, but it subdivides the problem in segregated steps. We choose the second approach because it solves sequentially within a single iteration, and thus less memory is required. The model was run for several iterations of the cometary day to ensure stable behavior.

5.1.5 Boundary Conditions and Model Assumptions

Incident solar radiation Q is applied to the geometry surface by utilizing the COMSOL's *Heat transfer in solids* module. COSMOL allows to define the external solar radiation source by defining the heat source as a black body at infinite distance with a specific temperature. However, thanks to the Rosetta mission, several specific models of insolation and sublimation of comet 67P have been developed. We therefore decided to calculate the incident heat flux received by the surface of the boulder following the method

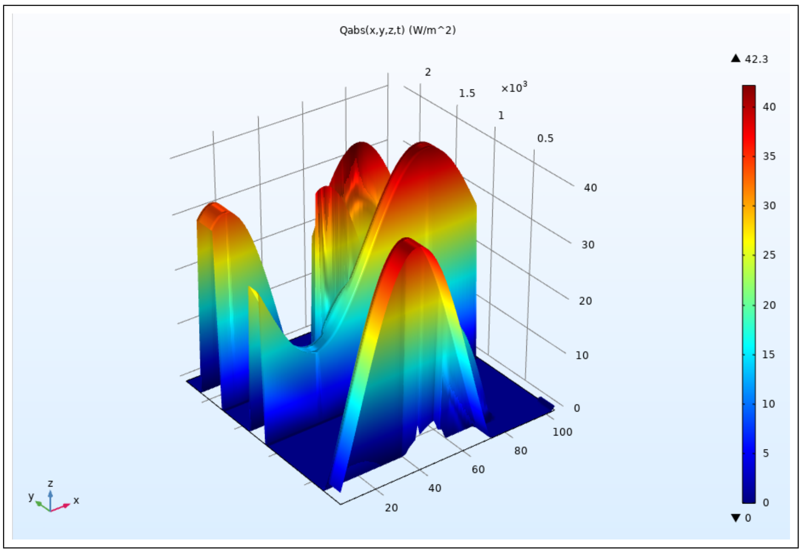

Figure 5.8: Absorbed heat flux (Q_{abs}) by the boulder at aphelion as a function of space and time. The x-axis represents the time steps used to discretize the cometary day (100 step = 1 cometary day), y-axis contains information about the coordinates of each facets of the mesh, and z-axis shows the absorbed heat flux (W/m^2).

developed by Keller et al. (2015). The insolation is calculated as a function of heliocentric distance and diurnal variation in order to predict the sublimation of water ice. This model consists of about 108000 facets and the insolation of a single facet is calculated taking into account its orientation with respect to the Sun. Because of the concave shape of the comet, for each time step the mutual occlusion of the facets is checked. Furthermore, the energy balance of the comet is influenced by Sunlight reflected by mutually facing facets in the presence of concavities. This enhancement of the local flux is included in the final amount of heat flux. This consideration is fundamental because allows to consider different geometries. To calculate the heat flux, the orbit of comet 67P around the Sun has been discretized in steps of 2.5° in true anomaly, and the spin is discretized in steps of 2% in rotational phase (Keller et al., 2015). We performed the calculation using the same geometry and mesh used in our model to keep the correspondence between facets in both models.

The surface of the volume and the boundary of the boulder that protrudes above the volume are the only boundaries that receive incident radiation. We calculated the insolation received at aphelion (22 May, 2012) and perihelion (13 August, 2015) as a start. The resulting incident solar radiation has been supplied to COMSOL via text file, and COMSOL considered this data as a surficial boundary conditions. In Fig. 5.8 an example of how COMSOL interprets these data is shown.

After the generation of the two meshes, we defined the two domains in thermal contact since they interact radiatively with each other. This condition acts as a boundary layer between domains, and this layer moves through the domains, remaining in contact with each other. As shown by Molaro et al. (2017), this assumption generates an artificial stress of the order of 10^{-1} MPa, neglegible compared the other stresses considered in this research. The heat transfer across thermal contact boundary is calculated as follows:

$$Q = c\Delta T \tag{5.7}$$

where T is the temperature and $c = \frac{K_{eff}}{\delta}$ is the gap conductance, K_{eff} is the effective thermal conductivity, and δ is the thickness of the boundary layer. The cubic volume is defined as periodic with respect to temperature, and fixed with respect to displacement. This choice is necessary to improve computational efficiency, and does not affect the final calculated stresses and displacements (Molaro et al., 2015; Molaro et al., 2017). The bottom boundary of the cubic volume is also held fixed. The surfaces are defined mechanically free, and we defined a strain reference temperature set for the boulder's initial temperature.

Stresses are influenced by different factors. Material inhomogeneity is one of these, and it can cause internal loading. Using a Finite Element Method, material inhomogeneity and anisotropy can be handled rather easily. Each consitutent for a given rock type differs from others in both texture and grain size. At the same time, average grain size varies with rock types. Individual crystals are chemically heterogeneous and, in general, possess different physical properties. However, the grain distribution is very random. As a result, on a microscopic scale, hard rocks usually have homogeneous properties. An isotropic behavior is pronounced only for sedimentary stratified rocks and metamorphic rocks which have well defined cleavage planes. For hard rocks, properties are assumed to be isotropic.

Preexisting microcracks represent another influencing element. Cracks are created in the form of voids as a result of removal of gases and water vapor which are trapped at high pressure and temperature during rock formation. These voids are extremely small compared to faults and joints and are usually in the form of microcracks in non porous, hard, dense rocks. Nevertheless, they have very defined effects on rock properties, due mainly to material discontinuity and the pressure of accumulated moisture in the cracks. Cracks have a very significant effect on fracture propagation. For comparatively

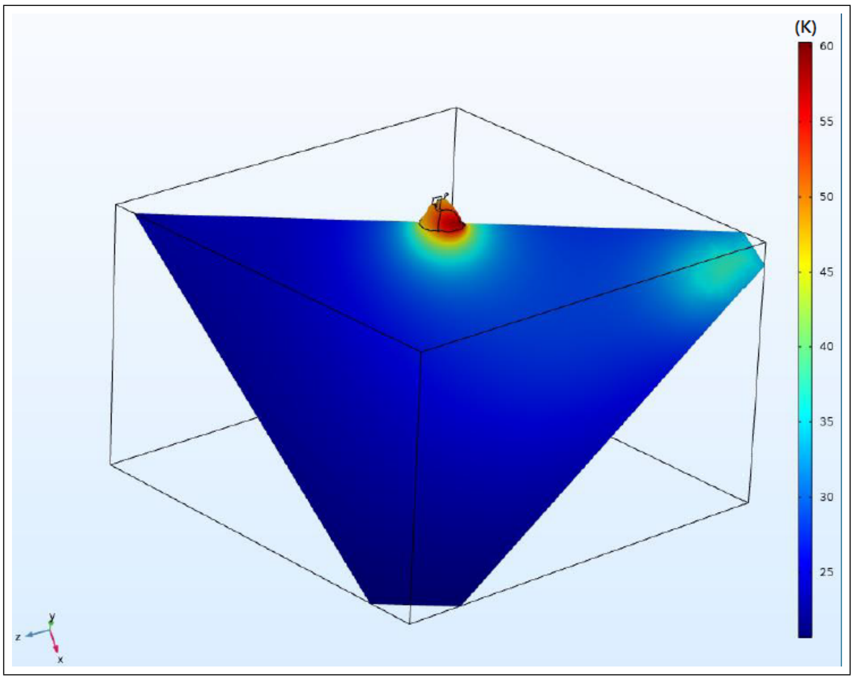

Figure 5.9: Initial temperature of the geometry. The bright spot on the right is an artefact.

non-porous, hard rocks, cracks occupy less the 1% of the total volume of rock as compared to $10 - 20\%$ for highly porous rocks. Hence, for hard rocks which possess a very low apparent porosity, the microcracks effects can be neglected.

5.1.6 Initial Values

The ambient temperature is set to 2.7 K, the temperature of airless environment. To calculate the initial temperature of the geometry, we run the simulation as many diurnal cycles at aphelion as required to stabilize temperature at the boulder's center. As a result, the temperature distribution shown in Fig. 5.9 is obtained, in which the initial temperature of the block and boulder surfaces are of the order of 30 K and 50 K respectively. This is in line with the subsurface temperatures measured by MIRO during the polar night in the southern regions. During the period August-October 2014, the subsurface temperatures were in the range 25 - 50 K (Choukroun et al., 2015). Before these observations, the southern polar regions had not been illuminated for approximately five years.

5.1.7 Stress Parameters

In structural engineering and strength of materials, an object may be subject to different types of forces and torques or a complex combination of them. These forces and torques give rise to different types of stresses at different points in the object. Depending on the material and the stress generated, the object may fail due to exceedence of different types of stresses. Before presenting and discussing the results, we introduce the most common theories used to describe the thermal stress weathering and the crack propagation. The reason for that is to understand which is the most suitable damage theory able to describe our results.

Von Mises Stress

In 1933, Von Mises proposed that yielding occurs when the distortion energy reaches a critical value. This critical value is specific for each material, and can easily be obtained by performing a simple tension test. When a body in an initial state of equilibrium is subjected to a force, the body deforms until it reaches a new state of mechanical equilibrium or deformed state. The relations between stresses and the deformation of the body, which characterizes strain, are called *Stress-Strain relations* (Von Mises and Windenburg, 1933). The Von Mises stress is a value used to determine if a given ductile material will fail. The Von Mises yield criterion states that if the stress of a material exceeds the yield limit of the same material under simple tension, then the material will yield. The amount of distortion energy u_d required to deform the shape of an object defines the Von Mises stress parameter. This energy is given in terms of the principal stress as:

$$u_d = \frac{1+\nu}{3E}\left[\frac{(\sigma_1-\sigma_2)^2+(\sigma_2-\sigma_3)^2+(\sigma_3-\sigma_1)^2}{2}\right] \tag{5.8}$$

where ν is the Poisson's ratio and E is the Young's modulus. The distortion energy at the time of failure in a simple tension test is given as follows:

$$u_d = \frac{1+\nu}{3E}\sigma_y^2 \tag{5.9}$$

where σ_y is the tensile yield strength of the material by definition. The condition of failure occurs when:

$$\sigma_y \leq \left[\frac{(\sigma_1-\sigma_2)^2+(\sigma_2-\sigma_3)^2+(\sigma_3-\sigma_1)^2}{2}\right]^{1/2} \tag{5.10}$$

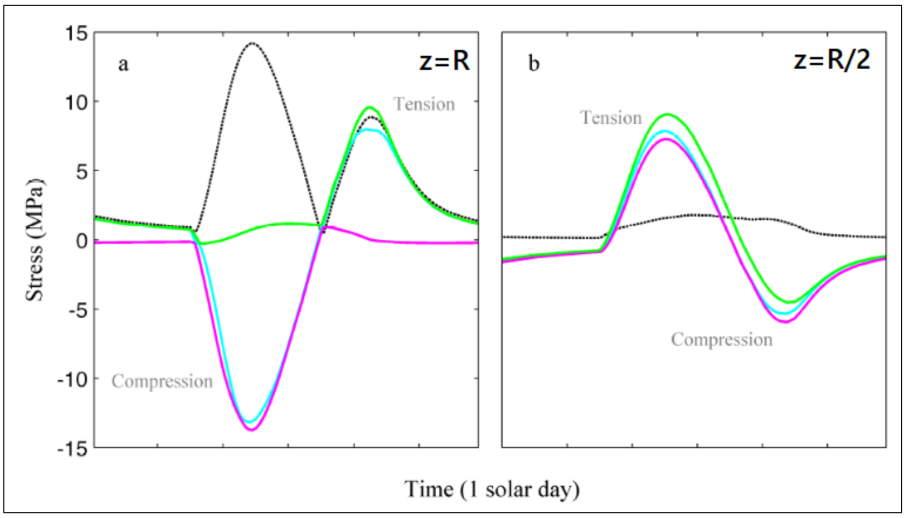

Figure 5.10: Von Mises stress (black dashed), and the first (green), second (cyan), and third (magenta) principal stresses at the top of the boulder (z=R) in panel a, and between the top and the boulder center (z=R/2) in panel b, over one solar day (Molaro et al., 2017).

The Von Mises Stress or *equivalent stress* σ_E can thus be obtained as follows:

$$\sigma_E = \left[\frac{(\sigma_1 - \sigma_2)^2 + (\sigma_2 - \sigma_3)^2 + (\sigma_3 - \sigma_1)^2}{2}\right]^{1/2} \tag{5.11}$$

Molaro et al. (2017) tested the validity of the Von Mises stress in the case of an airless boulder. Figure 5.10 shows the comparison between the Von Mises tress (black dashed line) and the principal stress on the top (z=R) and in the center (z=R/2) of the boulder over time. On the top, the Von Mises stress mirrors the principal stress. Considering a point in the middle of the boulder, this stress is less significant even though the three principal stresses are relevant. This suggests that the ductile yield strength in case of hydrostatic stress (equal tension or compression on all axes) in higher than under simple tension (Molaro et al., 2017). On the contrary, thermally induced stresses are not ductile processes. This leads to the fact that on the top of the boulder, the Von Mises stress quantifies the energy available to propagate cracks when it mirrors the maximum principal stress. However, considering a point in the center of the boulder, the Von Mises stress can not be used similarly, because it is not reflected by the equivalent stress parameter.

Paris' Law

The Paris' law (Paris and Erdogan, 1963) is a crack growth equation that characterizes the rate of growth of a fatigue crack. The Paris equation is:

$$\frac{da}{dN} = c\Delta k^n \tag{5.12}$$

where a is the crack length, N is the number of cycles, and c is an empirically determined parameter. k represents the stress intensity factor which characterizes the load around a crack and is used to predict the stress intensity caused by a residual stress or remote load. The rate of crack growth is experimentally linked to the range of stress intensity Δk seen in a loading cycle. The Paris' law predicts the fatigue crack growth for an N-cycle load. The reason why this cannot be used in our case is that, according to this law, at mid-range of growth rates, variations in microstructure, mean stress (or load ratio), thickness, and environment have no significant effects on the crack propagation rates, by definitions. In the case of boulder fragmentation, instead, chemical environment, ambient temperature, size of the boulder, composition, and cyclic frequency should be considered since they are very influential in crack propagation.

Maximum Principal Stress

The Maximum Principal Stress Theory states that failure in any material occurs when the principal stress in that material due to any loading exceeds the principal stress at which failure occurs in the one dimensional loading test. Furthermore, the Maximum Principal Stress criterion postulates that the growth of the crack will occur in a direction perpendicular to the maximum principal stress, controlling the plane in which the direction of crack propagation occurs. To determine whether this stress causes crack propagation, the linear elastic fracture mechanics theory has to be involved. This theory states that a crack will propagate to failure when the stress intensity factor K_I of a crack exceeds a critical value knows as fracture toughness K_{Icr} of the material (Lamp et al., 2017). The stress intensity factor is defined as follows:

$$K_I = 2\Delta\sigma_1 \left(\frac{c}{\pi}\right)^2 \tag{5.13}$$

where c is the radius of a penny shaped cracks, and σ_1 is the Maximum Principal Stress. The critical fracture toughness is difficult to define if the composition of the rock is unknown. In this case, laboratory experiments have found that for a given material, the critical fracture toughness can be determined as follows:

$$K_{Icr} = \frac{\sigma_t}{6.88} \tag{5.14}$$

where σ_t is the rock tensile strength.

To conclude, we will present results in terms of Maximum Principal Stress, using the convention that compressional stress is negative and tensile stress is positive. In this context, failure occurs when σ_1 reaches a value equal to some yield stress. The Maximum Principal Stress lies along a single plane as long as the material has an isotropic strength, and this assumption can be considered reasonable for rocky materials (Molaro et al., 2017). The Maximum Principal Stress will quantify the amount of tensile stress is available for microcrack propagation.

5.2 Results

In this section we present preliminary results in terms of temperatures and Maximum Principal Stresses (σ_1). We modeled temperatures in two specific points of the 67P orbit, aphelion (22 May, 2012), and perihelion (13 August, 2015).

5.2.1 Aphelion

The farthest point from the Sun of comet 67P's orbit is located at 5.6829 AU. Figure 5.11 shows the temperature cut plane for the considered geometry at intervals throughout the solar day. Midnight is the starting point of the simulation. When the Sun rises (panel a), the upper-right side of the boulder begins to heat quickly, while the left side remains cold because is still in shadow. When the Sun is higher in the sky, more of the boulder is warm (panel b). The boulder starts cooling on the right side when the Sun begins to set. In panel c, the boulder takes longer to cool due to the low thermal conductivity of the graphite. The boulder reaches a maximum temperature of 150 K, and a minimum of 50 K. Despite the strong temperature gradient, the heat is not conducted in the boulder's interior. This is reasonable because in a 40 m boulder made of graphite, the heat wave takes more than 12 hours to propagate. The temperature gradient shows a spatial distribution which follows the motion of the Sun. Figure 5.12 shows the Maximum Principal Stress on a 2D cut plane through the boulder. At sunrise, the boulder begins to heat up, allowing the surface to expand. The expansion creates a new region of tension on the right side of the boulder with a peak of 1.4 MPa.

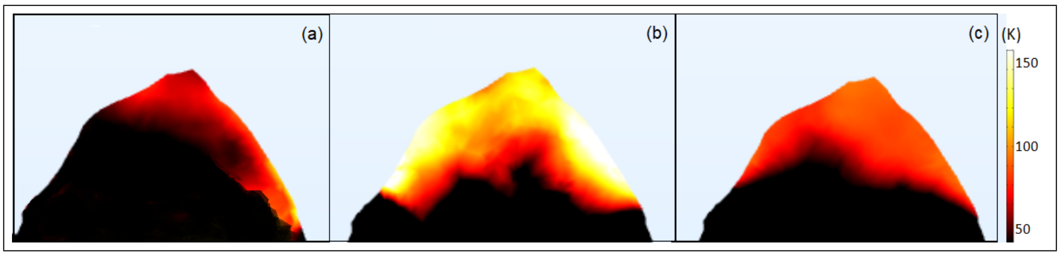

Figure 5.11: Snapshots of the boulder surface temperature at the aphelion. The time between two consecutive snapshots is about 4 hours.

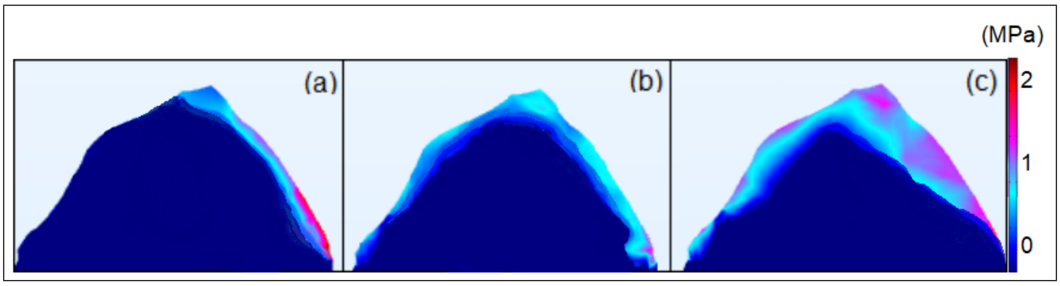

Figure 5.12: Snapshots of the Maximum Principal Stress on a 2D cut plane through the boulder. The time between two consecutive snapshots is about 4 hours. These results refer to the aphelion.

The sudden variation in temperature induces a local thermal gradient in the subsurface, causing a difference in temperature between the surface and the boulder's interior. The center of the boulder remains in a state of strong compression. Stresses during sunset are shown in panel c of Fig. 5.12. The boulder begins to cool and the sudden decrease in temperature causes the contraction of the surface resulting in an increasing of the surface stress.

5.2.2 Perihelion

Figure 5.13 shows the surface temperature for the considered geometry at intervals throughout the solar day. The boulder reaches a maximum temperature of 270 K, and a minimum of 50 K. The maximum temperature is definitely much larger than the aphelion case, as expected. The simulated temperature of the boulder changes throughout the day mirroring the aphelion trend. The right side of the boulder heats up quickly at sunrise, and the center of the boulder remains cool. The temperature gradient is stronger than before, and its spatial distribution follows the movement of the Sun. Figure 5.14 shows the Maximum Principal Stress on a 2D cut plane through the boulder. As the Sun rises, high stresses are induced on the right side of

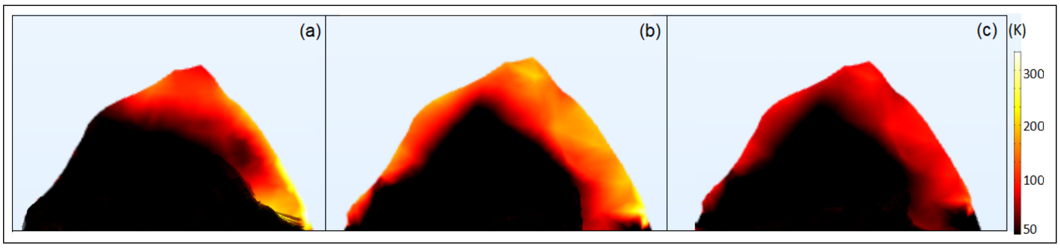

Figure 5.13: Snapshots of the boulder surface temperature at the perihelion. The time between two consecutive snapshots is about 4 hours.

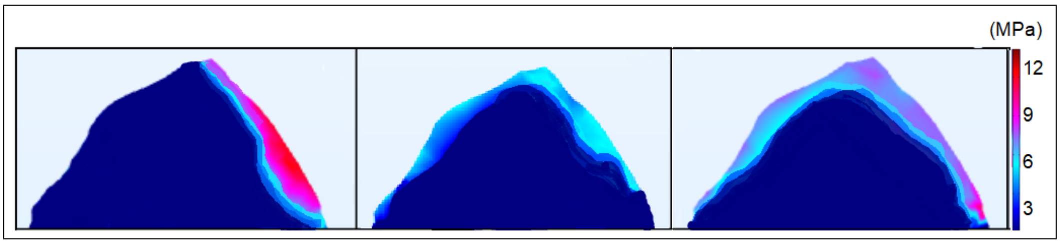

Figure 5.14: Snapshots of the Maximum Principal Stress on a 2D cut plane through the boulder. The time between two consecutive snapshots is about 4 hours. These results refer to the perihelion.

the boulder, when it begins to heat up. As the edge expands, it creates a region of strong tension with a peak of 12 Mpa. This stress is induced by the thermal shock which suddenly generates a difference in temperature between the surface and the boulder's interior. The center of the boulder remains in a state of strong compression. When the Sun is higher in the sky, new regions of tension forms, but changes in temperature are uniform throughout the day and stresses remains quite stable. Panel c refers to stresses induced during sunset. The boulder begins to cool, and the surface is in a new state of tension due to the sudden variation in temperature. Stresses in boulder's exterior are due to the contraction of the surface.

5.2.3 Linear Elastic Fracture Mechanics Theory

To understand whether the simulated stresses can cause crack propagation, we applied the linear elastic fracture mechanics theory. As mentioned in the previous section, the linear elastic fracture mechanics theory states that a crack will propagate to failure when the stress intensity factor K_I of a crack exceeds a critical value knows as fracture toughness K_{Icr} of the material (Lamp et al., 2017). at the aphelion, the Maximum Principal Stress $\Delta\sigma$ reached the maximum value of 1.4 MPa. This leads to a stress intensity

Property	Symbol	Unit	Value
Thermal Conductivity	k_b	W/m K	2
Density	ρ_b	kg/m^3	2700
Surface Emissivity	ϵ_g		0.95
Coefficient of Thermal Expansion	α_g	1/K	10^{-5}
Young's Modulus	E_b	GPa	50
Poisson's ratio	ν_b		0.23
Bolometric Albedo	A_b		0.1

Table 5.3: Material properties for basalt.

factor (see Eq. 5.13) of $K_I = 2\Delta\sigma\left(\frac{c}{\pi}\right)^2 = 0.1$ MPa m^2. The radius c of a shaped crack has been calculated starting from the length of the smallest crack (3.8 m) and this results in c of about 0.61 m. The graphite tensile strength is in range of 4.8 - 76 MPa. This leads to the lower bound of the critical values of the fracture toughness for the graphite equal to 0.70 MPa m^2. This leads to the conclusion that the amount of insolation received by the surface at aphelion is not sufficient to propagate internal microcracks in the boulder. On the contrary, analyzing the perihelion data, the stress intensity factor is $K_I = 1.0$ MPa m^2. This value is sufficient to propagate microcracks.

5.3 Validation Test

To verify the validity of the results, we performed a validation test using the same geometry and varying the composition. The geometry is assigned with the property of basalt. This assumption is not realistic, but allows to test the model comparing the results with those found in literature. The material properties for basalt are reported in Table 5.3. We focused on the surface temperature to compare the results with those obtained by applying the model developed by Keller et al. (2015). The initial values are set at zero. After one complete rotation, the surface temperature of the geometry ranges from 20 to 140 K. The results obtained with the method developed by Keller et al. (2015) show a temperature range from 60 up to 153 K. The two results are different and our temperatures are lower than the temperatures calculated with the Keller et al. (2015) model. This is reasonable because the model we developed is a transient model and considers the heat exchange between the outer space and the geometry. On the contrary, the other model is a stationary model and the received heat flux is stored in the surface.

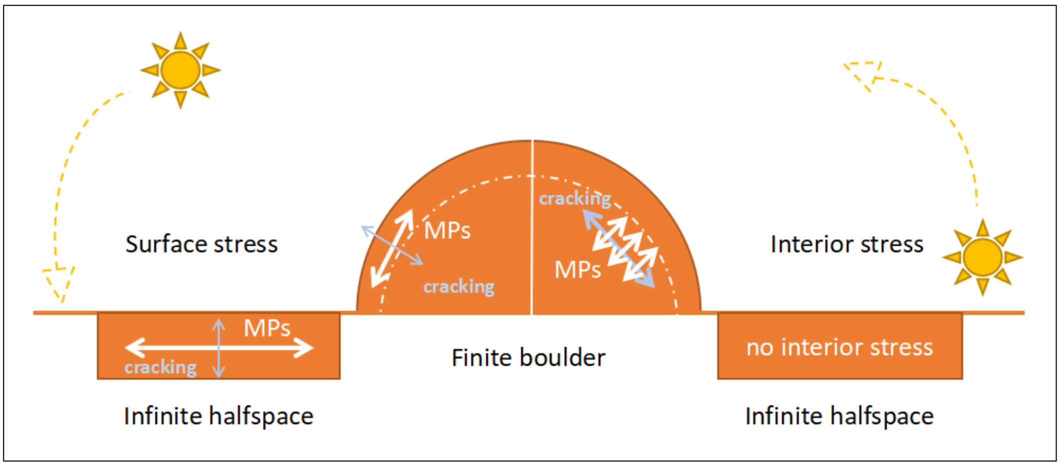

Figure 5.15: Surface and interior stresses in a finite boulder and infinite halfspace. White arrows denote the orientation of the Maximum Principal Stress, and gray arrows denote the direction of crack propagation (Molaro et al., 2017)

.

5.4 Conclusions

In this chapter we investigated the macroscopic thermomechanical behavior of a 40 m boulder located on the Imhotep region by modeling its response to diurnal thermal forcing. The aim was to explore whether the simulated stress is enough to propagate preexisting cracks, since stresses represent the amount of energy available for crack propagation. Another objective was to confirm that exterior stresses are controlled by the sudden variation in temperature, while interior stresses are controlled by the thermal gradient. We modeled the Maximum Principal Stress because it controls the plane in which the direction of crack propagation occurs. Surface stresses drive the propagation of surface-perpendicular cracks, contributing to granular disintegration. Interior stresses act on a plane perpendicular to the path of the Sun and drive the propagation of surface parallel cracks and contribute to surface exfoliation (see Fig. 5.15). Therefore the orientation of cracks can provide insights of how thermal stresses act. Our preliminary results show that in a 40 m boulder size, the combination of thermal contraction and expansion due to the sudden variation in temperature produces high surface stresses regardless of thermal gradient between the interior and the surface of the boulder. No interior stress is present, and the strong flux of heat outside the boulder induces a local thermal gradient in the subsurface, contributing to surface stresses. Usually a boulder shows a bimodal response to diurnal

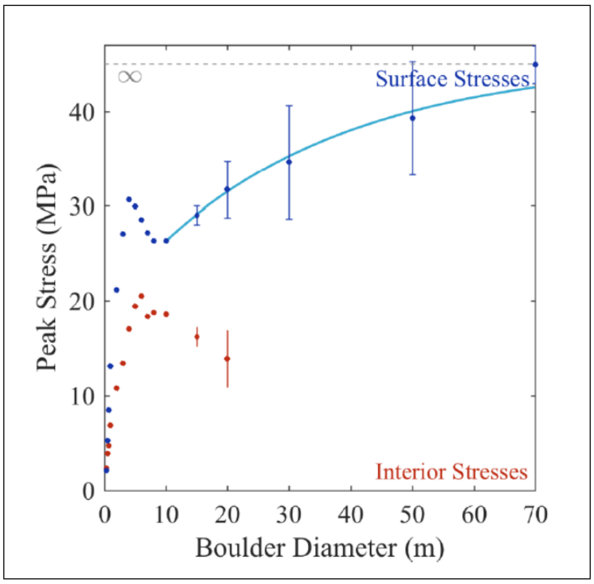

Figure 5.16: Peak surface (blue) and interior (red) stresses experienced in boulders of varying diameter. The curve is the best fit to the surface stresses for diameters $\geq$ 10 m. The grey dotted line represents an infinite halfspace (Molaro et al., 2017)

.

thermal forcing, where surface stresses are induced at the sunrise and sunset due to the expansion and contraction of the surface, while macroscopic thermal gradients during daytime induced interior stresses (Molaro et al., 2017). The fact that this large boulder does not experience internal stress is confirmed by Molaro et al. (2015) and is linked with the surface curvature of the boulder. As shown in Fig. 5.16, boulders whose diameters are ideally infinite can experience only surface stresses. The surface of large boulders as the one under consideration approaches that of infinite halfspace (Molaro et al., 2017). An infinite rock undergoes compression at the surface and can still have tensile stress at the depth as the thermal wave travel downward, but have the same effects as surface stresses. A 40 m boulder can be approximated to an infinite flat rock with no surface curvature. This leads to surface expansion or contraction with no increase in circumference or volume variation (see Fig. 5.17).

In conclusion, the modeled boulder experienced surface stresses induced by the amount of expansion and contraction that it experiences during sunrise and sunset. Sunrise and sunset are then the primary control of shock strength. The heat flux received at aphelion is not sufficient to propagate preexistent cracks due to the large distance from the Sun. At perihelion,

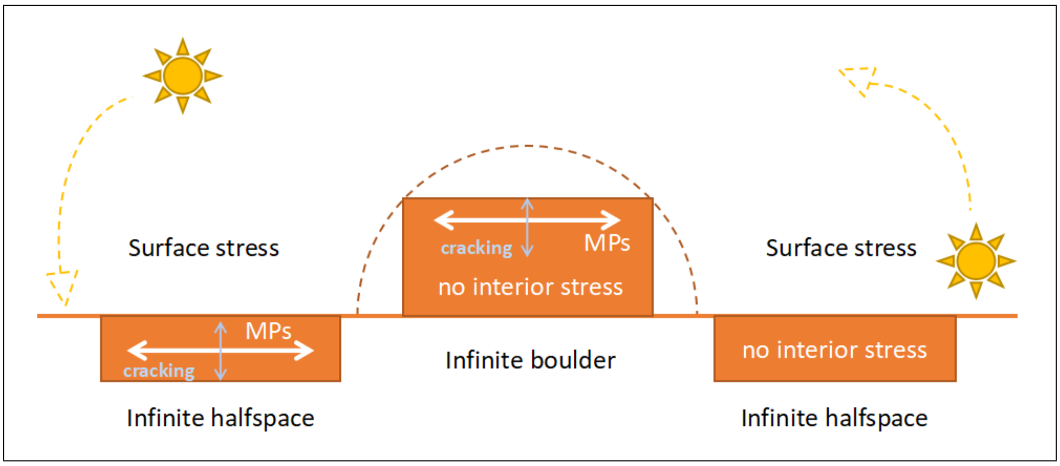

Figure 5.17: Surface and interior stresses in an infinite boulder and infinite halfspace. White arrows denote the orientation of the Maximum Principal Stress, and gray arrows denote the direction of crack propagation.

on the contrary, the surface of the boulder experiences a strong variation in temperature, and this contributes to the propagation of microcracks and weakening of the boulder.

5.5 Future Works

The upper layer of comet 67P reveals a uniform surface covered by regolith composed of elements ranging in size from centimeters up to 5 meters. The thickness of this layer varies from 0 to 2 meters (Mottola et al., 2015). The heat capacity of the regolith is strongly temperature dependent and for this reason we expect that boulders cool slowly if surrounded by warm insulating regolith. In the future, we will model temperature and stresses including a regolith layer with variable thickness to understand the rule of this layer in terms of thermal conduction and cracks propagation.
One of the major limit of this study is the composition of the boulder. Hypothesis about the mixture of materials can be made, but several models including different materials with variable thermal and physical properties are necessary. For doing this, we will apply the Cheng and Vachon theory to calculate the thermal conductivity of two- and three-phase solid heterogeneous mixtures (Cheng and Vachon, 1969). Thermal conductivity is defined as the rate at which heat is transferred by conduction through a unit-cross section area of a material, when a temperature gradient exists perpendicular to the area. We will adapt the model to calculate the appropriate thermal

conductivity of the boulder with different mixtures, comparing the result with the thermal conductivity of the comet measured by MIRO. This will allow to speculate about the composition of the comet's nucleus. We will consider two different models. The first defines a boulder as consisting of ice mixed with solid and cometary materials in the form of dust and agglomerated particulates. In the second model we will describe a boulder in which the icy part sublimated, leaving a porous boulder composed of solid and cometary material with residual gases confined in the porous structure. The porosity and the phase volume fraction, i.e. the ratio between the continuous and the discontinuous phases, will be modified to investigate their role in heat conduction. Finally, we will perform simulations over the entire orbit of the comet to include in our study the thermal fatigue, and to determine the number of orbits necessary for the fragmentation of the surface.

Chapter 6

Conclusions

Until the sixteenth century, comets were considered to be omens of death of kings and noble men. They were interpreted also as coming catastrophes or attacks against terrestrial inhabitants. Before 1600, it was not clear whether these objects were astronomical or meteorological phenomena in the atmosphere of the Earth. Today, comets are considered leftovers from the material that initially formed the Solar System. Travelling almost undisturbed from the time of their formation, they keep within them secrets about the origin of the Solar System and its evolution. They are made of primordial ice and dust, with generally unstable orbits, and interacting with the solar radiation. Early space missions to comet 21P/Giacobini-Zimmer in 1985, and 1P/Halley in 1986, provided the first in situ observation of comets, revealing their complexity and the need to study them in detail. The European Space Agency's Rosetta mission was the first designed to orbit and land on a comet. The spacecraft was launched on 2 March 2004, on a 10-year journey towards comet 67P/Churyumov-Gerasimenko. Rosetta flew by two main belt asteroids, 2867 Steins (in 2008) and 21 Lutetia (in 2010), before entering deep-space hibernation mode in June, 2011. On 12 November, 2014, Rosetta deployed the Philae probe to the comet for the first time in history. During the next phase of the mission, Rosetta accompanied the comet through perihelion (13 August, 2015), and concluded on 30 September, 2016, with a controlled impact onto the surface. The objectives of the Rosetta mission were to rendezvous with and enter orbit around comet 67P/Churyumov-Gerasimenko, and to perform observations of the comet's nucleus and coma while the comet moved along its orbit. The spacecraft and the lander were equipped with several remote sensing and in situ instruments, which allowed to study the physical and chemical properties of the nucleus, the evolution of the coma and of the nucleus during its orbit around the Sun, and link the morphological features present on the nucleus surface with the interac-

tion with the solar influence. The nucleus, its composition, morphology and activity, have been observed by the Optical, Spectroscopic and Infrared Remote Imaging System (OSIRIS) onboard Rosetta spacecraft. It consisted of a Narrow and a Wide Angle Cameras. High-resolution images reveal that the nucleus is a collection of morphological contrasts, characterized by different terrains and different striking types of landforms, such as smooth flat regolith plains, vertical cliffs, and talus aprons. The presence of large boulders is one of the most important geological features of 67P. These objects can be found ubiquitously on the surface, both isolated and in clusters, and their size distribution depends both on the formation and evolution they have undergone. In this work we focused on boulders because their presence on comet 67P offers the opportunity to study the physical properties and the evolution of the comet itself. They reveal imprints of erosional and geological processes that affected the surface of the nucleus, allowing to study all the phenomena which lead to the fragmentation of the surface. Thermal stresses, gravitational phenomena, and comet activity are considered the best candidates.
This work has been divided into three parts. In the first part, we have proposed a detailed quantitative analysis of isolated boulder fields that are located in three different regions of comet 67P. This analysis has taken into account the size-frequency distribution and cumulative fractional area of 11811 boulders. We have investigated the validity of the theory according to which the power-law exponent of the size-frequency distribution can be interpreted as the fractal dimension of the population. We have finally analyzed the shape of these boulders, finding a suitable set of shape parameters useful to describe their morphology. Our results show that there are significant differences between the studied regions. The size-frequency distributions of Imhotep, Hapi, and Hatmehit populations reveal that the first two regions are characterized by a similar power index, in the range of -2.3/-2.7. The Hapi area shows a different value of the power index. This might indicate different formation processes of the boulders. We have also found that the distribution of boulders does not show significant variations with respect to the perihelion passage, in agreement with what is found in literature. We tested the relationship between the size-frequency distribution and the fractal theory by applying the box-count approach to investigate the fractal behavior of the population. The calculated fractal dimension indicates that all studied areas show a possible fractal behavior, except for the bigger boulders on Hapi. These difference might suggest a different origin of these boulders. To explain this result, we have suggested two different solutions: the first suggests that the boulders located in Hapi collapsed during past gravitational events and their fragmentation is the result of an ongoing thermal weathering. The second one proposes a different scenario. Due to the location and

peculiar alignment of these boulders, these objects would represent the tops of outcrops, immersed in a deposit of back-fall material. This is consistent with the presence of layers, because the boulders appear to be aligned along a specific layer of the big lobe. Finally, we have defined solidity and circularity as invariant shape factors. These quantities are fundamental to describe the boulder morphology across the different populations. All the analyzed boulders show a rounded and solid shape without many inlets. We have compared the mean values of the shape parameters before and after perihelion, and we have not observed significant differences among the analyzed regions. In the second part of this work, we have quantified the seasonal erosion and deposit/accretion in the Hapi region. Due to the inclination of the spin axis, the southern hemisphere of comet 67P experiences a strong insolation during perihelion. This results in an insolation dicothomy between the northern and southern hemisphere, which is reflected also in the morphology between the two hemispheres. Northern regions are fully covered of dust. On the contrary, equatorial regions are characterized by consolidated and coarse terrains. During the approach to perihelion, the temperature of the nucleus surface increases, causing the sublimation of ices. Water has been defined as the most abundant volatile in the coma, suggesting a strong erosion of the surface due to the sublimation of water ice. The strong insolation in the south and the water ice content could erode the surface up to 20 m around perihelion. The northern hemisphere has shown a minimal erosion due to the minimal amount of received insolation. For this reason, the presence of dust in the northern region has been suggested to be the result of transport mechanisms of particles from the southern hemisphere during the southern summer. The amount of dust transported from south to north can shed light on the content of 67P's pristine ice, assuming that the value can be representative of the average value of all comets. To provide an upper limit of comet's water ice fraction, we have developed a tool which allowed to quantify the seasonal erosion and deposit/accretion in the Hapi region. We have monitored the time evolution of 22 boulders heights with a vertical accuracy of 0.2 m, defined as the difference between the top of the boulders and the surrounding pebble deposit surfaces. We have found a decrease of the boulder heights at the perihelion phase from 2014 to 2016 of $\delta\Delta_{2014-2016}$ = -1.4 ± 0.4 m. This value has been thus interpreted as a direct measurement of the fallout thickness. The predicted (Fulle et al., 2018b) fallout thickness of 1.8 ± 0.7 m is consistent with our results. The comparison between the thickness of the eroded layer and the dust density found in the coma in the same period, leads to the Hapi's fallout of about 96%. This provides an upper limit of 2% in mass for Hapi's water ice fraction, which fixes the pristine 67P ice content in the range from 1% to 15% in mass. Following the model developed by

Fulle et al. (2018b), considering all the possible ice losses during the transfer of the fallout from the southern sources onto Hapi, the water ice fraction in Hapi's deposit of (1.2 ± 0.8)% provides refractory-to-ice mass ratios ranging from 6 to 110 in the perihelion-eroded volume of pristine nucleus material of 4×10^7 m^3, corresponding to the 67P pristine ice mass fraction of (8 ± 7)%. Comparing this value with other components, it is evident that is a bit lower than the range from 5% (Mogi et al., 2017) to 20% (Garenne et al., 2014) measured in CI-chondrites and in the InterStellar Medium (about 20%).
Finally, we have investigated how thermal weathering influenced the propagation of preexisting cracks on boulders of comet 67P. Thermal shock and fatigue are considered as the most important processes responsible for the fragmentation of the nucleus surface. There are two different stresses that can contribute to the erosion of a boulder. The exterior stress is controlled by a sudden variation in temperature during sunset and sunrise, while interior stresses are controlled by the thermal gradient due to the day and night cycle. The aim was to explore which stress can affect the simulated boulder and explore whether the simulated stress is enough to propagate preexisting cracks. We have selected a specific boulder located in the Imhotep region because it shows elements attributable to thermal fragmentation: the surface of the boulder is highly fractured, and fractures are perpendicular with respect the path of the Sun. This aspect is fundamental because the orientation of cracks can provide insight of how thermal stresses act. The boulder is surrounded by smaller fragments, and this population is unrelated to specific gravitational deposits. Following the method developed by Keller et al. (2015), we have calculated the incident heat flux during aphelion and perihelion. The results have been used as boundary conditions for our thermal and stress model. We used COMSOL Multyphysics to simulate the propagation of heat inside a 40 m boulder, model the surface and interior temperature, and the Maximum Principal Stress. We have selected this crack propagation theory because this stress controls the plane in which the direction of crack propagation occurs. Our preliminary results show that the sudden variation in temperature after the sunset and sunrise produces high surface stresses regardless of thermal gradient between the interior and the surface of the boulder. No interior stress is present, and the strong flux of heat outside the boulder induces a local thermal gradient in the subsurface, contributing to surface stresses. The reason is that the surface of a large boulder approaches that of infinite halfspace, and cannot experience internal stresses during daytime. Infinite rocks can have tensile stress at the depth as the thermal wave travel downward, but have the same effects as surface stresses. We have finally applied the Linear Elastic Fracture Mechanics theory to understand whether the simulated stress was sufficient to propagate cracks. The heat

flux received at aphelion is not sufficient to propagate preexistent cracks due to the large distance from the Sun. At perihelion, on the contrary, the surface of the boulder experiences a strong variation in temperature, and this contributes to the propagation of microcracks and weakening of the boulder.

Appendix A

Annexes of Chapter 4

NAC-OSIRIS image	Spatial scale (m/pixel)
NAC_2014-08-21T16.42.56.549Z_ID30_1397549300_F22	1.26
NAC_2014-08-21T19.42.54.558Z_ID30_1397549900_F22	1.25
NAC_2014-08-21T20.42.54.581Z_ID30_1397549100_F22	1.25
NAC_2014-08-22T08.42.54.550Z_ID30_1397549000_F22	1.26
NAC_2014-08-28T20.42.53.590Z_ID30_1397549900_F22	1.01
NAC_2014-08-29T14.42.55.551Z_ID30_1397549700_F22	1.02
NAC_2014-08-29T20.42.53.538Z_ID30_1397549900_F22	1.02
NAC_2014-08-29T21.42.53.565Z_ID30_1397549100_F22	0.99
NAC_2014-08-29T23.12.53.524Z_ID30_1397549500_F22	1.01
NAC_2014-08-30T02.42.53.544Z_ID30_1397549800_F22	1.04
NAC_2014-08-30T03.42.53.546Z_ID30_1397549000_F22	1.05
NAC_2014-08-31T15.42.53.546Z_ID30_1397549000_F22	1.24
NAC_2014-09-01T16.42.53.551Z_ID30_1397549400_F22	0.97
NAC_2014-09-10T11.54.24.601Z_ID30_1397549000_F24	0.55
NAC_2014-09-22T21.09.48.386Z_ID30_1397549000_F16	0.54
NAC_2014-12-10T06.29.11.447Z_ID30_1397549002_F24	0.37
NAC_2016-06-19T11.09.40.836Z_ID30_1397549000_F41	0.56
NAC_2016-06-19T15.30.03.468Z_ID30_1397549004_F16	0.54
NAC_2016-09-30T03.37.09.738Z_ID30_1397549200_F22	0.26

Table A.1: The NAC-OSIRIS images used in this work. The first three letters indicate the instrument used to acquire the image; the following digits are the time (in Coordinate Universal Time, UTC) of imaging (year-month-day, then hour-minute-seconds) as reported in the file name (this time is not corrected for S/C drift and leap seconds); the last two numbers correspond to the used filter identifier. The spatial scale (m/pixel) is shown.

ID Boulder	Latitude (°)	Longitude (°)
1	27.69	18.20
2	30.76	22.61
3	30.25	30.35
4	33.82	31.72
5	33.39	27.18
6	36.58	20.36
7	38.93	22.81
8	40.52	25.49
9	36.86	9.64
10	36.09	7.92
11	39.50	12.15
12	39.71	7.98
13	50.93	354.56
14	55.09	345.15
15	49.93	0.03
16	56.05	2.95
17	59.19	6.85
18	47.03	357.43
19	51.33	0.60
20	47.92	4.99
21	44.89	5.62
22	31.06	25.07

Table A.2: ID, latitude, and longitude of the analyzed boulders.

Boulder	Image	UTC	Subset	i	e	L	H	δH
				(°)	(°)	(m)	(m)	(m)
1	21/08/2014	16:42:56	1	80.5	55.3	50.0	8.4	0.8
	22/08/2014	8:42:50	1	44.1	36.2	8.3	8.6	1.9
	29/08/2014	20:42:53	2	83.9	47.1	86.1	9.1	0.9
	29/08/2014	21:42:53	2	70.5	31.7	25.7	9.1	0.8
	29/08/2014	23:12:53	2	72.4	34.3	28.8	9.1	0.8
	30/08/2014	2:42:53	2	42.4	11.5	8.3	9.1	1.5
	30/08/2014	3:42:53	2	35.3	10.2	6.8	9.6	1.8
	10/9/2014	11:54:24	3	50.9	41.7	12.1	9.8	1.1
	22/09/2014	21:09:48	3	40.3	56.3	8.1	9.5	2.1
	19/06/2016	11:09::40	5	61.5	26.5	15.1	8.2	0.7
2	22/08/2014	8:42:50	1	40.7	26.8	9.0	10.5	1.9
	29/08/2014	21:42:53	2	70.8	32.2	32.1	11.2	0.8
	29/08/2014	23:12:53	2	65.9	29.0	24.6	11.1	0.9
	1/9/2014	16:42:53	2	36.9	26.3	8.3	11.1	1.9
	10/9/2014	11:54:24	3	45.5	56.3	11.9	11.7	1.8
	22/09/2014	21:09:48	3	45.0	63.1	11.5	11.5	2.1
	10/12/2014	6:29:11	4	79.0	14.6	62.3	12.1	0.7
	19/06/2016	11:09::40	5	59.8	27.5	18.9	11.1	0.8
3	21/08/2014	19:42:54	1	46.7	19.1	6.4	6.0	1.5
	28/08/2014	20:42:53	2	73.8	46.3	22.4	6.5	0.7
	29/08/2014	20:42:53	2	70.6	33.9	18.5	6.5	0.7
	29/08/2014	21:42:53	2	76.0	37.1	27.9	6.9	0.7
	29/08/2014	23:12:53	2	74.7	37.4	23.7	6.5	0.7
	30/08/2014	2:42:53	2	45.7	33.5	7.2	7.0	1.6
	30/08/2014	3:42:53	2	30.9	15.9	4.2	7.0	2.2
	31/08/2014	15:42:53	2	45.1	12.1	7.4	7.4	1.5
	1/9/2014	16:42:53	2	41.0	20.7	6.5	7.5	1.5
	10/9/2014	11:54:24	3	40.6	56.1	6.0	7.0	2.0
	22/09/2014	21:09:48	3	37.4	58.8	5.7	7.5	2.3
	10/12/2014	6:29:11	4	77.0	14.2	33.3	7.7	0.7
	19/06/2016	11:09:40	5	57.1	30.1	9.7	6.3	0.8
4	21/08/2014	19:42:54	1	24.4	19.6	5.9	13.0	3.6
	22/08/2014	8:42:50	1	51.3	33.0	16.5	13.2	1.5
	28/08/2014	20:42:53	2	66.7	43.4	31.8	13.7	1.1
	29/08/2014	20:42:53	2	77.1	38.4	61.5	14.1	0.9
	29/08/2014	21:42:53	2	64.1	25.4	29.0	14.1	1.0
	29/08/2014	23:12:53	2	60.6	23.5	24.1	13.6	1.0
	31/08/2014	15:42:53	2	43.4	10.3	13.3	14.1	1.7

Boulder	Image	UTC	Subset	i	e	L	H	δH
				(°)	(°)	(m)	(m)	(m)
	10/9/2014	11:54:24	3	47.4	51.0	15.6	14.3	1.5
	10/12/2014	6:29:11	4	75.5	15.6	57.4	14.8	0.7
	19/06/2016	11:09:40	5	60.1	28.6	23.4	13.5	0.8
5	21/08/2014	19:42:54	1	43.9	25.3	10.1	10.5	1.8
	22/08/2014	8:42:50	1	45.7	30.7	11.0	10.8	1.7
	28/08/2014	20:42:53	2	68.4	45.8	28.8	11.4	1.0
	29/08/2014	20:42:53	2	69.5	31.3	29.7	11.1	0.8
	29/08/2014	21:42:53	2	67.2	28.5	26.6	11.2	0.9
	29/08/2014	23:12:53	2	76.4	38.4	45.6	11.0	0.8
	30/08/2014	2:42:53	2	44.6	21.2	11.3	11.4	1.5
	31/08/2014	15:42:53	2	42.6	10.8	10.8	11.8	1.7
	1/9/2014	16:42:53	2	43.0	33.6	11.1	11.9	1.7
	10/9/2014	11:54:24	3	44.1	52.8	11.5	11.9	1.7
	10/12/2014	6:29:11	3	81.1	14.3	78.6	12.4	0.8
	19/06/2016	11:09:40	5	57.0	30.1	17.6	11.4	0.8
6	21/08/2014	16:42:56	1	65.6	49.2	62.0	28.1	1.6
	21/08/2014	19:42:54	1	55.2	30.3	40.0	27.8	1.7
	22/08/2014	8:42:50	1	49.3	37.5	32.5	28.0	2.0
	29/08/2014	20:42:53	2	59.5	22.4	48.8	28.7	1.3
	29/08/2014	21:42:53	2	68.6	30.0	73.2	28.7	1.3
	29/08/2014	23:12:53	2	66.5	27.3	65.8	28.7	1.3
	30/08/2014	2:42:53	2	48.9	11.2	32.6	28.4	1.5
	30/08/2014	3:42:53	2	39.4	15.5	23.4	28.4	2.0
	31/08/2014	15:42:53	2	49.6	4.9	33.4	28.4	1.6
	1/9/2014	16:42:53	2	48.5	37.7	32.8	29.0	1.8
	10/9/2014	11:54:24	3	58.4	41.4	48.3	29.7	1.3
	22/09/2014	21:09:48	3	55.4	53.7	41.3	28.5	1.6
	19/06/2016	11:09:40	5	62.3	26.8	52.8	27.7	1.1
7	21/08/2014	19:42:54	1	49.4	26.7	18.2	15.6	1.7
	29/08/2014	20:42:53	2	77.1	39.4	71.7	16.4	1.0
	29/08/2014	21:42:53	2	69.8	30.9	43.8	16.1	1.0
	29/08/2014	23:12:53	2	40.0	18.6	13.5	16.1	1.8
	10/9/2014	11:54:24	3	44.9	45.7	16.9	17.0	1.6
	22/09/2014	21:09:48	3	48.1	46.5	18.5	16.6	1.4
	10/12/2014	6:29:11	4	68.9	22.9	44.9	17.3	0.7
	19/06/2016	11:09:40	5	66.5	25.1	36.6	15.9	0.8
8	29/08/2014	20:42:53	2	75.5	37.0	21.7	5.6	0.6
	29/08/2014	21:42:53	2	59.9	20.9	10.3	6.0	0.9

Boulder	Image	UTC	Subset	i	e	L	H	δH
				(°)	(°)	(m)	(m)	(m)
	30/08/2014	2:42:53	2	49.8	23.4	6.9	5.8	1.2
	10/9/2014	11:54:24	3	49.6	40.2	7.8	6.6	1.1
	22/09/2014	21:09:48	3	52.7	34.4	8.0	6.1	0.9
	10/12/2014	6:29:11	4	61.0	32.7	12.3	6.8	0.6
	19/06/2016	11:09:40	5	62.8	25.7	11.3	5.8	0.6
	30/09/2016	3:37:09	6	86.0	62.2	83.0	5.8	0.8
9	29/08/2014	21:42:53	2	65.8	28.6	24.9	11.2	0.9
	29/08/2014	23:12:53	2	72.2	32.8	35.6	11.4	0.8
	10/9/2014	11:54:24	3	50.0	47.2	14.3	12.0	1.3
	22/09/2014	21:09:48	3	57.6	57.3	18.7	11.9	1.3
10	29/08/2014	14:42:55	2	54.4	43.9	6.1	4.4	1.3
	29/08/2014	21:42:53	2	62.9	28.6	7.7	3.9	0.8
	29/08/2014	23:12:53	2	67.7	30.2	9.6	3.9	0.7
	30/08/2014	2:42:53	2	53.0	24.7	5.9	4.5	1.1
	30/08/2014	3:42:53	2	49.0	22.0	4.5	3.9	1.2
	31/08/2014	15:42:53	2	56.6	5.6	6.5	4.3	0.9
	1/9/2014	16:42:53	2	53.8	39.6	6.0	4.4	1.2
	10/9/2014	11:54:24	3	60.1	45.4	8.4	4.8	0.8
	22/09/2014	21:09:48	3	51.9	51.8	5.8	4.5	1.2
	19/06/2016	11:09:40	5	74.6	29.3	12.0	3.3	0.4
11	21/08/2014	19:42:54	1	62.7	42.2	57.1	29.5	1.6
	21/08/2014	20:42:54	1	56.6	34.6	45.3	29.8	1.7
	22/08/2014	8:42:50	1	59.4	51.0	50.7	30.0	1.8
	29/08/2014	14:42:55	2	58.4	34.7	49.1	30.2	1.5
	29/08/2014	20:42:53	2	50.5	12.0	37.8	31.2	1.5
	29/08/2014	21:42:53	2	61.2	23.2	55.6	30.6	1.4
	30/08/2014	2:42:53	2	60.2	21.3	53.2	30.5	1.4
	31/08/2014	15:42:53	2	59.4	18.2	50.6	30.0	1.5
	1/9/2014	16:42:53	2	57.5	49.6	47.9	30.5	1.7
	22/09/2014	21:09:48	3	59.2	43.5	52.1	31.0	1.3
	10/12/2014	6:29:11	4	65.5	26.1	69.2	31.5	1.1
12	21/08/2014	19:42:54	1	66.7	47.4	40.1	17.2	1.3
	21/08/2014	20:42:54	1	62.0	37.0	32.0	17.0	1.3
	22/08/2014	8:42:50	1	66.0	54.9	39.1	17.4	1.4
	29/08/2014	14:42:55	2	60.9	39.4	32.4	18.0	1.2
	29/08/2014	23:12:53	2	62.9	26.3	34.9	17.8	1.1
	30/08/2014	2:42:53	2	61.1	22.7	32.2	17.7	1.1
	30/08/2014	3:42:53	2	55.3	24.2	26.1	18.1	1.3

Boulder	Image	UTC	Subset	i	e	L	H	δH
				(°)	(°)	(m)	(m)	(m)
	31/08/2014	15:42:53	2	60.6	20.0	32.2	18.1	1.2
	1/9/2014	16:42:53	2	59.8	50.4	31.1	18.1	1.4
	22/09/2014	21:09:48	3	62.4	41.6	35.4	18.5	1.0
13	21/08/2014	16:42:56	1	71.9	54.2	52.0	17.0	1.2
	21/08/2014	20:42:54	1	64.1	42.0	35.0	17.0	1.3
	22/08/2014	8:42:50	1	66.7	57.8	39.0	16.8	1.4
	29/08/2014	14:42:55	2	65.6	34.5	37.6	17.0	1.1
	29/08/2014	20:42:53	2	35.2	13.0	12.1	17.1	2.0
	29/08/2014	23:12:53	2	66.6	13.0	39.9	17.2	1.1
	30/08/2014	2:42:53	2	66.4	26.7	41.3	18.1	1.0
	30/08/2014	3:42:53	2	60.0	24.1	31.5	18.2	1.2
	31/08/2014	15:42:53	2	67.3	25.4	43.1	18.0	1.1
	1/9/2014	16:42:53	2	64.9	55.8	37.7	17.6	1.3
	22/09/2014	21:09:48	3	67.1	38.1	42.9	18.1	0.9
	19/06/2016	11:09:40	5	79.3	30.4	90.0	17.0	1.0
14	21/08/2014	19:42:54	1	69.8	51.9	47.5	17.5	1.3
	21/08/2014	20:42:54	1	65.2	41.3	37.9	17.5	1.3
	22/08/2014	8:42:50	1	76.9	68.0	74.5	17.4	1.4
	28/08/2014	20:42:53	2	45.7	19.3	18.5	18.1	1.5
	29/08/2014	14:42:55	2	66.6	41.8	40.8	17.6	1.1
	29/08/2014	20:42:53	2	35.3	7.8	12.8	18.1	1.9
	29/08/2014	21:42:53	2	42.2	15.0	16.4	18.1	1.6
	29/08/2014	23:12:53	2	62.2	13.6	34.5	18.2	1.1
	30/08/2014	2:42:53	2	67.4	28.2	43.8	18.2	1.0
	30/08/2014	3:42:53	2	64.7	28.3	38.8	18.3	1.1
	31/08/2014	15:42:53	2	69.9	26.8	50.6	18.5	1.1
	1/9/2014	16:42:53	2	67.9	56.7	46.7	19.0	1.3
	22/09/2014	21:09:48	3	71.2	38.7	55.1	18.7	0.9
	10/12/2014	6:29:11	4	53.1	39.9	25.6	19.2	1.1
	19/06/2016	15:30:03	5	69.3	16.6	47.2	17.8	0.8
	30/09/2016	3:37:09	6	65.4	42.9	38.1	17.4	0.8
15	29/08/2014	14:42:55	2	54.9	34.5	31.3	22.0	1.4
	29/08/2014	23:12:53	2	64.9	32.4	59.1	21.6	1.1
	30/08/2014	2:42:53	2	62.0	25.7	41.4	22.1	1.2
	30/08/2014	3:42:53	2	56.3	21.1	32.1	21.4	1.3
	31/08/2014	15:42:53	2	65.6	19.8	47.2	21.4	1.2
	1/9/2014	16:42:53	2	64.8	54.0	46.8	22.0	1.4
	22/09/2014	21:09:48	3	71.8	43.6	67.7	22.3	1.0

Boulder	Image	UTC	Subset	i	e	L	H	δH
				(°)	(°)	(m)	(m)	(m)
	30/09/2016	3:37:09	6	69.8	44.3	42.6	20.0	0.9
16	21/08/2014	19:42:54	1	58.4	44.0	28.3	17.4	1.5
	21/08/2014	20:42:54	1	52.7	37.5	22.8	17.3	1.7
	22/08/2014	8:42:50	1	71.3	65.9	51.0	17.3	1.4
	29/08/2014	14:42:55	2	55.1	28.3	25.3	17.6	1.3
	29/08/2014	20:42:53	2	50.4	13.2	21.8	18.0	1.3
	29/08/2014	21:42:53	2	55.5	19.3	26.3	18.1	1.2
	29/08/2014	23:12:53	2	53.4	14.9	23.9	17.7	1.2
	30/08/2014	2:42:53	2	57.7	16.8	29.1	18.4	1.2
	30/08/2014	3:42:53	2	52.7	11.5	24	18.3	1.2
	31/08/2014	15:42:53	2	59.4	25.4	31.1	18.4	1.3
	1/9/2014	16:42:53	2	57.7	53.1	28.8	18.2	1.6
	22/09/2014	21:09:48	3	60.3	35.2	32.6	18.6	1.0
	10/12/2014	6:29:11	4	68.2	24.8	47.8	19.1	0.8
	19/06/2016	11:09:40	5	79.4	20.9	93.0	17.4	1.0
	19/06/2016	15:30:03	5	73.4	13.1	59.2	17.6	0.8
	30/09/2016	3:37:09	6	70.3	50.0	49.3	17.7	0.9
17	21/08/2014	20:42:54	1	57.1	38.8	16.2	10.5	1.4
	29/08/2014	20:42:53	2	41.4	2.7	10.0	11.3	1.4
	29/08/2014	21:42:53	2	47.1	8.6	11.9	11.1	1.2
	30/08/2014	2:42:53	2	64.2	23.4	23.0	11.1	0.9
	30/08/2014	3:42:53	2	56.2	16.4	16.8	11.2	1.1
	31/08/2014	15:42:53	2	56.7	21.6	17.3	11.4	1.2
	22/09/2014	21:09:48	3	64.0	40.3	24.2	11.8	0.8
	10/12/2014	6:29:11	4	49.9	43.1	14.6	12.3	1.1
	19/06/2016	11:09:40	5	78.0	23.1	51.0	10.8	0.7
	19/06/2016	15:30:03	5	70.8	15.5	29.7	10.4	0.6
	30/09/2016	3:37:09	6	62.0	40.0	19.9	10.6	0.7
18	21/08/2014	19:42:54	1	75.7	50.6	14.3	3.6	0.7
	22/08/2014	8:42:50	1	67.8	55.0	13.5	5.5	1.0
	29/08/2014	14:42:55	2	63.0	37.5	11.4	5.8	0.9
	29/08/2014	20:42:53	2	45.8	8.2	5.3	5.2	1.2
	29/08/2014	21:42:53	2	61.0	27.6	10.5	5.8	0.9
	29/08/2014	23:12:53	2	72.8	35.4	13.1	4.1	0.6
	30/08/2014	2:42:53	2	66.9	27.9	10.2	4.3	0.7
	30/08/2014	3:42:53	2	67.7	29.5	12.5	5.1	0.7
	31/08/2014	15:42:53	2	71.9	24.6	19.1	6.2	0.7
	1/9/2014	16:42:53	2	68.0	54.3	12.9	5.2	0.9

Boulder	Image	UTC	Subset	i	e	L	H	δH
				(°)	(°)	(m)	(m)	(m)
	22/09/2014	21:09:48	3	75.7	44.9	22.1	5.6	0.5
	10/12/2014	6:29:11	4	65.3	27.8	13.3	6.2	0.5
	19/06/2016	15:30:03	5	74.3	12.7	16.0	4.5	0.4
	30/09/2016	3:37:09	6	68.5	50.4	11.2	4.4	0.6
19	29/08/2014	14:42:55	2	57.0	28.7	17.0	11.1	1.1
	29/08/2014	23:12:53	2	53.8	14.7	14.5	10.6	1.1
	30/08/2014	2:42:53	2	60.5	24.6	18.0	10.2	1.0
	30/08/2014	3:42:53	2	65.0	24.1	21.8	10.2	0.9
	31/08/2014	15:42:53	2	63.6	36.2	21.1	10.5	1.1
	22/09/2014	21:09:48	3	67.3	30.8	26.4	11.1	0.7
	10/12/2014	6:29:11	4	59.4	32.7	19.6	11.6	0.7
	19/06/2016	11:09:40	5	78.9	19.3	51.0	10.0	0.6
	19/06/2016	15:30:03	5	75.5	17.6	36.3	9.4	0.5
	30/09/2016	3:37:09	6	70.3	40.7	27.5	9.9	0.6
20	21/08/2014	20:42:54	1	60.6	29.6	9.3	5.2	1.0
	22/08/2014	8:42:50	1	66.6	48.3	12.8	5.5	1.0
	29/08/2014	23:12:53	2	73.5	35.2	20.6	6.1	0.6
	31/08/2014	15:42:53	2	60.5	15.4	11.5	6.5	0.9
	1/9/2014	16:42:53	2	65.4	48.0	13.1	6.0	0.9
21	21/08/2014	20:42:54	1	68.1	38.7	20.2	8.1	0.9
	22/08/2014	8:42:50	1	65.9	47.0	18.1	8.1	1.0
	29/08/2014	21:42:53	2	54.6	16.4	12.2	8.7	1.0
	1/9/2014	16:42:53	2	54.6	41.9	12.6	8.9	1.3
	10/12/2014	6:29:11	4	46.2	45.8	10.0	9.6	1.2
	30/09/2016	3:37:09	6	76.7	52.4	33.7	8.0	0.6
22	28/08/2014	20:42:53	2	72.9	45.7	11.4	3.5	0.6
	29/08/2014	21:42:53	2	73.1	34.8	11.2	3.4	0.6
	29/08/2014	23:12:53	2	74.6	36.6	12.2	3.4	0.5
	30/08/2014	2:42:53	2	44.0	25.7	3.3	3.4	1.5
	1/9/2014	16:42:53	2	37.1	31.6	3.0	4.0	1.9
	10/9/2014	11:54:24	3	45.0	51.9	4.0	4.0	1.5
	22/09/2014	21:09:48	3	51.3	57.3	5.1	4.1	1.4

Table A.3: Summary of the boulder height measurements, reporting (for each boulder) the date of the image on which the height is calculated, the corresponding UTC as reported in the file name (this time is not corrected for S/C drift and leap seconds), the corresponding subset, the incidence angle (i), the emission angle (e), the measured length of the shadow (L), the measured height of boulder (H) with the associated average error bar (δH).

Boulder	S1 $< H >$ (m)	S1 $\delta(< H >)$ (m)	S2 $< H >$ (m)	S2 $\delta(< H >)$ (m)	S3 $< H >$ (m)	S3 $\delta(< H >)$ (m)	S4 $< H >$ (m)	S4 $\delta(< H >)$ (m)	S5 $< H >$ (m)	S5 $\delta(< H >)$ (m)	S6 $< H >$ (m)	S6 $\delta(< H >)$ (m)
1	8.4	0.5	9.1	0.4	9.8	0.43			8.2	1.5		
2	10.5	0.5	11.1	0.4	11.6	0.4	12.1	1.5	11.1	1.3		
3	6	0.7	6.7	0.3	7.2	0.3	7.7	1.4	6.3	1.3		
4	13.2	0.3	13.9	0.4	14.3	0.7	14.8	1.5	13.5	1.2		
5	10.6	0.4	11.3	0.3	11.8	0.6	12.4	1.3	11.4	1.2		
6	27.9	0.3	28.6	0.2	29.2	0.5			27.7	0.9		
7	15.6	0.6	16.2	0.4	16.8	0.5	17.3	1.4	15.9	1.3		
8			5.8	0.2	6.3	0.3	6.8	0.2	5.8	1.7	5.7	1.2
9			11.3	0.8	11.9	0.6						
10			4.1	0.4	4.7	0.7			3.3	2.7		
11	29.8	0.3	30.5	0.3	31.1	0.8	31.5	1.0				
12	17.2	0.4	18.0	0.3	18.5	1.0						
13	16.9	0.4	17.7	0.3	18.1	1.1			16.9	1.0		
14	17.5	0.5	18.2	0.3	18.7	1.1	19.2	0.9	17.8	1.3	17.4	1.2
15			21.7	0.3	22.3	1.0					20.1	1.1
16	17.4	0.4	18.1	0.3	18.6	1.0	19.1	1.3	17.6	0.8	17.7	1.1
17	10.5	0.7	11.2	0.4	11.8	1.2	12.3	0.9	10.6	1.2	10.6	1.5
18	4.2	0.8	5.1	0.4	5.6	1.9	6.1	2.1	4.5	2.9	4.4	1.8
19			10.4	0.3	11.1	1.5	11.6	1.4	9.7	1.7	9.7	1.7
20	5.4	0.7	6.2	0.7								
21	8.1	0.7	8.8	0.6			9.6	0.8			8	1.7
22			3.4	0.4	4.1	0.5						

Table A.4: Time evolution of the weighted average height of each boulder. Each subset (S) contains the weighted average height ($< H >$) of each boulder and the associated error ($\delta(< H >)$).

Boulder	S2-S1 Δ (m)	S2-S1 $\delta\Delta$ (m)	S3-S2 Δ (m)	S3-S2 $\delta\Delta$ (m)	S4-S3 Δ (m)	S4-S3 $\delta\Delta$ (m)	S5-S4 Δ (m)	S5-S4 $\delta\Delta$ (m)	S6-S5 Δ (m)	S6-S5 $\delta\Delta$ (m)
1	0.7	0.6	0.6	0.6						
2	0.6	0.7	0.5	0.6	0.5	1.5	-1.1	2.0		
3	0.7	0.7	0.5	0.4	0.5	1.5	-1.4	2.0		
4	0.7	0.5	0.4	0.8	0.5	1.6	-1.3	1.9		
5	0.6	0.5	0.6	0.8	0.5	1.4	-0.9	1.7		
6	0.7	0.4	0.6	0.6						
7	0.7	0.8	0.5	0.7	0.5	1.5	-1.4	1.9		
8			0.5	0.3	0.5	0.4	-1.0	1.7	-0.2	2.2
9			0.6	1.0						
10			0.6	0.8						
11	0.7	0.4	0.6	0.8	0.5	1.2				
12	0.7	0.6	0.5	1.1						
13	0.7	0.5	0.5	1.2						
14	0.8	0.5	0.5	1.1	0.5	1.4	-1.4	1.6	-0.4	1.8
15			0.6	1.0						
16	0.8	0.5	0.5	1.1	0.5	1.7	-1.6	1.5	0.2	1.4
17	0.7	0.8	0.6	1.3	0.5	1.5	-1.6	1.5	0.1	1.9
18	0.9	0.9	0.5	2.0						
19			0.6	1.5	0.5	2.0	-1.8	1.9	0.2	2.1
20	0.8	1.0								
21	0.7	0.9								
22			0.6	0.6						
Weighted average	0.7	0.2	0.5	0.2	0.5	0.3	-1.3	0.5	-0.1	0.8

Table A.5: Time evolution of the boulder height difference $< \delta$. Each time step contains information related to 22 boulders. The height differences for each boulder and the weighted averages with the associated error bars are reported.

Bibliography

Allegre, C., Le Mouel, J., and Provost, A. (1982). Scaling rules in rock fracture and possible implications for earthquake prediction. *Nature*, 297(5861):47.

Altwegg, K., Balsiger, H., Berthelier, J., Bieler, A., Calmonte, U., Fuselier, S., Goesmann, F., Gasc, S., Gombosi, T. I., Le Roy, L., de Keyser, J., Morse, A., Rubin, M., Schuhmann, M., Taylor, M. G. G. T., Tzou, C.-Y., and Wright, I. (2017). Organics in comet 67P a first comparative analysis of mass spectra from ROSINADFMS, COSAC and Ptolemy. *Monthly Notices of the Royal Astronomical Society*, 469(Suppl˙2):S130–S141.

Anishetty, R., Koehler, P., and McLerran, L. (1980). Central collisions between heavy nuclei at extremely high energies: The fragmentation region. *Phys. Rev. D*, 22:2793–2804.

Åström, J. (2006). Statistical models of brittle fragmentation. *Advances in Physics*, 55(3-4):247–278.

Auger, A.-T., Groussin, O., Jorda, L., Bouley, S., Gaskell, R., Lamy, P. L., Capanna, C., Thomas, N., Pommerol, A., Sierks, H., et al. (2015). Geomorphology of the imhotep region on comet 67p/churyumov-gerasimenko from osiris observations. *Astronomy & Astrophysics*, 583:A35.

Auster, H. U., Apáthy, I., Berghofer, G., Fornacon, K., Remizov, A., Carr, C., Guettler, C., Haerendel, G., Heinisch, P., Hervcik, D., Hilchenbach, M., Kührt, E., Magnes, W., Motschmann, U., Richter, I., Russell, C. T., Przyklenk, A., Schwingenschuh, K., Sierks, H., and Glassmeier, K.-H. (2015). The nonmagnetic nucleus of comet 67p/churyumov-gerasimenko. *Science*, 349.

Auster, H. U., Apathy, I., Berghofer, G., Remizov, A., Roll, R., Fornacon, K. H., Glassmeier, K. H., Haerendel, G., Hejja, I., Kührt, E., Magnes, W., Moehlmann, D., Motschmann, U., Richter, I., Rosenbauer, H., Russell,

C. T., Rustenbach, J., Sauer, K., Schwingenschuh, K., Szemerey, I., and Waesch, R. (2007). Romap: Rosetta magnetometer and plasma monitor. *Space Science Reviews*, 128(1):221–240.

Ballan, L., Brusco, N., and Cortelazzo, G. M. (2005). 3D passive shape recovery from texture and silhouette information. In *2nd IEE European Conference on Visual Media Production, CVMP*, London, UK.

Balsiger, H., Altwegg, K., Bochsler, P., Eberhardt, P., Fischer, J., Graf, S., Jäckel, A., Kopp, E., Langer, U., Mildner, M., et al. (2007). Rosina–rosetta orbiter spectrometer for ion and neutral analysis. *Space Science Reviews*, 128(1-4):745–801.

Barbin, Y., Kofman, W., Nielsen, E., Hagfors, T., Seu, R., Picardi, G., and Svedhem, H. (1999). The consert instrument for the rosetta mission. *Advances in Space Research*, 24(9):1115–1126.

Bardyn, A., Baklouti, D., Cottin, H., Fray, N., Briois, C., Paquette, J., Stenzel, O., Engrand, C., Fischer, H., Hornung, K., Isnard, R., Langevin, Y., Lehto, H., Le Roy, L., Ligier, N., Merouane, S., Modica, P., Orthous-Daunay, F.-R., Ryn, J., Schulz, R., Siln, J., Thirkell, L., Varmuza, K., Zaprudin, B., Kissel, J., and Hilchenbach, M. (2017). Carbon-rich dust in comet 67P/Churyumov-Gerasimenko measured by COSIMA/Rosetta. *Monthly Notices of the Royal Astronomical Society*, 469(Suppl˙2):S712–S722.

Basilevsky, A., Head, J., Horz, F., and Ramsley, K. (2015). Survival times of meter-sized rock boulders on the surface of airless bodies. *Planetary and Space Science*, 117:312–328.

Belton, M. J. S., Zou, X.-D., Li, J.-Y., and Asphaug, E. (2018). On the origin of internal layers in comet nuclei. *Icarus*, 314:364–375.

Bertini, I., La Forgia, F., Fulle, M., Tubiana, C., Gttler, C., Moreno, F., Agarwal, J., Munoz, O., Mottola, S., Ivanovsky, S., Pajola, M., Lucchetti, A., Petropoulou, V., Lazzarin, M., Rotundi, A., Bodewits, D., Frattin, E., Toth, I., Masoumzadeh, N., Kovacs, G., Rinaldi, G., Guirado, D., Sierks, H., Naletto, G., Lamy, P., Rodrigo, R., Koschny, D., Davidsson, B., Barbieri, C., Barucci, M. A., Bertaux, J.-L., Cambianica, P., Cremonese, G., Da Deppo, V., Debei, S., De Cecco, M., Deller, J., Ferrari, S., Ferri, F., Fornasier, S., Gutierrez, P. J., Hasselmann, P. H., Ip, W.-H., Keller, H. U., Lara, L. M., Lopez Moreno, J. J., Marzari, F., Massironi, M., Penasa, L., and Shi, X. (2018). The backscattering ratio of comet 67P/ChuryumovGerasimenko dust coma as seen by OSIRIS onboard Rosetta. *Monthly Notices of the Royal Astronomical Society*, 482(3):2924–2933.

Bibring, J.-P., Lamy, P., Langevin, Y., Soufflot, A., Berthé, M., Borg, J., Poulet, F., and Mottola, S. (2007). Civa. *Space Science Reviews*, 128(1-4):397–412.

Biele, J., Ulamec, S., Maibaum, M., Roll, R., Witte, L., Jurado, E., Muñoz, P., Arnold, W., Auster, H.-U., Casas, C., Faber, C., Fantinati, C., Finke, F., Fischer, H.-H., Geurts, K., Güttler, C., Heinisch, P., Herique, A., Hviid, S., Kargl, G., Knapmeyer, M., Knollenberg, J., Kofman, W., Kömle, N., Kührt, E., Lommatsch, V., Mottola, S., Pardo de Santayana, R., Remetean, E., Scholten, F., Seidensticker, K. J., Sierks, H., and Spohn, T. (2015). The landing(s) of philae and inferences about comet surface mechanical properties. *Science*, 349(6247).

Birch, S. P. D., Tang, Y., Hayes, A. G., Kirk, R. L., Bodewits, D., Campins, H., Fernandez, Y., de Freitas Bart, R., Kutsop, N. W., Sierks, H., Soderblom, J. M., Squyres, S. W., and Vincent, J.-B. (2017). Geomorphology of comet 67P/ChuryumovGerasimenko. *Monthly Notices of the Royal Astronomical Society*, 469(Suppl˙2):S50–S67.

Bittelli, M., Campbell, G., and Flury, M. (1999). Characterization of particle-size distribution in soils with a fragmentation model. *Soil Science Society of America Journal - SSSAJ*, 63:782–788.

Blum, J., Gundlach, B., Krause, M., Fulle, M., Johansen, A., Agarwal, J., von Borstel, I., Shi, X., Hu, X., Bentley, M. S., et al. (2017). Evidence for the formation of comet 67p/churyumov-gerasimenko through gravitational collapse of a bound clump of pebbles. *Monthly Notices of the Royal Astronomical Society*, 469(Suppl_2):S755–S773.

Boogert, A. A., Gerakines, P. A., and Whittet, D. C. (2015). Observations of the icy universe. *Annual Review of Astronomy and Astrophysics*, 53:541–581.

Bourke, M. C., Brearley, J. A., Haas, R., and Viles, H. A. (2007a). A photographic atlas of rock breakdown features in geomorphic environments.

Bourke, M. C., Brearley, J. A., Haas, R., and Viles, H. A. (2007b). A photographic atlas of rock breakdown features in geomorphic environments.

Bourne, N., Millett, J., and Pickup, I. (1997). Delayed failure in shocked silicon carbide. *Journal of Applied Physics*, 81(9):6019–6023.

Buratti, B. J., Choukroun, M., and Bauer, J. M. (2016). The Low Albedo of Comets. *AGU Fall Meeting Abstracts*, pages P43A–2083.

Burbine, T. H., McCoy, T. J., Meibom, A., Gladman, B., and Keil, K. (2002). Meteoritic parent bodies: Their number and identification. *Asteroids III.*

Cambianica, P., Cremonese, G., Naletto, G., Lucchetti, A., Pajola, M., Penasa, L., Simioni, E., and Massironi, M. (2019). Quantitative analysis of isolated boulder fields on comet 67p/churyumov-gerasimenko. *Astronomy & Astrophysics*, 630(A15):S636–S645.

Capaccioni, F. a., Coradini, A., Filacchione, G., Erard, S., Arnold, G., Drossart, P., De Sanctis, M., Bockelee-Morvan, D., Capria, M., Tosi, F., et al. (2015). The organic-rich surface of comet 67p/churyumov-gerasimenko as seen by virtis/rosetta. *Science*, 347(6220):aaa0628.

Carr, C., Cupido, E., Lee, C., Balogh, A., Beek, T., Burch, J., Dunford, C., Eriksson, A., Gill, R., Glassmeier, K., et al. (2007). Rpc: The rosetta plasma consortium. *Space Science Reviews*, 128(1-4):629–647.

Ceccarelli, C., Castets, A., Caux, E., Hollenbach, D., Loinard, L., Molinari, S., and Tielens, A. (2000). The structure of the collapsing envelope around the low-mass protostar iras 16293-2422. *Astronomy and Astrophysics*, 355:1129–1137.

Cheng, S. C. and Vachon, R. (1969). The prediction of the thermal conductivity of two and three phase solid heterogeneous mixtures. *International Journal of Heat and Mass Transfer*, 12(3):249–264.

Choukroun, M., Keihm, S., Schloerb, F., Gulkis, S., Lellouch, E., Leyrat, C., von Allmen, P., Biver, N., Bockelée-Morvan, D., Crovisier, J., et al. (2015). Dark side of comet 67p/churyumov-gerasimenko in aug.–oct. 2014-miro/rosetta continuum observations of polar night in the southern regions. *Astronomy & Astrophysics*, 583:A28.

Cintala, M. J. (1992). Impact-induced thermal effects in the lunar and mercurian regoliths. *Journal of Geophysical Research: Planets*, 97(E1):947–973.

Colangeli, L., Lopez-Moreno, J., Palumbo, P., Rodriguez, J., Cosi, M., Della Corte, V., Esposito, F., Fulle, M., Herranz, M., Jeronimo, J., et al.

(2007). The grain impact analyser and dust accumulator (giada) experiment for the rosetta mission: design, performances and first results. *Space Science Reviews*, 128(1-4):803–821.

Coradini, A., Capaccioni, F., Drossart, P., Arnold, G., Ammannito, E., Angrilli, F., Barucci, A., Bellucci, G., Benkhoff, J., Bianchini, G., et al. (2007). Virtis: An imaging spectrometer for the rosetta mission. *Space Science Reviews*, 128(1-4):529–559.

Cremonese, G., Arpigny, C., Manfroid, J., Bockelee-Morvan, D., Crovisier, J., Rauer, H., Boehnhardt, H., Fitzsimmons, A., Fulle, M., Jockers, K., et al. (1997). The european hale-bopp team observations of comet hale-bopp. In *Bulletin of the American Astronomical Society*, volume 29, page 1035.

Cremonese, G. and Fulle, M. (1997). Sodium in comets. *Earth, Moon, and Planets*, 79(1-3):209–220.

D. McFadden, L., Eppes, M., R. Gillespie, A., and Hallet, B. (2005). Physical weathering in arid landscape due to diurnal variation in the direction of solar heating. *Geological Society of America Bulletin - GEOL SOC AMER BULL*, 117.

De Sanctis, M., Capaccioni, F., Ciarniello, M., Filacchione, G., Formisano, M., Mottola, S., Raponi, A., Tosi, F., Bockelée-Morvan, D., Erard, S., et al. (2015). The diurnal cycle of water ice on comet 67p/churyumov–gerasimenko. *Nature*, 525(7570):500.

Delannay, R., Le Caër, G., and Botet, R. (1996). A simple soluble model of discrete sequential fragmentation. *Journal of Physics A: Mathematical and General*, 29(21):6693.

Dorn, R. I. (2003). Boulder weathering and erosion associated with a wildfire, sierra ancha mountains, arizona. *Geomorphology*, 55(1-4):155–171.

Duncan, M., Quinn, T., and Tremaine, S. (1988). The origin of short-period comets. *The Astrophysical Journal*, 328:L69–L73.

Ehlmann, B. L., Viles, H. A., and Bourke, M. C. (2008). Quantitative morphologic analysis of boulder shape and surface texture to infer environmental history: A case study of rock breakdown at the ephrata fan, channeled scabland, washington. *Journal of Geophysical Research: Earth Surface*, 113(F2).

El-Maarry, M. R., Groussin, O., Thomas, N., Pajola, M., Auger, A.-T., Davidsson, B., Hu, X., Hviid, S. F., Knollenberg, J., Güttler, C., Tubiana, C., Fornasier, S., Feller, C., Hasselmann, P., Vincent, J.-B., Sierks, H., Barbieri, C., Lamy, P., Rodrigo, R., Koschny, D., Keller, H. U., Rickman, H., A'Hearn, M. F., Barucci, M. A., Bertaux, J.-L., Bertini, I., Besse, S., Bodewits, D., Cremonese, G., Da Deppo, V., Debei, S., De Cecco, M., Deller, J., Deshapriya, J. D. P., Fulle, M., Gutierrez, P. J., Hofmann, M., Ip, W.-H., Jorda, L., Kovacs, G., Kramm, J.-R., Kührt, E., Küppers, M., Lara, L. M., Lazzarin, M., Lin, Z.-Y., Lopez Moreno, J. J., Marchi, S., Marzari, F., Mottola, S., Naletto, G., Oklay, N., Pommerol, A., Preusker, F., Scholten, F., and Shi, X. (2017). Surface changes on comet 67p/churyumov-gerasimenko suggest a more active past. *Science*, 355(6332):1392–1395.

El-Maarry, M. R., Thomas, N., Giacomini, L., Massironi, M., Pajola, M., Marschall, R., Gracia-Berná, A., Sierks, H., Barbieri, C., Lamy, P. L., et al. (2015). Regional surface morphology of comet 67p/churyumov-gerasimenko from rosetta/osiris images. *Astronomy & Astrophysics*, 583:A26.

El-Maarry, M. R., Thomas, N., Gracia-Berná, A., Pajola, M., Lee, J. C., Massironi, M., Davidsson, B., Marchi, S., Keller, H. U., Hviid, S. F., Besse, S., Sierks, H., Barbieri, C., Lamy, P. L., Koschny, D., Rickman, H., Rodrigo, R., A'Hearn, M. F., Auger, A. T., Barucci, M. A., Bertaux, J. L., Bertini, I., Bodewits, D., Cremonese, G., Da Deppo, V., De Cecco, M., Debei, S., Güttler, C., Fornasier, S., Fulle, M., Giacomini, L., Groussin, O., Gutierrez, P. J., Ip, W. H., Jorda, L., Knollenberg, J., Kovacs, G., Kramm, J. R., Kührt, E., Küppers, M., Lara, L. M., Lazzarin, M., Lopez Moreno, J. J., Marschall, R., Marzari, F., Naletto, G., Oklay, N., Pommerol, A., Preusker, F., Scholten, F., Tubiana, C., and Vincent, J. B. (2016). Regional surface morphology of comet 67P/Churyumov-Gerasimenko from Rosetta/OSIRIS images: The southern hemisphere. *Astronomy and Astrophysics*, 593:A110.

Eppes, M. C., Magi, B., Hallet, B., Delmelle, E., Mackenzie-Helnwein, P., Warren, K., and Swami, S. (2016). Deciphering the role of solar-induced thermal stresses in rock weathering. *Bulletin*, 128(9-10):1315–1338.

Eppes, M.-C., Willis, A., Molaro, J., Abernathy, S., and Zhou, B. (2015). Cracks in martian boulders exhibit preferred orientations that point to solar-induced thermal stress. *Nature communications*, 6:6712.

ESRI (2011). Arcgis desktop: Release 10.3.1 redlands, ca: Environmental systems research institute.

Filacchione, G., Groussin, O., Herny, C., Kappel, D., Mottola, S., Oklay, N., Pommerol, A., Wright, I., Yoldi, Z., Ciarniello, M., et al. (2019). Comet 67p/cg nucleus composition and comparison to other comets. *Space Science Reviews*, 215(1):19.

Finzi, A. E., Zazzera, F. B., Dainese, C., Malnati, F., Magnani, P. G., Re, E., Bologna, P., Espinasse, S., and Olivieri, A. (2007). Sd2 – how to sample a comet. *Space Science Reviews*, 128(1):281–299.

Fornasier, S., Mottola, S., Keller, H. U., Barucci, M., Davidsson, B., Feller, C., Deshapriya, J., Sierks, H., Barbieri, C., Lamy, P., et al. (2016). Rosettas comet 67p/churyumov-gerasimenko sheds its dusty mantle to reveal its icy nature. *Science*, 354(6319):1566–1570.

Fougere, N., Altwegg, K., Berthelier, J.-J., Bieler, A., Bockelée-Morvan, D., Calmonte, U., Capaccioni, F., Combi, M. R., De Keyser, J., Debout, V., et al. (2016). Direct simulation monte carlo modelling of the major species in the coma of comet 67p/churyumov-gerasimenko. *Monthly Notices of the Royal Astronomical Society*, 462(Suppl_1):S156–S169.

Fulle, M., Bertini, I., Della Corte, V., Güttler, C., Ivanovski, S., La Forgia, F., Lasue, J., Levasseur-Regourd, A. C., Marzari, F., Moreno, F., et al. (2018a). The phase function and density of the dust observed at comet 67p/churyumov–gerasimenko. *Monthly Notices of the Royal Astronomical Society*, 476(2):2835–2839.

Fulle, M., Blum, J., Green, S., Gundlach, B., Herique, A., Moreno, F., Mottola, S., Rotundi, A., and Snodgrass, C. (2018b). The refractory-to-ice mass ratio in comets. *Monthly Notices of the Royal Astronomical Society*, 482(3):3326–3340.

Fulle, M., Della Corte, V., Rotundi, A., Green, S., Accolla, M., Colangeli, L., Ferrari, M., Ivanovski, S., Sordini, R., and Zakharov, V. (2017). The dust-to-ices ratio in comets and kuiper belt objects. *Monthly Notices of the Royal Astronomical Society*, 469(Suppl_2):S45–S49.

Fulle, M., Marzari, F., Della Corte, V., Fornasier, S., Sierks, H., Rotundi, A., Barbieri, C., Lamy, P. L., Rodrigo, R., Koschny, D., et al. (2016). Evolution of the dust size distribution of comet 67p/churyumov–gerasimenko from 2.2 au to perihelion. *The Astrophysical Journal*, 821(1):19.

Garenne, A., Beck, P., Montes-Hernandez, G., Chiriac, R., Toche, F., Quirico, E., Bonal, L., and Schmitt, B. (2014). The abundance and stability of water in type 1 and 2 carbonaceous chondrites (ci, cm and cr). *Geochimica et Cosmochimica Acta*, 137:93–112.

Garvin, J., Mouginis-Mark, P., and Head, J. (1981). Characterization of rock populations on planetary surfaces: Techniques and a preliminary analysis of mars and venus. *The moon and the planets*, 24(3):355–387.

Ghent, R. R., Hayne, P. O., Bandfield, J. L., Campbell, B. A., Allen, C. C., Carter, L. M., and Paige, D. A. (2014). Constraints on the recent rate of lunar ejecta breakdown and implications for crater ages. *Geology*, 42(12):1059–1062.

Glassmeier, K.-H., Boehnhardt, H., Koschny, D., Kührt, E., and Richter, I. (2007). The Rosetta Mission: Flying Towards the Origin of the Solar System. *Space Science Reviews*, 128:1–21.

Goesmann, F., Rosenbauer, H., Roll, R., and Böhnhardt, H. (2005). Cosac onboard rosetta: a bioastronomy experiment for the short-period comet 67p/churyumov-gerasimenko. *Astrobiology*, 5(5):622–631.

Golombek, M. and Rapp, D. (1997). Size-frequency distributions of rocks on mars and earth analog sites: Implications for future landed missions. *Journal of Geophysical Research: Planets*, 102(E2):4117–4129.

Golombek, M. P., Haldemann, A. F. C., Forsberg-Taylor, N. K., DiMaggio, E. N., Schroeder, R. D., Jakosky, B. M., Mellon, M. T., and Matijevic, J. R. (2003). Rock size-frequency distributions on mars and implications for mars exploration rover landing safety and operations. *Journal of Geophysical Research: Planets*, 108(E12):n/a–n/a. 8086.

Gounelle, M., Spurnỳ, P., and Bland, P. A. (2006). The orbit and atmospheric trajectory of the orgueil meteorite from historical records. *Meteoritics & Planetary Science*, 41(1):135–150.

Grady, D. (2007). *Fragmentation of rings and shells: the legacy of NF Mott*. Springer Science & Business Media.

Greenberg, J. M. and Li, A. (1999). Morphological structure and chemical composition of cometary nuclei and dust. *Space Science Reviews*, 90(1-2):149–161.

Griffith, A. and Gilman, J. J. (1968). The phenomena of rupture and flow in solids. *Transactions of the ASM*, 61:855–906.

Griggs, D. T. (1936). Deformation of Rocks under High Confining Pressures: I. Experiments at Room Temperature. *Journal of Geology*, 44:541–577.

Groussin, O., Jorda, L., Auger, A.-T., Kührt, E., Gaskell, R., Capanna, C., Scholten, F., Preusker, F., Lamy, P., Hviid, S., et al. (2015). Gravitational slopes, geomorphology, and material strengths of the nucleus of comet 67p/churyumov-gerasimenko from osiris observations. *Astronomy & Astrophysics*, 583:A32.

Gulkis, S., Allen, M., von Allmen, P., Beaudin, G., Biver, N., Bockelée-Morvan, D., Choukroun, M., Crovisier, J., Davidsson, B. J., Encrenaz, P., et al. (2015). Subsurface properties and early activity of comet 67p/churyumov-gerasimenko. *Science*, 347(6220):aaa0709.

Gulkis, S., Frerking, M., Crovisier, J., Beaudin, G., Hartogh, P., Encrenaz, P., Koch, T., Kahn, C., Salinas, Y., Nowicki, R., et al. (2007). Miro: Microwave instrument for rosetta orbiter. *Space Science Reviews*, 128(1-4):561–597.

Hall, K. and Thorn, C. E. (2014). Thermal fatigue and thermal shock in bedrock: An attempt to unravel the geomorphic processes and products. *Geomorphology*, 206:1–13.

Hernandez, G., Leon, R., Salinas, L., and Dimnet, E. (2012). A fragmentation model with neighborhood interaction. *Applied Mathematical Modelling*, 36(4):1694 – 1702.

Hörz, F. and Cintala, M. (1997). The barringer award address presented 1996 july 25, berlin, germany: Impact experiments related to the evolution of planetary regoliths. *Meteoritics & Planetary Science*, 32(2):179–209.

Hu, X., Shi, X., Sierks, H., Blum, J., Oberst, J., Fulle, M., Kührt, E., Güttler, C., Gundlach, B., Keller, H. U., et al. (2017a). Thermal modelling of water activity on comet 67p/churyumov-gerasimenko with global dust mantle and plural dust-to-ice ratio. *Monthly Notices of the Royal Astronomical Society*, 469(Suppl_2):S295–S311.

Hu, X., Shi, X., Sierks, H., Fulle, M., Blum, J., Keller, H., Kührt, E., Davidsson, B., Güttler, C., Gundlach, B., et al. (2017b). Seasonal erosion and restoration of the dust cover on comet 67p/churyumov-gerasimenko as observed by osiris onboard rosetta. *Astronomy & Astrophysics*, 604:A114.

Jorda, L., Gaskell, R., Capanna, C., Hviid, S., Lamy, P., Ďurech, J., Faury, G., Groussin, O., Gutiérrez, P., Jackman, C., Keihm, S. J., Keller, H. U., Knollenberg, J., Kührt, E., Marchi, S., Mottola, S., Palmer, E., Schloerb, F. P., Sierks, H., Vincent, J.-B., A'Hearn, M. F., Barbieri, C., Rodrigo, R., Koschny, D., Rickman, H., Barucci, M. A., Bertaux, J. L., Bertini, I., Cremonese, G., Da Deppo, V., Davidsson, B., Debei, S., De Cecco, M., Fornasier, S., Fulle, M., Güttler, C., Ip, W.-H., Kramm, J. R., Küppers, M., Lara, L. M., Lazzarin, M., Lopez Moreno, J. J., Marzari, F., Naletto, G., Oklay, N., Thomas, N., Tubiana, C., and Wenzel, K.-P. (2016). The global shape, density and rotation of Comet 67P/Churyumov-Gerasimenko from preperihelion Rosetta/OSIRIS observations. *Icarus*, 277:257–278.

Jutzi, M., Michel, P., Benz, W., and Richardson, D. C. (2010). Fragment properties at the catastrophic disruption threshold: The effect of the parent bodys internal structure. *Icarus*, 207(1):54–65.

Kadono, T. and Arakawa, M. (2002). Crack propagation in thin glass plates caused by high velocity impact. *Physical Review E*, 65(3):035107.

Keller, H. U., Barbieri, C., Lamy, P., Rickman, H., Rodrigo, R., Wenzel, K.-P., Sierks, H., AHearn, M. F., Angrilli, F., Angulo, M., et al. (2007). Osiris–the scientific camera system onboard rosetta. *Space Science Reviews*, 128(1-4):433–506.

Keller, H. U., Mottola, S., Davidsson, B., Schröder, S., Skorov, Y., Kührt, E., Groussin, O., Pajola, M., Hviid, S. F., Preusker, F., et al. (2015). Insolation, erosion, and morphology of comet 67p/churyumov-gerasimenko. *Astronomy & Astrophysics*, 583:A34.

Keller, H. U., Mottola, S., Hviid, S. F., Agarwal, J., Kührt, E., Skorov, Y., Otto, K., Vincent, J.-B., Oklay, N., Schröder, S. E., et al. (2017). Seasonal mass transfer on the nucleus of comet 67p/chuyumov–gerasimenko. *Monthly Notices of the Royal Astronomical Society*, 469(Suppl_2):S357–S371.

Kissel, J., Altwegg, K., Clark, B., Colangeli, L., Cottin, H., Czempiel, S., Eibl, J., Engrand, C., Fehringer, H., Feuerbacher, B., et al. (2007). Cosima–high resolution time-of-flight secondary ion mass spectrometer for the analysis of cometary dust particles onboard rosetta. *Space Science Reviews*, 128(1-4):823–867.

Klingelhöfer, G., Brückner, J., Duston, C., Gellert, R., and Rieder, R. (2007). The rosetta alpha particle x-ray spectrometer (apxs). *Space science reviews*, 128(1-4):383–396.

Kossacki, K. J., Spohn, T., Hagermann, A., Kaufmann, E., and Khrt, E. (2015). Comet 67p/churyumovgerasimenko: Hardening of the sub-surface layer. *Icarus*, 260:464 – 474.

Kranz, R. L. (1979). Crack growth and development during creep of barre granite. In *International Journal of Rock Mechanics and Mining Sciences & Geomechanics Abstracts*, volume 16, pages 23–35. Elsevier.

Kranz, R. L. (1983). Microcracks in rocks: A review. *Tectonophysics*, 100:449–480.

Krapivsky, P. and Majumdar, S. N. (2000). Traveling waves, front selection, and exact nontrivial exponents in a random fragmentation problem. *Physical review letters*, 85(26):5492.

Kuiper, G. and Hynek, J. (1951). On the origin of the solar system, in astrophysics: a topical symposium. In *AstrophysicsA Topical Symposium*, page 357. McGraw Hill NY.

Lamp, J. L., Marchant, D. R., Mackay, S. L., and Head, J. W. (2017). Thermal stress weathering and the spalling of antarctic rocks. *Journal of Geophysical Research: Earth Surface*, 122(1):3–24.

Lamy, P. L., Toth, I., Fernandez, Y. R., and Weaver, H. A. (2004). *The sizes, shapes, albedos, and colors of cometary nuclei*, pages 223–264.

Lamy, P. L., Toth, I., Weaver, H. A., Jorda, L., Kaasalainen, M., and Gutiérrez, P. J. (2006). Hubble Space Telescope observations of the nucleus and inner coma of comet 67P/Churyumov-Gerasimenko. *Astronomy and Astrophysics*, 458:669–678.

Le Feuvre, M. and Wieczorek, M. A. (2011). Nonuniform cratering of the moon and a revised crater chronology of the inner solar system. *Icarus*, 214(1):1–20.

Li, B., Ling, Z., Zhang, J., and Chen, J. (2017). Rock size-frequency distributions analysis at lunar landing sites based on remote sensing and in-situ imagery. *Planetary and Space Science*.

Lienau, C. (1936). Random fracture of a brittle solid. *Journal of the Franklin Institute*, 221(6):769 – 787.

Lindborg, U. (1969). A statistical model for the linking of microcracks. *Acta Metallurgica*, 17(4):521–526.

Lorek, S., Gundlach, B., Lacerda, P., and Blum, J. (2016). Comet formation in collapsing pebble clouds-what cometary bulk density implies for the cloud mass and dust-to-ice ratio. *Astronomy & Astrophysics*, 587:A128.

Mandelbrot, B. (1967). How Long Is the Coast of Britain? Statistical Self-Similarity and Fractional Dimension. *Science*, 156:636–638.

Mandelbrot, B. B. (1983). *The fractal geometry of nature*, volume 173. WH freeman New York.

Marshall, D., Hartogh, P., Rezac, L., von Allmen, P., Biver, N., Bockelée-Morvan, D., Crovisier, J., Encrenaz, P., Gulkis, S., Hofstadter, M., et al. (2017). Spatially resolved evolution of the local h2o production rates of comet 67p/churyumov-gerasimenko from the miro instrument on rosetta. *Astronomy & Astrophysics*, 603:A87.

Massironi, M., Simioni, E., Marzari, F., Cremonese, G., Giacomini, L., Pajola, M., Jorda, L., Naletto, G., Lowry, S., El-Maarry, M. R., et al. (2015). Two independent and primitive envelopes of the bilobate nucleus of comet 67p. *Nature*, 526(7573):402.

MATLAB (2010). *version 7.10.0 (R2010a)*. The MathWorks Inc., Natick, Massachusetts.

Matsushita, M., Hayakawa, Y., and Sawada, Y. (1985). Fractal structure and cluster statistics of zinc-metal trees de- posited on a line electrode. *Phys. Rev. A*, 32:3814–3816.

Migliorini, A., Piccioni, G., Capaccioni, F., Filacchione, G., Bockelée-Morvan, D., Erard, S., Leyrat, C., Combi, M. R., Fougere, N., Crovisier, J., Taylor, F. W., De Sanctis, M. C., Capria, M. T., Grassi, D., Rinaldi, G., Tozzi, G. P., and Fink, U. (2016). Water and carbon dioxide distribution in the 67P/Churyumov-Gerasimenko coma from VIRTIS-M infrared observations. *Astronomy and Astrophysics*, 589:A45.

Miloevic, N. T., Elston, G. N., Krstonoic, B., and Rajkovic, N. (2013). Box-count analysis of two dimensional images: Methodology, analysis and classification. In *2013 19th International Conference on Control Systems and Computer Science*, pages 306–312.

Mogi, K., Yamashita, S., Nakamura, T., Matsuoka, M., Okumura, S., and Furukawa, Y. (2017). Dehydration Process of Experimentally Heated Murchison Without any Effects of Adsorbed and Rehydrated Water. In *80th*

Annual Meeting of the Meteoritical Society, volume 1987 of *LPI Contributions*, page 6225.

Möhlmann, D., Seidensticker, K. J., Fischer, H.-H., Faber, C., Flandes, A., Knapmeyer, M., Krger, H., Roll, R., Scholten, F., Thiel, K., and Arnold, W. (2018). Compressive strength and elastic modulus at agilkia on comet 67p/churyumov-gerasimenko derived from the sesame/casse touchdown signals. *Icarus*, 303:251 – 264.

Molaro, J. L., Byrne, S., and Langer, S. A. (2015). Grain-scale thermoelastic stresses and spatiotemporal temperature gradients on airless bodies, implications for rock breakdown. *Journal of Geophysical Research: Planets*, 120(2):255–277.

Molaro, J. L., Byrne, S., and Le, J. L. (2017). Thermally induced stresses in boulders on airless body surfaces, and implications for rock breakdown. *Icarus*, 294:247–261.

Morbidelli, A. (2005). Origin and dynamical evolution of comets and their reservoirs. *arXiv preprint astro-ph/0512256*.

Morbidelli, A., Lunine, J., O'Brien, D., Raymond, S., and Walsh, K. (2012). Building terrestrial planets. *Annual Review of Earth and Planetary Sciences*, 40(1):251–275.

Mott, N. (2006a). Fragmentation of he shells: a theoretical formula for the distribution of weights of fragments. In *Fragmentation of Rings and Shells*, pages 227–241. Springer.

Mott, N. (2006b). *A Theory of the Fragmentation of Shells and Bombs*, pages 243–294. Springer Berlin Heidelberg, Berlin, Heidelberg.

Mottola, S., Arnold, G., Grothues, H.-G., Jaumann, R., Michaelis, H., Neukum, G., and Bibring, J.-P. (2007). The rolis experiment on the rosetta lander. *Space Science Reviews*, 128(1-4):241–255.

Mottola, S., Arnold, G., Grothues, H.-G., Jaumann, R., Michaelis, H., Neukum, G., Bibring, J.-P., Schröder, S. E., Hamm, M., Otto, K. A., Pelivan, I., Proffe, G., Scholten, F., Tirsch, D., Kreslavsky, M., Remetean, E., Souvannavong, F., and Dolives, B. (2015). The structure of the regolith on 67p/churyumov-gerasimenko from rolis descent imaging. *Science*, 349(6247).

Mottola, S., Lowry, S., Snodgrass, C., Lamy, P. L., Toth, I., Rożek, A., Sierks, H., A'Hearn, M. F., Angrilli, F., Barbieri, C., Barucci, M. A., Bertaux, J.-L., Cremonese, G., Da Deppo, V., Davidsson, B., De Cecco, M., Debei, S., Fornasier, S., Fulle, M., Groussin, O., Gutiérrez, P., Hviid, S. F., Ip, W., Jorda, L., Keller, H. U., Knollenberg, J., Koschny, D., Kramm, R., Kührt, E., Küppers, M., Lara, L., Lazzarin, M., Lopez Moreno, J. J., Marzari, F., Michalik, H., Naletto, G., Rickman, H., Rodrigo, R., Sabau, L., Thomas, N., Wenzel, K.-P., Agarwal, J., Bertini, I., Ferri, F., Güttler, C., Magrin, S., Oklay, N., Tubiana, C., and Vincent, J.-B. (2014). The rotation state of 67P/Churyumov-Gerasimenko from approach observations with the OSIRIS cameras on Rosetta. *Astronomy and Astrophysics*, 569:L2.

Nyquist, H. (1928). Certain Topics in Telegraph Transmission Theory. *Transactions of the American Institute of Electrical Engineers*, 47:617–644.

OBrien, D. P., Izidoro, A., Jacobson, S. A., Raymond, S. N., and Rubie, D. C. (2018). The delivery of water during terrestrial planet formation. *Space Science Reviews*, 214(1):47.

Ogliore, R., Westphal, A., Gainsforth, Z., Butterworth, A., Fakra, S., and Marcus, M. A. (2009). Nebular mixing constrained by the stardust samples. *Meteoritics & planetary science*, 44(10):1675–1681.

Orowan, E. (1944). The Fatigue of Glass Under Stress. *Nature*, 154:341–343.

Ott, T., Drolshagen, E., Koschny, D., Gttler, C., Tubiana, C., Frattin, E., Agarwal, J., Sierks, H., Bertini, I., Barbieri, C., Lamy, P. I., Rodrigo, R., Rickman, H., AHearn, M. F., Barucci, M. A., Bertaux, J.-L., Boudreault, S., Cremonese, G., Da Deppo, V., Davidsson, B., Debei, S., De Cecco, M., Deller, J., Feller, C., Fornasier, S., Fulle, M., Geiger, B., Gicquel, A., Groussin, O., Gutirrez, P. J., Hofmann, M., Hviid, S. F., Ip, W.-H., Jorda, L., Keller, H. U., Knollenberg, J., Kovacs, G., Kramm, J. R., Khrt, E., Kppers, M., Lara, L. M., Lazzarin, M., Lin, Z.-Y., Lpez-Moreno, J. J., Marzari, F., Mottola, S., Naletto, G., Oklay, N., Pajola, M., Shi, X., Thomas, N., Vincent, J.-B., and Poppe, B. (2017). Dust mass distribution around comet 67P/ChuryumovGerasimenko determined via parallax measurements using Rosetta's OSIRIS cameras. *Monthly Notices of the Royal Astronomical Society*, 469(Suppl˙2):S276–S284.

Pajola, M., Lee, J.-C., Oklay, N., Hviid, S. F., Penasa, L., Mottola, S., Shi, X., Fornasier, S., Davidsson, B., Giacomini, L., Lucchetti, A., Massironi, M., Vincent, J. B., Bertini, I., Naletto, G., Ip, W. H., Sierks, H., Lamy,

P. L., Rodrigo, R., Koschny, D., Keller, H. U., Agarwal, J., Barucci, M. A., Bertaux, J. L., Bodewits, D., Cambianica, P., Cremonese, G., Da Deppo, V., Debei, S., De Cecco, M., Deller, J., El Maarry, M. R., Feller, C., Ferrari, S., Fulle, M., Gutierrez, P. J., Gttler, C., Lara, L. M., La Forgia, F., Lazzarin, M., Lin, Z.-Y., Lopez Moreno, J. J., Marzari, F., Preusker, F., Scholten, F., Toth, I., and Tubiana, C. (2019). Multidisciplinary analysis of the Hapi region located on Comet 67P/ChuryumovGerasimenko. *Monthly Notices of the Royal Astronomical Society*, 485(2):2139–2154.

Pajola, M., Lucchetti, A., Fulle, M., Mottola, S., Hamm, M., Da Deppo, V., Penasa, L., Kovacs, G., Massironi, M., Shi, X., Tubiana, C., Gttler, C., Oklay, N., Vincent, J. B., Toth, I., Davidsson, B., Naletto, G., Sierks, H., Barbieri, C., Lamy, P. L., Rodrigo, R., Koschny, D., Rickman, H., Keller, H. U., Agarwal, J., AHearn, M. F., Barucci, M. A., Bertaux, J. L., Bertini, I., Cremonese, G., Debei, S., De Cecco, M., Deller, J., El Maarry, M. R., Fornasier, S., Frattin, E., Gicquel, A., Groussin, O., Gutierrez, P. J., Hfner, S., Hofmann, M., Hviid, S. F., Ip, W. H., Jorda, L., Knollenberg, J., Kramm, J. R., Khrt, E., Kppers, M., Lara, L. M., Lazzarin, M., Moreno, J. J. L., Marzari, F., Michalik, H., Preusker, F., Scholten, F., and Thomas, N. (2017). The pebbles/boulders size distributions on Sais: Rosettas final landing site on comet 67P/ChuryumovGerasimenko. *Monthly Notices of the Royal Astronomical Society*, 469(Suppl˙2):S636–S645.

Pajola, M., Lucchetti, A., Fulle, M., Mottola, S., Hamm, M., Da Deppo, V., Penasa, L., Kovacs, G., Massironi, M., Shi, X., Tubiana, C., Güttler, C., Oklay, N., Vincent, J. B., Toth, I., Davidsson, B., Naletto, G., Sierks, H., Barbieri, C., Lamy, P. L., Rodrigo, R., Koschny, D., Rickman, H., Keller, H. U., Agarwal, J., A'Hearn, M. F., Barucci, M. A., Bertaux, J. L., Bertini, I., Cremonese, G., Debei, S., De Cecco, M., Deller, J., El Maarry, M. R., Fornasier, S., Frattin, E., Gicquel, A., Groussin, O., Gutierrez, P. J., Höfner, S., Hofmann, M., Hviid, S. F., Ip, W. H., Jorda, L., Knollenberg, J., Kramm, J. R., Kührt, E., Küppers, M., Lara, L. M., Lazzarin, M., Moreno, J. J. L., Marzari, F., Michalik, H., Preusker, F., Scholten, F., and Thomas, N. (2017). The pebbles/boulders size distributions on Sais: Rosetta's final landing site on comet 67P/Churyumov-Gerasimenko. *Monthly Notices of the Royal Astronomical Society*, 469:S636–S645.

Pajola, M., Vincent, J.-B., Güttler, C., Lee, J.-C., Bertini, I., Massironi, M., Simioni, E., Marzari, F., Giacomini, L., Lucchetti, A., et al. (2015). Size-frequency distribution of boulders 7 m on comet 67p/churyumov-gerasimenko. *Astronomy & Astrophysics*, 583:A37.

Paris, P. and Erdogan, F. (1963). A critical analysis of crack propagation laws. *Journal of basic engineering*, 85(4):528–533.

Pätzold, M., Andert, T., Hahn, M., Asmar, S. W., Barriot, J.-P., Bird, M. K., Häusler, B., Peter, K., Tellmann, S., Grün, E., Weissman, P. R., Sierks, H., Jorda, L., Gaskell, R., Preusker, F., and Scholten, F. (2016). A homogeneous nucleus for comet 67P/Churyumov-Gerasimenko from its gravity field. *Nature*, 530:63–65.

Pätzold, M., Andert, T. P., Hahn, M., Barriot, J.-P., Asmar, S. W., Häusler, B., Bird, M. K., Tellmann, S., Oschlisniok, J., and Peter, K. (2018). The nucleus of comet 67p/churyumov–gerasimenko–part i: The global view–nucleus mass, mass-loss, porosity, and implications. *Monthly Notices of the Royal Astronomical Society*, 483(2):2337–2346.

Pätzold, M., Häusler, B., Aksnes, K., Anderson, J. D., Asmar, S. W., Barriot, J.-P., Bird, M. K., Boehnhardt, H., Eidel, W., Grün, E., et al. (2007). Rosetta radio science investigations (rsi). *Space science reviews*, 128(1-4):599–627.

Penasa, L., Massironi, M., Ferrari, S., Pajola, M., Marzari, F., Naletto, G., Bertini, I., Cremonese, G., Ferri, F., La Forgia, F., Frattin, E., Lazzarin, M., Lucchetti, A., and Simioni, E. (2017). The layered structure of the nucleus of the comet 67P: implications on missing volumes and lobes orientations. *European Planetary Science Congress*, 11:EPSC2017–485.

Penasa, L., Massironi, M., Naletto, G., Simioni, E., Ferrari, S., Pajola, M., Lucchetti, A., Preusker, F., Scholten, F., Jorda, L., Gaskell, R., Ferri, F., Marzari, F., Davidsson, B., Mottola, S., Sierks, H., Barbieri, C., Lamy, P. L., Rodrigo, R., Koschny, D., Rickman, H., Keller, H. U., Agarwal, J., AHearn, M. F., Barucci, M. A., Bertaux, J. L., Bertini, I., Cremonese, G., Da Deppo, V., Debei, S., De Cecco, M., Deller, J., Feller, C., Fornasier, S., Frattin, E., Fulle, M., Groussin, O., Gutierrez, P. J., Gttler, C., Hofmann, M., Hviid, S. F., Ip, W. H., Knollenberg, J., Kramm, J. R., Khrt, E., Kppers, M., La Forgia, F., Lara, L. M., Lazzarin, M., Lee, J.-C., Lopez Moreno, J. J., Oklay, N., Shi, X., Thomas, N., Tubiana, C., and Vincent, J. B. (2017). A three-dimensional modelling of the layered structure of comet 67P/Churyumov-Gerasimenko. *Monthly Notices of the Royal Astronomical Society*, 469(Suppl˙2):S741–S754.

Perfect, E. (1997). Fractal models for the fragmentation of rocks and soils: a review. *Engineering Geology*, 48(3):185 – 198. Fractals in Engineering Geology.

Preusker, F., Scholten, F., Matz, K.-D., Roatsch, T., Hviid, S. F., Mottola, S., Knollenberg, J., Kührt, E., Pajola, M., Oklay, N., Vincent, J.-B., Davidsson, B., A'Hearn, M. F., Agarwal, J., Barbieri, C., Barucci, M. A., Bertaux, J.-L., Bertini, I., Cremonese, G., Da Deppo, V., Debei, S., De Cecco, M., Fornasier, S., Fulle, M., Groussin, O., Gutiérrez, P. J., Güttler, C., Ip, W.-H., Jorda, L., Keller, H. U., Koschny, D., Kramm, J. R., Küppers, M., Lamy, P., Lara, L. M., Lazzarin, M., Lopez Moreno, J. J., Marzari, F., Massironi, M., Naletto, G., Rickman, H., Rodrigo, R., Sierks, H., Thomas, N., and Tubiana, C. (2017). The global meter-level shape model of comet 67P/Churyumov-Gerasimenko. *Astronomy and Astrophysics*, 607:L1.

Ptzold, M., Andert, T. P., Hahn, M., Barriot, J.-P., Asmar, S. W., Husler, B., Bird, M. K., Tellmann, S., Oschlisniok, J., and Peter, K. (2018). The Nucleus of comet 67P/ChuryumovGerasimenko Part I: The global view nucleus mass, mass-loss, porosity, and implications. *Monthly Notices of the Royal Astronomical Society*, 483(2):2337–2346.

R Core Team (2013). *R: A Language and Environment for Statistical Computing.* R Foundation for Statistical Computing, Vienna, Austria.

Riedler, W., Torkar, K., Jeszenszky, H., Romstedt, J., Alleyne, H. S. C., Arends, H., Barth, W., Biezen, J., Butler, B., Ehrenfreund, P., et al. (2007). Midas–the micro-imaging dust analysis system for the rosetta mission. *Space Science Reviews*, 128(1-4):869–904.

Riley, N. A. (1941). Projection sphericity. *Journal of Sedimentary Research*, 11(2):94.

Rosin, P. (1933). The laws governing the fineness of powdered coal.

Rotundi, A., Sierks, H., Della Corte, V., Fulle, M., Gutierrez, P. J., Lara, L., Barbieri, C., Lamy, P. L., Rodrigo, R., Koschny, D., et al. (2015). Dust measurements in the coma of comet 67p/churyumov-gerasimenko inbound to the sun. *Science*, 347(6220):aaa3905.

Schmidt, M., Rumpel, C., and Kögel-Knabner, I. (1999). Particle size fractionation of soil containing coal and combusted particles. *European Journal of Soil Science*, 50(3):515–522.

Schneider, C. A., Rasband, W. S., and Eliceiri, K. W. (2012). Nih image to imagej: 25 years of image analysis. *Nature methods*, 9(7):671.

Schuhmann Jr, R. (1940). Principles of comminution, i-size distribution and surface calculations. *Am. Inst. Min. Met. Eng., Tech. Pub.*, 1189:1–11.

Seeds, M. A. (1997). Foundations of astronomy. *Belmont, CA: Wadsworth Pub. Co., c1997. 4th ed.*

Seidensticker, K. J., Möhlmann, D., Apathy, I., Schmidt, W., Thiel, K., Arnold, W., Fischer, H.-H., Kretschmer, M., Madlener, D., Péter, A., Trautner, R., and Schieke, S. (2007). Sesame – an experiment of the rosetta lander philae: Objectives and general design. *Space Science Reviews*, 128(1):301–337.

Shi, X., Hu, X., Mottola, S., Sierks, H., Keller, H., Rose, M., Güttler, C., Fulle, M., Fornasier, S., Agarwal, J., et al. (2018). Coma morphology of comet 67p controlled by insolation over irregular nucleus. *Nature Astronomy*, 2(7):562.

Sierks, H., Barbieri, C., Lamy, P. L., Rodrigo, R., Koschny, D., Rickman, H., Keller, H. U., Agarwal, J., A'Hearn, M. F., Angrilli, F., Auger, A.-T., Barucci, M. A., Bertaux, J.-L., Bertini, I., Besse, S., Bodewits, D., Capanna, C., Cremonese, G., Da Deppo, V., Davidsson, B., Debei, S., De Cecco, M., Ferri, F., Fornasier, S., Fulle, M., Gaskell, R., Giacomini, L., Groussin, O., Gutierrez-Marques, P., Gutiérrez, P. J., Güttler, C., Hoekzema, N., Hviid, S. F., Ip, W.-H., Jorda, L., Knollenberg, J., Kovacs, G., Kramm, J. R., Kührt, E., Küppers, M., La Forgia, F., Lara, L. M., Lazzarin, M., Leyrat, C., Lopez Moreno, J. J., Magrin, S., Marchi, S., Marzari, F., Massironi, M., Michalik, H., Moissl, R., Mottola, S., Naletto, G., Oklay, N., Pajola, M., Pertile, M., Preusker, F., Sabau, L., Scholten, F., Snodgrass, C., Thomas, N., Tubiana, C., Vincent, J.-B., Wenzel, K.-P., Zaccariotto, M., and Pätzold, M. (2015). On the nucleus structure and activity of comet 67p/churyumov-gerasimenko. *Science*, 347(6220).

Smith, T., Marks, W., Lange, G., Sheriff, W., and Neale, E. (1989). A fractal analysis of cell images. *Journal of Neuroscience Methods*, 27(2):173 – 180.

Spitzer Jr, L. (2008). *Physical processes in the interstellar medium.* John Wiley & Sons.

Spohn, T., Seiferlin, K., Hagermann, A., Knollenberg, J., Ball, A. J., Banaszkiewicz, M., Benkhoff, J., Gadomski, S., Gregorczyk, W., Grygorczuk, J., et al. (2007). Mupus–a thermal and mechanical properties probe for the rosetta lander philae. *Space Science Reviews*, 128(1-4):339–362.

Sprunt, E. S. and Brace, W. (1974). Direct observation of microcavities in crystalline rocks. In *International Journal of Rock Mechanics and Mining Sciences & Geomechanics Abstracts*, volume 11, pages 139–150. Elsevier.

Stern, S., Slater, D., Scherrer, J., Stone, J., Versteeg, M., Ahearn, M. F., Bertaux, J.-L., Feldman, P., Festou, M., Parker, J. W., et al. (2007). Alice: the rosetta ultraviolet imaging spectrograph. *Space Science Reviews*, 128(1-4):507–527.

Stern, S. A. and Colwell, J. E. (1997). Collisional Erosion in the Primordial Edgeworth-Kuiper Belt and the Generation of the 30-50 AU Kuiper Gap. *Astrophysical Journal*, 490:879–882.

Tang, Y., Birch, S. P. D., Hayes, A. G., de Freitas Bart, R., and Squyres, S. W. (2017). Boulder Size Frequency Distribution on Comet 67P/Churyumov-Gerasimenko. In *Lunar and Planetary Science Conference*, volume 48 of *Lunar and Planetary Inst. Technical Report*, page 2796.

Thirumalai, K. and Demou, S. (1974). Thermal expansion behavior of intact and thermally fractured mine rocks. In *AIP Conference Proceedings*, volume 17, pages 60–71. AIP.

Thomas, N., Davidsson, B., El-Maarry, M. R., Fornasier, S., Giacomini, L., Gracia-Berná, A., Hviid, S., Ip, W.-H., Jorda, L., Keller, H., et al. (2015a). Redistribution of particles across the nucleus of comet 67p/churyumov-gerasimenko. *Astronomy & Astrophysics*, 583:A17.

Thomas, N., El Maarry, M. R., Theologou, P., Preusker, F., Scholten, F., Jorda, L., Hviid, S., Marschall, R., Kührt, E., Naletto, G., et al. (2018). Regional unit definition for the nucleus of comet 67p/churyumov-gerasimenko on the shap7 model. *Planetary and space science*, 164:19–36.

Thomas, N., Sierks, H., Barbieri, C., Lamy, P. L., Rodrigo, R., Rickman, H., Koschny, D., Keller, H. U., Agarwal, J., A'Hearn, M. F., et al. (2015b). The morphological diversity of comet 67p/churyumov-gerasimenko. *Science*, 347(6220):aaa0440.

Todd, J. F., Barber, S. J., Wright, I. P., Morgan, G. H., Morse, A. D., Sheridan, S., Leese, M. R., Maynard, J., Evans, S. T., Pillinger, C. T., et al. (2007). Ion trap mass spectrometry on a comet nucleus: the ptolemy instrument and the rosetta space mission. *Journal of Mass Spectrometry*, 42(1):1–10.

Turcotte, D. (1986). Fractals and fragmentation. *Journal of Geophysical Research: Solid Earth*, 91(B2):1921–1926.

Tyler, S. W. and Wheatcraft, S. W. (1992). Fractal scaling of soil particle-size distributions: analysis and limitations. *Soil Science Society of America Journal*, 56(2):362–369.

van Boekel, R., Min, M., Leinert, C., Waters, L. B. F. M., Richichi, A., Chesneau, O., Dominik, C., Jaffe, W., Dutrey, A., Graser, U., Henning, T., de Jong, J., Köhler, R., de Koter, A., Lopez, B., Malbet, F., Morel, S., Paresce, F., Perrin, G., Preibisch, T., Przygodda, F., Schöller, M., and Wittkowski, M. (2004). The building blocks of planets within the 'terrestrial' region of protoplanetary disks. *Nature*, 432:479–482.

Viles, H. and Goudie, A. (2007). Rapid salt weathering in the coastal namib desert: Implications for landscape development. *Geomorphology*, 85(1-2):49–62.

Viles, H. and Goudie, A. (2013). Weathering in the central namib desert, namibia: controls, processes and implications. *Journal of Arid Environments*, 93:20–29.

Viles, H. A. (2001). Scale issues in weathering studies. *Geomorphology*, 41(1):63–72.

Vincent, J.-B., Bodewits, D., Besse, S., Sierks, H., Barbieri, C., Lamy, P., Rodrigo, R., Koschny, D., Rickman, H., Keller, H. U., et al. (2015a). Large heterogeneities in comet 67p as revealed by active pits from sinkhole collapse. *Nature*, 523(7558):63.

Vincent, J.-B., Hviid, S. F., Mottola, S., Kuehrt, E., Preusker, F., Scholten, F., Keller, H. U., Oklay, N., de Niem, D., Davidsson, B., Fulle, M., Pajola, M., Hofmann, M., Hu, X., Rickman, H., Lin, Z.-Y., Feller, C., Gicquel, A., Boudreault, S., Sierks, H., Barbieri, C., Lamy, P. L., Rodrigo, R., Koschny, D., AHearn, M. F., Barucci, M. A., Bertaux, J.-L., Bertini, I., Cremonese, G., Da Deppo, V., Debei, S., De Cecco, M., Deller, J., Fornasier, S., Groussin, O., Gutirrez, P. J., Gutirrez-Marquez, P., Gttler, C., Ip, W.-H., Jorda, L., Knollenberg, J., Kovacs, G., Kramm, J.-R., Kppers, M., Lara, L. M., Lazzarin, M., Lopez Moreno, J. J., Marzari, F., Naletto, G., Penasa, L., Shi, X., Thomas, N., Toth, I., and Tubiana, C. (2017). Constraints on cometary surface evolution derived from a statistical analysis of 67Ps topography. *Monthly Notices of the Royal Astronomical Society*, 469(Suppl˙2):S329–S338.

Vincent, J.-B., Oklay, N., Pajola, M., Höfner, S., Sierks, H., Hu, X., Barbieri, C., Lamy, P., Rodrigo, R., Koschny, D., et al. (2015b). Are fractured cliffs the source of cometary dust jets? insights from osiris/rosetta at 67p. *arXiv preprint arXiv:1512.03193*.

Visser, R., Jørgensen, J. K., Kristensen, L. E., Van Dishoeck, E. F., and Bergin, E. A. (2013). Hot water in the inner 100 au of the class 0 protostar ngc 1333 iras2a. *The Astrophysical Journal*, 769(1):19.

Vokrouhlický, D., Nesvorný, D., and Dones, L. (2019). Origin and evolution of long-period comets. *The Astronomical Journal*, 157(5):181.

Von Mises, R. and Windenburg, D. (1933). The critical external pressure of cylindrical tubes under uniform radial and axial load. Technical report, DAVID TAYLOR MODEL BASIN WASHINGTON DC.

Wadell, H. (1933). Sphericity and Roundness of Rock Particles. *Journal of Geology*, 41:310–331.

Walsh, K. J., Morbidelli, A., Raymond, S. N., O'Brien, D. P., and Mandell, A. M. (2011). A low mass for mars from jupiters early gas-driven migration. *Nature*, 475(7355):206.

Whipple, F. L. (1950). A comet model. I. The acceleration of Comet Encke. *Astrophysical Journal*, 111:375–394.

Whipple, F. L. (1987). A review of cometary sciences. *Philosophical Transactions of the Royal Society of London Series A*, 323:339–347.

Yingst, R. A., Haldemann, A. F. C., Biedermann, K. L., and Monhead, A. M. (2007). Quantitative morphology of rocks at the mars pathfinder landing site. *Journal of Geophysical Research: Planets*, 112(E6):n/a–n/a. E06002.

Zheng, J. and Hryciw, R. (2015). Traditional soil particle sphericity, roundness and surface roughness by computational geometry. *Géotechnique*, 65(6):494–506.